QUANTITATIVE INVESTIGATION OF THE HOMOGENEOUS DECOMPOSITION OF TRIMETHYLINDIUM AND AMMONIA BY *IN SITU* RAMAN SPECTROSCOPY

By

JANG YEON HWANG

A DISSERTATION PRESENTED TO THE GRADUATE SCHOOL
OF THE UNIVERSITY OF FLORIDA IN PARTIAL FULFILLMENT
OF THE REQUIREMENTS FOR THE DEGREE OF
DOCTOR OF PHILOSOPHY

UNIVERSITY OF FLORIDA

2004

ACKNOWLEDGMENTS

The author would like to thank Drs. Chang-Won Park, Adrian E. Roitberg, and James D. Winefordner for being his committee members. He also wishes to present his sincere gratitude to his committee chair, Dr. Timothy J. Anderson. His encouragements were great support to the author throughout this work.

It was a great pleasure for the author to have a chance to learn with Dr. Zerner. His passion for teaching should be appreciated. The author also thanks Dr. Bartlett for encouraging him to take advantage of computational chemistry.

It was also a pleasure for the author to have chances to work with visiting scholars and colleagues in his research group.

The author wishes to express his appreciation to Mr. D. Vince and Mr. J. Hinnant for their kind support for his experiments. He also thinks that the staff members in the main office deserve his gratitude.

Finally, the author should express his sincere gratitude to his parents for their endless love and care for him.

TABLE OF CONTENTS

page

ACKNOWLEDGMENTS ii

LIST OF TABLES vi

LIST OF FIGURES vii

ABSTRACT xi

CHAPTER

1 INTRODUCTION 1

2 REACTOR AND MODELING 8

- 2.1 Background 8
- 2.2 Reactor System 10
  - 2.2.1 Reactor Assembly 11
  - 2.2.2 Gas Handling Circuit 12
- 2.3 Reactor Model 14
  - 2.3.1 Model Description 14
  - 2.3.2 Numerical Model 16
  - 2.3.3 Derivation of Mass Diffusion Flux Equation 21
  - 2.3.4 Property Estimation for Simulations 24
- 2.4 Penalty Finite Element Method 26
  - 2.4.1 The Galerkin Method 26
  - 2.4.2 Penalty Formulation 29
  - 2.4.3 A Simple Test 31
- 2.5 Summary 32

3 RAMAN SCATTERING AND COMPUTATIONAL CHEMISTRY 34

- 3.1 Introduction 34
- 3.2 Theoretical Background of Raman Scattering 38
  - 3.2.1 Selection Rules for Raman Scattering 39
  - 3.2.2 Intensity of Raman Scattering 42
- 3.3 Applications of Raman Scattering 45
  - 3.3.1 Raman System 45
  - 3.3.2 Temperature Determination 48

3.3.2.1 Formulation 48
3.3.2.2 Applications 49
3.3.3 Concentration Determination 52
3.3.3.1 Formulation 52
3.3.3.2 Applications 53
3.4 Computational Chemistry 56
3.4.1 Vibration Frequency 58
3.4.1.1 Harmonic vibration 58
3.4.1.2 Hot band transition 59
3.4.2 Basis Set Superposition Error 62
3.4.3 Calculation of Thermodynamic Properties 64

4 MODEL VALIDATION FOR HEAT AND MASS TRANSPORT 66

4.1 Heat Transport 66
4.1.1 Background 66
4.1.2 Validation of the Heat Transport Model 67
4.1.3 Gas Phase Dynamics 69
4.1.4 Summary 79
4.2 Mass Transport 79
4.2.1 Background 79
4.2.2 First Inlet Configuration 81
4.2.3 New Inlet Configuration and Flow Instability 86
4.2.4 Mass Transport Characteristics in the Reactor 97
4.2.5 Conclusions 102

5 PARAMETER ESTIMATION PROCEDURE 103

5.1 Background 103
5.2 Establishment of Parameter Estimation Procedure 104
5.2.1 Fundamental Formulation 104
5.2.2 Optimization Scheme 107
5.2.2.1 Deterministic methods 107
5.2.2.2 Simple genetic algorithm 110
5.2.3 Implementation of a Simple Genetic Algorithm 112
5.2.3.1 Parameters encoding 112
5.2.3.2 Selection 114
5.2.3.3 Reproduction 114
5.2.3.4 Performance tests 115
5.2.3.5 Crowding model – an advanced concept 120
5.2.4 Summary 121
5.3 Application to Mass Transport 122
5.3.1 Introduction 122
5.3.2 Experimental 123
5.3.3 Problem Formulation 125
5.3.4 Optimization Scheme 127
5.3.5 Applications and Discussion 128

5.3.6 Conclusions 135

6 BEHAVIOR OF AMMONIA AND TRIMETHYLALUMINUM 137

6.1 Ammonia Decomposition 137
6.1.1 Introduction 137
6.1.2 Experimental 138
6.1.3 Results and Discussion 140
6.1.4 Conclusions 149
6.2 Behavior of Trimethylaluminum 150
6.2.1 Background 150
6.2.2 Experimental 150
6.2.3 Results 151
6.2.4 Summary 155

7 DECOMPOSITION OF TRIMETHYLINDIUM 157

7.1 Introduction 157
7.2 Kinetics of TMIn Decomposition 161
7.2.1 Experimental 161
7.2.2 Numerical Description 163
7.2.3 Results and Discussion 164
7.2.4 Conclusions 175
7.3 Reaction Intermediates 176
7.3.1 Experimental 176
7.3.2 Computational Chemistry 178
7.3.3 Experimental Results 180
7.3.4 Reaction Intermediates 183
7.3.5 Conclusions 191
7.4 Interaction between TMIn and Ammonia 191
7.4.1 Experimental 191
7.4.2 Results and Discussion 192
7.4.3 Conclusions 196

8 CONCLUSIONS AND RECOMMENDATIONS 197

LIST OF REFERENCES 202

BIOGRAPHICAL SKETCH 215

LIST OF TABLES

Table page

2-1. Calibration results for mass flow controllers 14

3-1. Electronic transitions of Group III atoms. 36

3-2. Calculated spectral resolutions (cm^{-1}). 47

3-3. Apparent relative Raman cross-sections for three gas mixtures 54

3-4. Experimental and calculated vibrational frequencies (cm^{-1}). 58

3-5. Vibrational transitions of MMIn 62

3-6. Ga-C bond energies in TMGa decomposition (kcal/mol). 65

5-1. Parameter estimation results from methane dispersion experiments 132

5-2. Parameter estimation results from ammonia dispersion experiments. 132

6-1. Values of apparent relative Raman cross-section of ammonia and activation energy for concentration and reaction rate calculations, respectively 143

7-1. Normalized relative Raman intensities of TMIn, MMIn, and atomic indium 165

7-2. Present and reported reaction rate constants for TMIn decomposition 173

7-3. Calculated ΔH and ΔG depending on model chemistry (kcal/mol) 178

7-4. Average ΔH and ΔG for Reactions 7-6a through 6c for the temperature range 200 to 600 °C (in kcal/mol) 184

7-5. ΔH and ΔG for the selected reactions using B3LYP/(6-311++G(2d,2p) + SDB-aug-cc-pVTZ) 186

7-6. ΔH, ΔG, and reaction rate constants for Reactions 7-6d and 7-6e. 188

7-7. Calculated vibrations for selected intermediates. 188

7-8. Estimated ν_s(In-C) of the adduct. 194

LIST OF FIGURES

Figure page

1-1. Methodology developed in this study 5

2-1. A picture of the reactor used in this work. 10

2-2. Schematic of the first reactor configuration 11

2-3. Gas handling circuit. 13

2-4. Schematic of the axisymmetric reactor model. 15

2-5. Two fundamental configurations in the view factor calculations 19

2-6. Velocity profiles at $x = 0.5$ (V) and $y = 0.5$ (U) for $Re = 400$ 32

3-1. Observed decomposition behavior of phospine depending on probing methods 35

3-2. Schematic of the Raman system. 45

3-3. Temperature determination 50

3-4. Overlap of spectra in the nitrogen rotation band 51

3-5. A gas flow cell used in the Raman cross-section study. 54

3-6. Hypothetical spectral transmittance of quartz 55

3-7. Curve fitting the calculated potential (—) with the Morse potential (---). 61

3-8. Size of the available basis set in (a) is different from that in (b). 63

3-9. Adduct formation from TMGa and ammonia 64

4-1. Axial temperature profiles for two inlet velocities 68

4-2. Temperature profiles along the centerline of the reactor 70

4-3. Calculated streamlines and isotherms in the reactor for N_2 carrier gas 73

4-4. Calculated streamlines and isotherms in the reactor for H_2 carrier gas 75

4-5. Calculated (a) streamlines and (b) isotherms in the reactor with H_2 carrier gas 78

4-6. The first inlet configuration used in the model validation..82

4-7. Axial concentration profiles along the centerline of the reactor 83

4-8. Axial concentration profiles along the centerline of the reactor for the gas velocities of (●) 1.5 cm/s and (■) 2.5 cm/s 84

4-9. Concentration profile with partially removed glass beads 86

4-10. Modified inlet configuration...87

4-11. Axial concentration profiles of CH_4 with the modified inlet configuration.............89

4-12. Axial concentration profiles of CH_4 at r = 0 mm (O, ---) and r = 10 mm (●, —)...90

4-13. Streamlines and concentration contours in the reactor when 10 % CH_4/N_2 is introduced through the annulus inlet...92

4-14. Axial concentration profiles of CH_4 for three different inlet concentrations 93

4-15. Streamlines and concentration contours in the reactor when 5 % CH_4/N_2 is introduced through the annulus inlet...94

4-16. Axial concentration profiles of CH_4 with a reduced gas-travel length at 23 °C.......95

4-17. Effects of filling the annulus channel on streamlines and concentration contours ..96

4-18. Methane concentration profiles at 24 °C along the centerline.................................98

4-19. Radial CH_4 concentration profiles at different axial positions 99

4-20. Calculated radial concentration profiles of TMIn 100

4-21. Calculated centerline concentration profiles of NH_3..101

5-1. The shape of the objective function in Problem 1..116

5-2. Performance of the genetic algorithm for Problem 1 117

5-3. The shape of the objective function in Problem 2 118

5-4. Test results for the second problem...119

5-5. Schematic of the reactor used in parameter estimation. 124

5-6. Measured and simulated axial concentration profiles for the gas velocity of 2.5 (●), 3.5 (■), and 4.5 (▲) cm/s 129

5-7. Measured and simulated axial concentration profiles for inlet concentration 4 (●) and 8 (■) mole % ammonia in N_2..129

5-8. Performance of the parameter estimation procedure..130

5-9. Shape of the objective function near the estimates for the ammonia case 134

6-1. Schematic of the reactor for ammonia study...139

6-2. Ammonia concentration (●) and gas temperature (O) profiles along the centerline of the reactor at different heater temperatures.......................................141

6-3. Transmission characteristic of the reactor walls for two temperatures 146

6-4. The square-root term in Eq. 6-9 evaluated by using a W-lamp................................146

6-5. Simulated temperature distributions at the reactor wall for different heater temperature..147

6-6. Ammonia concentration (●) and gas temperature (O) profiles along the centerline of the reactor with the heater temperature set at 500 °C........................149

6-7. Observed Raman peaks for $(TMAl)_2$ at 21 °C..152

6-8. Measured and simulated $(TMAl)_2$ concentration profiles at 21 °C 152

6-9. Axial velocity component and $(TMAl)_2$ mole fraction 154

6-10. Dissociation behavior of $(TMAl)_2$ into TMAl at various temperature position.....155

7-1. Schematic of the reactor. 161

7-2. Experimental (■) and simulated (—) gas temperature profiles 165

7-3. Exhaustive scan with the parameters defined in Eq. 7-3..167

7-4. Performance of genetic/Simplex approach..168

7-5. Exhausted scan with a fixed relative Raman cross-section ($\Sigma_{TMIn} = 22.3$)...............169

7-6. Experimental (■) and simulated concentration profiles of TMIn............................170

7-7. Reported reaction rates for TMIn decomposition with different carrier gases.........172

7-8. Experimental (◆) and calculated MMIn concentration profiles..............................174

7-9. Schematic of the reactor for the reaction intermediate study. 177

7-10. Observed spectra in the ranges of In-C vibrations and the atomic indium transition........181

7-11. Spectra taken in the nitrogen rotation band........182

7-12. Reaction intermediates during TMIn decomposition........185

7-13. IRC calculation for a transition state of $(DMIn)_2$ in Reaction 7-6e........187

7-14. Raman spectra in the range of $HInCH_3$ vibrations........189

7-15. Changes in TMIn characteristic peaks for the following conditions........192

7-16. TMIn decomposition in the presence of NH_3........195

Abstract of Dissertation Presented to the Graduate School
of the University of Florida in Partial Fulfillment of the
Requirements for the Degree of Doctor of Philosophy

QUANTITATIVE INVESTIGATION OF THE HOMOGENEOUS DECOMPOSITION OF TRIMETHYLINDIUM AND AMMONIA BY *IN SITU* RAMAN SPECTROSCOPY

By

Jang Yeon Hwang

August 2004

Chair: Timothy James Anderson
Major Department: Chemical Engineering

A new methodology was established to better understand the physical/chemical behavior of precursors used in metalorganic chemical vapor deposition (MOCVD). The methodology consists of *in situ* Raman scattering signals collection, detailed modeling of the process, and extracting unknown parameters from the experimental data using a combined genetic/Simplex algorithm and the validated reactor model.

The first order reaction rate constants for trimethylindium (TMIn) decomposition (k_0, E_a) and relative Raman cross-section were simultaneously estimated from observed Raman scattering intensities: $10^{17.9}$ s^{-1}, 56.1 kcal/mol, and 22.3, respectively. The reactor model revealed that TMIn decomposition occurred and completed in the gas phase between 120 and 535 ^{o}C, while monomethylindium (MMIn) was found to decompose on the susceptor surface as well as in the gas phase. In addition, a new reaction intermediate ($HInCH_3$) was identified during TMIn decomposition. Its characteristic vibrations were observed at 416 [ν(H-In-C)], 464 [ν(In-C)], and 1560 cm^{-1} [ν(In-H)]. The kinetic

constants for its decomposition into indium and methane were estimated using quantum chemistry calculations: $k_0 = 1.4 \times 10^{14}\ s^{-1}$ and $E_a = 30.8$ kcal/mol.

Ammonia was found to decompose on a quartz surface and the values of activation energy with a simple kinetic reaction model were 10.9, 12.6, 14.5, and 15.8 kcal/mol at a heater temperature of 300, 500, 700, and 900 °C, respectively. During this investigation, it was also found that transmittance of quartz is a function of temperature and wavelength of the light and influences the interpretation of the signal. The adduct of TMIn and NH_3 was identified by observing 5 cm^{-1} shift of the symmetric In-C vibration. It was considered that decomposition intermediates of TMIn reacted with NH_3 near the heated susceptor and the reaction product seemed stable.

It was also observed that a large density variation caused by molecular weight difference in the reactor could change flow regimes. The onset of instability was characterized by solutal density difference, gas velocity, and distance traveled by the gas. Investigation on $(TMAl)_2$ behavior in the reactor suggested that the natural convection due to solutal density difference can be mitigated by applying heat in the current inverted geometry of the reactor. In addition, it was observed that the dimer almost completely dissociated at 135 °C in the reactor.

CHAPTER 1
INTRODUCTION

Since the transistor was invented by J. Bardeen, W. Brattain, and W. Shockley, silicon has been widely used for semiconductor devices. There has been the necessity, however, for new semiconductor materials for reliable high temperature and high power operations and for short wavelength optical and optoelectronic applications. Silicon has a fixed low and indirect bandgap (1.1 eV) and therefore is not suitable for the applications mentioned above. These new applications require wide bandgap and thermally stable materials [Mor94]. Controllable bandgap materials are especially necessary for optoelectronic applications. The compound semiconductors formed from the groups IIIB (Al, Ga, In) and VB (N, P, As) or from the IIB (Zn, Cd, Hg) and VIB (S, Se, Te) elements are particularly suited. By forming solid solutions, a continuous range of bandgap energies can be obtained.

One of the most important application areas of compound semiconductors is for optoelectronic devices including blue and green LEDs and ultraviolet light detectors [Amb98]. ZnSe (II-VI) was introduced for semiconductor laser applications prior to recent advances in group III-nitride (III-V) semiconductors. ZnSe, however, has proven to be inferior to nitrides in their long term stability [Mor94]. Therefore, nitride compounds have been studied more actively. The bandgaps of InN, GaN, and AlN are 1.9, 3.4 and 6.2 eV, respectively. It has been recently suggested that bandgap of InN be less than 1 eV [Bec02]. These bandgaps cover the full visible and ultraviolet (UV) ranges and therefore, by manipulating the bandgap through composition control, a full complement of devices can be fabricated. In addition to their wide bandgap, group III-nitrides are known to have high mechanical strength, good thermal conductivity, and chemical stability [Amb98, Mor94]. Therefore, group III-nitrides are promising materials for light emitters or detectors and high temperature and/or high power devices [Amb98, Mor97].

Compound semiconductor materials involving group III-nitrides are grown by a number of processes including metalorganic chemical vapor deposition (MOCVD) and molecular beam epitaxy (MBE). MOCVD is the most common technology to grow thin films with good crystal quality and electrical properties after the introduction of heteroepitaxy [Kol98]. To optimize MOCVD reactor design and operating conditions, an understanding of the reaction kinetics is necessary. The MOCVD reaction kinetics and mechanisms are not well understood even though excellent results have been achieved in practice. For example, the homogeneous decomposition of trimethylindium (TMIn) was first investigated by Jacko and Price [Jac64] using toluene as a carrier gas at low pressure. Subsequent studies used flow tube reactors and physical sampling of the reacting gas mixture to investigate the effect of the carrier gas on the extent of decomposition [Buc88, But86, Jac64, Lar86]. The reaction rate constants for the apparent first order decomposition reaction suggested by analysis of these measurements, however, were variable with the reported activation energy for removal of the first methyl group ranging from 35.9 to 54.0 kcal/mol and frequency factors range from $10^{12.0}$ to $10^{17.9}$ s^{-1}. For trimethylgallium (TMGa), the reported apparent activation energy for dissociation of the first methyl group ranges from 58 to 62 kcal/mol [Che91, Hos90, Jac63]. In addition, for trimethylaluminum (TMAl), the two reported values of activation energy for the removal of the first methyl group are very different (9 [Suz86] and 38 kcal/mol [Suz85]). These variations possibly reflect experimental uncertainties as well as chemical effects from the choice of carrier gas.

Most of the currently available decomposition kinetic data were typically obtained from simple flow cell or flow tube experiments coupled with mass or infrared (IR) spectroscopy. There are two characteristics to be noted about these types of experiments. First, homogeneous conditions are assumed in the cell to simplify the data analysis, even though the conditions at the reactor wall or sampling system introduce opportunities for heterogeneous reactions. Wide ranges of observed activation energies for decomposition of TMIn and TMAl are not fully explained by chemical effects from the choice of carrier gas [Kop84, Tho96, Yas85], but reveal experimental uncertainties. It is known that thermal decomposition of metalorganic precursors is influenced by catalytic effects of the reactor or substrate surface [Nis97, Sug97]. In addition, it was suggested [Mcd00] that surfaces play an important role in decompostion of metalorganic precursors in a flow tube reactor and flow tube reactors are not suitable for decomposition study of metalorganic precursors. Therefore, gas and surface reactions are usually confounded in experimental results and neglect of either without careful consideration can give rise to an incorrect analysis or inconsistent conclusions. Second, a small amount of reacting material is sampled for detection, i.e., *ex situ* observation. Reactive species can change their chemical form while flowing through a sampling tube and conditions in the detection unit are usually very different from those in the reactor. As a result, *ex situ* observation can be different from what actually occurs in the reactor. Based on the above discussion, it is considered that more reliable kinetic information on a MOCVD process is obtainable if *in situ* probing is used and both kinds of reactions are effectively discriminated with a better understanding of the process.

Non-intrusive detection of species and temperature has been widely studied in the combustion area for air-pollutant control purposes [Kel97]. Optical probing is a non-intrusive method and applicable to the investigation of MOCVD processes. Richter *et al.* [Ric91] have compared several optical diagnostic methods that can be used to obtain a better understanding of MOCVD processes. Although optical probing is non-intrusive, the information is limited by experimental factors; e.g., geometric limits and complex situations in MOCVD reactors make it difficult to analyze the experimental data. To elicit quantitative, meaningful results from the limited experimental data, modeling the reactor is necessary because the flow and thermal fields in MOCVD reactors can be complex. In addition, the validated reactor model can provide detailed information about gas dynamics, which is important in MOCVD processes because it is known that the reactor is often operated in the mass transport limited region [Has84, Li98]. Modeling work has been conducted to obtain a better insight of MOCVD processes with limited information [Dil91, Mou91, Pes98], while measured overall growth rates were used to validate the model [Saf97]. Temperature and species concentration profiles obtained without disturbing the reactions and flow patterns in the reactor, however, can be used to validate the reactor model and then the validated model could be used to extract detailed information about the process from limited observed information.

To obtain a better understanding of MOCVD of Group III-nitrides, a reliable methodology to extract kinetic information for these chemical systems has been established in this work. The methodology mainly consists of developing a measurement reactor system, modeling the reactor, and extracting physical parameters from experimental data (see Figure 1-1).

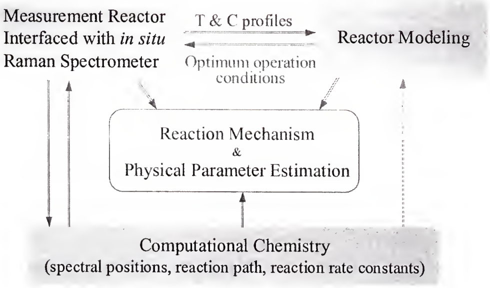
Measurement Reactor
Interfaced with *in situ*
Raman Spectrometer
T & C profiles
Optimum operation conditions
Reactor Modeling
Reaction Mechanism
&
Physical Parameter Estimation
Computational Chemistry
(spectral positions, reaction path, reaction rate constants)

Figure 1-1. Methodology developed in this study.

A measurement reactor was interfaced with a Raman spectrometer to simultaneously obtain temperature and species information in the reactor with good spatial resolution. To simplify modeling of the reactor, the measurement reactor was designed to have axisymmetry. To interpret *in situ* observations, i.e., composition and temperature profiles in the reactor, a 2-D aximsymmetric reactor model was established, including momentum, heat, and mass transport. A finite element method (FEM) was used to numerically deal with a set of partial differential equations and complex reactor geometry in the reactor model. The reactor model should be validated before used to analyze experimental data or customize experimental conditions for a specific objective of the experiment. Observed temperature and concentration profiles can be used for this purpose. In the validation process, it is also important to have a well-designed reactor in that its boundary conditions can be reasonably described by simple mathematical expressions in the reactor model. A measurement reactor and its validated model can be used to interpret subsequent experimental data and understand reaction mechanism. Furthermore, by combining the reactor model and a reliable optimization algorithm, a parameter estimation procedure can be established to extract unknown physical parameters from experimental observations. Through the aforementioned methodology, quantum chemistry calculations can provide complementary information. Calculated spectral positions of a new reaction intermediate are useful in performing experiments and interpreting the experimental results. On the other hand, experimental observation can be used to scale calculated expectation. It can be also used to calculate physical properties of new intermediates required in the model and to estimate reaction rate constants using transition state theory.

This work is made up of eight chapters including this chapter. In Chapter 2 Reactor and Modeling, the measurement reactor configuration is explained along with the gas handling system for the reactor. In the modeling part, physical and numerical models are described. In Chapter 3 Raman Scattering and Computational Chemistry, the theoretical background for Raman spectroscopy is briefly reviewed and then temperature and species characterization is discussed. Some practical issues in temperature and concentration determination are also considered. The Raman system used in this work is described in this chapter. In addition, applications of computational chemistry in spectroscopy and properties estimation are exemplified. In Chapter 4 Model Validation for Heat and Mass Transport, the reactor model developed in Chapter 2 is validated with experimental data, and heat and mass transport characteristics in the reactor are discussed. In addition, flow instability caused by solutal density difference is discussed. In Chapter 5 Parameter Estimation Procedure, a parameter estimation procedure is established using the reactor model and genetic/Simplex algorithms and performance of the procedure is tested with actual experimental data. In Chapter 6 Behavior of Ammonia and Trimethylaluminum, reactions of ammonia in non-isothermal conditions and behavior of TMAl in the measurement reactor are discussed. In Chapter 7 Decomposition of Trimethylindium, homogeneous decomposition of TMIn and its reaction intermediates are discussed and the parameter estimation procedure is applied to simultaneously estimate reaction rate constants (k_0 and E_a) and the relative Raman cross-section of TMIn. In addition, interaction between TMIn and ammonia is briefly discussed. In Chapter 8 Conclusions and Recommendations, this work is concluded and some recommendations are considered.

CHAPTER 2
REACTOR AND MODELING

2.1 Background

Cold-wall chemical vapor deposition (CVD) reactors are frequently used to deposit thin solid films. In particular, MOCVD is widely used for depositing epitaxial films of compound semiconductors [Hir82, Str89]. It is beneficial to establish a uniform flow field in the reactor that is free of vortices to minimize gas switching time and unwanted contamination. The flow field in the reactor also plays a major role in developing gas phase isotherms parallel to the substrate. The flow pattern in a CVD reactor is influenced by several factors including the reactor geometry, heat transfer characteristics, and the flow boundary conditions. The influence of buoyancy forces due to thermal effects in CVD reactors has been extensively studied [Hol92, Jen89, Mon88]. A large thermal gradient not aligned with the direction of the gravity vector can produce recirculating flow patterns in the reactor and cause adverse effects on the film quality [Gil82, Hol92, Jen91, Par02, Pat89]. It was also reported that the buoyancy caused by temperature gradients could break the condition of axisymmetry to trigger flow instability [Hol92, San00]. Recirculation or unstable flow patterns should be eliminated or at least minimized for satisfactory process control and reproducibility. With respect to recirculation flow, an inverted reactor geometry in which cold gas flows up toward the heated substrate has certain advantages because the buoyancy tends to stabilize the flow. In addition, particulate impingement effects should be reduced because of the favorable alignment of the reactor with respect to gravity. This reactor geometry is also suited for experiments to extract kinetic data, given the relatively well-defined flow and temperature fields in the reactor. Wafer mounting onto the inverted susceptor, of course, would be more difficult than in the non-inverted designs.

Most of the previously reported kinetics data of reactions of sources for MOCVD were obtained with simple flow cell experiments, but reaction experiments with *in situ* probing techniques under real flow conditions possibly render more detailed information about the reaction kinetics and mechanism. Analyses of the experimental data are, however, more complicated than in simple flow cell cases where homogeneous conditions have been assumed inside the flow cell to simplify analysis of experimental data. In actual non-isothermal flow reactors, flow, temperature, and concentration distributions are not uniform and therefore modeling work is required to take full advantage of the *in situ* observation and to obtain a better understanding of the phenomena.

Modeling work has been performed to obtain better insight of MOCVD processes with the limited information [Mou91, Oh91, Pes98]. Safvi *et al.* [Saf97] compared experimental measurements of GaN growth rates with modeling results. Chinoy *et al.* [Chi91] investigated the factors controlling the flow and temperature fields in a vertical upflow MOCVD reactor (e.g., susceptor temperature, susceptor-nozzle distance, gas flow rate, and reactor pressure), and radiation heat transfer rates were found to be as significant as those by convection. In most of the modeling studies of MOCVD processes, the momentum, energy, and overall mass balances are assumed independent of precursor concentrations because the concentrations are generally very low compared to the carrier gas concentration. In nitride cases, however, the concentration of nitrogen source is not as low as in other typical MOCVD cases. Therefore, species balances for carrier gas (nitrogen or hydrogen) and nitrogen source (ammonia) are solved simultaneously along with momentum and energy balances. Metalorganic sources are usually heavier than carrier gas and this difference can cause natural convection, and therefore the mass and momentum transfer in the MOCVD reactor should be considered at the same time.

In this chapter, the reactor used in this work is described along with a gas handling circuit to supply gases to the reactor. Then, modeling the reactor is discussed and the developed numerical simulation code is tested with the driven cavity flow.

2.2 Reactor System

The reactor system used in this work consisted of reactor assembly and a gas handling circuit. A photograph of the up-flow, cold-wall CVD reactor used in this work is shown in Figure 2-1.

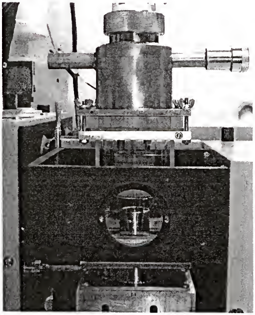

Figure 2-1. A picture of the reactor used in this work.

2.2.1 Reactor Assembly

The first reactor configuration is schematically depicted in Figure 2-2 to show its cross-section.

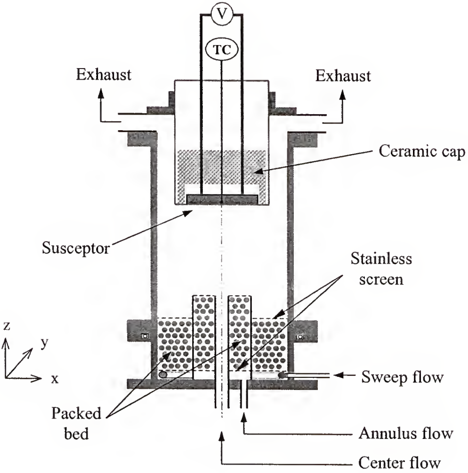

Figure 2-2. Schematic of the first reactor configuration. The electric power supply and a thermocouple are denoted by V and TC, respectively.

The reactor assembly was put on a stage that was able to move in two directions (xz). Thereby, it was possible to select a detection point in the reactor with respect to a spatially fixed laser line. Each part of the reactor is explained in the following.

Main body. The main body (middle part of the reactor) was made of quartz to probe the inside of the reactor with Raman spectroscopy, because quartz is transparent to the visible range of light [Ing88]. To make it easy to model the reactor afterwards, the reactor was built to have axisymmetry. In the real reactor, however, the main body was a quartz square duct to minimize loss of optical signals and a quartz cylinder (ID = 70 mm) with four longitudinal slots at possible optical paths was put inside the square duct. These quartz parts were seated on top of a stainless base described in the next.

Base. The base was equipped with three gas inlets, labeled center, annulus, and sweep inlets, respectively, in Figure 2-2. The center and annulus inlet channels were used for chemicals, while an inert gas was supplied through the sweep inlet channel to help maintain flow stability [Hwa04] and to protect quartz walls from any kind of deposit. Because gases were supplied by small diameter tubes, stainless screens and glass bead layers were used to produce a better gas distribution. Especially for the sweep inlet, the supply tube was connected to a ring-shaped distributor beneath the stainless screen.

Top. A stainless part was put on top of the quartz parts, i.e. the main body explained above, which held gas exhaust lines and a quartz envelope (OD = 50 mm). An electric heating unit was seated on top of a quartz block inside the quartz envelope and a thermocouple was put under the heating unit to measure the temperature of the heater. A porous ceramic cap was placed over the heating unit to reduce heat loss from the heater and radiation noises to observed Raman spectra. The bottom surface of the quartz envelope served as the susceptor in this work. The distance between the susceptor and inlets was adjusted by moving the quartz envelope. Gases were introduced through three concentric inlets at the bottom of the reactor, impinge upon the susceptor, and exit through the annulus area at the top of the reactor.

2.2.2 Gas Handling Circuit

A gas handling system was used to supply gases to the reactor (Figure 2-3). The system could supply two different gases to the reactor at the same time and two metalorganic bubblers could be connected. The operation of metalorganic bubblers was characterized elsewhere [Her90].

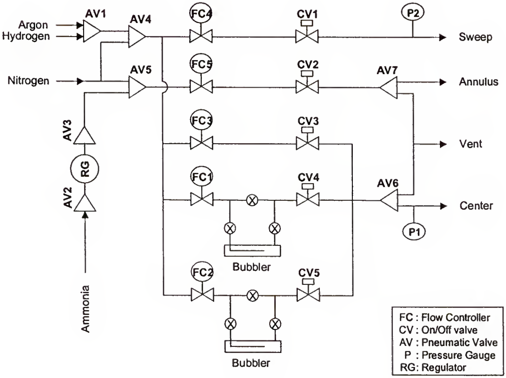

Figure 2-3. Gas handling circuit.

Gas flow rates were controlled by five mass flow controllers (UNIT Instruments). The mass flow controllers were calibrated with bubble flow meters flowing nitrogen for the control range from 20 to 80 % and the calibration results were summarized in Table 2-1. The mass flow controllers showed good linearity for the calibration range as shown by R^2 values. When these mass flow controllers were used to control gases other than nitrogen, flow rates were corrected by dividing them by a proper correction factor.

With a nitrogen standard, they are 1.01, 0.74, and 0.72 for hydrogen, ammonia, and methane, respectively.

Table 2-1. Calibration results for mass flow controllers. Flow rate was calculated by the formula: $y = A + Bx$, where y is % control and x is a desired flow rate (sccm).

Controller	Control caliber	A	B	R^2
FC 1	100 sccm	0.223	0.8917	1.00
FC 2	100 sccm	-0.250	0.8972	1.00
FC 3	2.5 slm	-0.13	0.03822	1.00
FC 4	10 slm	-6.2	0.01187	0.997
FC 5	2.5 slm	-0.616	0.03630	1.00

2.3 Reactor Model

2.3.1 Model Description

A two-dimensional axisymmetric model presented in Figure 2-4 was conceived to describe transport phenomena occurring in the reactor. It was assumed that gases were introduced from the porous layer at the bottom of the reactor at initial velocities of V_C, V_A, and V_S at the center, annulus, and sweep inlets, respectively. The gases were assumed to exit the reactor with a fully developed flow profile through the annulus region at the top of the reactor. This is reasonable assumption because, in most experiments, the length of the annulus region was more than seven times longer than the gap in the annulus. No slip conditions were used on all the other solid surfaces. Natural boundary conditions were assumed along the centerline of the reactor for all transport processes.

To include detailed descriptions of heat transfer in the reactor, the solid part of the reactor was included in the reactor model as well as the gas region. When the heater was activated, it was assumed that a constant temperature (T_{Heater}) was maintained at the top of an imaginary block inside the quartz envelope. Contact resistance between the heating unit and the envelope surface was modeled by adjusting thermal conductivity of the block.

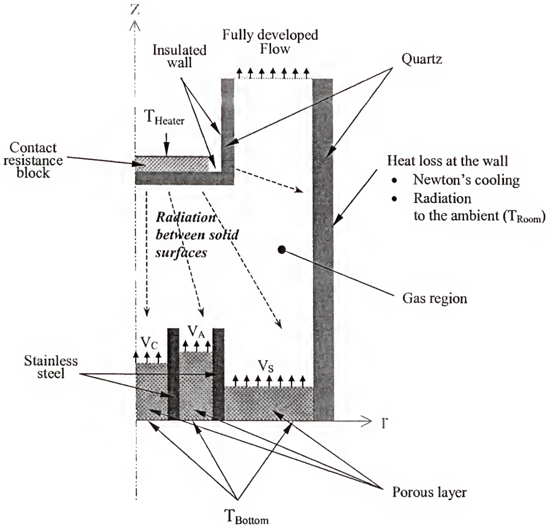

Figure 2-4. Schematic of the axisymmetric reactor model.

Conductive heat was only considered inside the quartz envelope, i.e. insulated wall, and it was assumed that the porous ceramic cap over the heating unit could effectively reduce the radiation heat loss (see Figure 2-2). Incorporation of the imaginary block gives tolerance to this assumption. A constant temperature (T_{Bottom}) was given at the bottom surface of the reactor, which would be experimentally measured for every non-isothermal experiment. It is known that radiation heat transfer is important to reasonably describe MOCVD processes [Fot90a, Fot90b] and therefore radiation heat transfer was considered between solid surfaces inside the reactor. At the outside walls, it was assumed that heat was being lost by both Newton's cooling and radiation to the ambient at room temperature.

In mass dispersion or reaction cases, a gas mixture with a fixed concentration was assumed to flow into the reactor through selected inlets. Because the reactor had only one heat source in the quartz envelope and a sweeping flow was used to keep the sidewalls clean, surface reactions were allowed only on the susceptor surface, while other surfaces were assumed to be impenetrable.

2.3.2 Numerical Model

In MOCVD reactors, the temperature gradient near the susceptor is very large, e.g. 100 ^{o}C/mm, and there must be large variations in the gas density. To describe this change, the ideal gas law was adopted in this work. This is an appropriate assumption because of high temperature and atmospheric or below pressure conditions in typical MOCVD reactors. The pressure dependence of the density was not considered and a nominal pressure was used for the density calculation because gas velocities in usual MOCVD reactors were much smaller than the speed of sound. Thermal diffusion was also included in the species balance as the temperature gradient is usually high in nitride MOCVD reactors and nitrogen or hydrogen is used as the carrier gas in a MOCVD process, molecular weight of which is very low compared with those of metal organic sources. Another consequence of the high temperature condition is substantial effects of radiation on the process.

At steady state, transport phenomena in the reactor were described by the following governing equations [Bir90]:

- Equation of state (ideal gas law):

$$\rho = \frac{PM}{RT} \tag{2-1}$$

- Continuity:

$$\nabla \cdot \rho \vec{v} = 0 \tag{2-2}$$

- Momentum balance:

$$\rho \vec{v} \cdot \nabla \vec{v} = -\nabla p + \nabla \cdot \mu \left(\nabla \vec{v} + (\nabla \vec{v})^T \right) + \rho \vec{g} \tag{2-3}$$

- Energy balance:

$$\rho C_p \vec{v} \cdot \nabla T = \nabla \cdot k \nabla T \tag{2-4}$$

- Balance for species k:

$$\rho \vec{v} \cdot \nabla w_k = \nabla \cdot \left\{ \sum_{i=1}^{\lambda-1} L_{ki} \nabla w_i + G_k \nabla \ln T \right\} + r_k , \quad k = 1, \dots \lambda - 1 \tag{2-5}$$

where ρ, μ, C_p, and M are the density, viscosity, heat capacity, and molecular weight of the gas mixture, respectively. P, R, k, T, and $\vec{g}$ are the nominal pressure, gas constant, thermal conductivity, temperature, and gravity, respectively. $\vec{v}$ and p are the velocity vector and pressure within the gas region. In Eq. 2-5, w_k and r_k are the mass fraction and production rate of species k, respectively. L_{ki} and G_k represent the multi component diffusion and thermal diffusion effects, respectively. The mass diffusion flux of component k, i.e. $\vec{j}_k$ was expressed in terms of them:

$$\vec{j}_k = -\sum_{i=1}^{\lambda-1} L_{ki} \nabla w_i - G_k \nabla \ln T \tag{2-6}$$

where

$$L_{ki} = \left(\frac{1}{M_i} - \frac{1}{M_\nu} \right) \sum_{m=1}^{\lambda-1} \left(B^{-1} \right)_{km} \frac{M^2}{M_m} w_m - \frac{M}{M_i} \left(B^{-1} \right)_{ki}, \tag{2-6a}$$

$$G_k = \sum_{i=1}^{\lambda-1} \left(B^{-1} \right)_{ki} \left\{ \sum_{m \neq i}^{\lambda} \tilde{C}_{im} \left(\frac{D_m^T}{\rho_m} - \frac{D_i^T}{\rho_i} \right) \right\}, \tag{2-6b}$$

and M_k is the molecular weight of component k and M is that of the mixture. Matrix component B_{ik} has the following expressions:

$$B_{ik} = \frac{\tilde{C}_{ik}}{\rho_k} - \frac{\tilde{C}_{i\lambda}}{\rho_\lambda} \tag{2-6c}$$

where $\tilde{C}_{ik} = x_i x_k / D_{ik}$ for a dilute ideal gas mixture where D_{ik} is the binary diffusion coefficient for components i and k. Detailed derivation of the mass diffusion flux used in this work and the practical expressions of the included terms for coding are explained in Section 2.3.3.

To complement the above governing equations, proper boundary conditions are necessary. For all transport processes, natural boundary conditions were applied along the centerline of the reactor. The other conditions are described in the following descriptions.

Momentum. At the walls of the reactor and the susceptor surface, the no-slip condition was applied. The gas flows into the reactor at the bottom and exits through the annulus area between the quartz envelope and the reactor wall.

Energy. Temperatures at the heater and bottom of the reactor were set to specified values. The ambient temperature was specified, because heat transfer between the outside wall of the reactor and the ambient was also considered (Newton's law of cooling). The heat transfer coefficient was estimated using the following equation [Inc85]:

$$\mathrm{Nu} = \left(0.825 + \frac{0.387\,\mathrm{Ra}^{1/6}}{\left[1 + (0.492/\mathrm{Pr})^{9/16}\right]^{8/27}}\right)^2 \qquad (2\text{-}7)$$

where Nu, Ra, and Pr are the Nusselt, Rayleigh, and Prandtl numbers, respectively. This correlation describes heat transfer on a vertical plate by natural convection. In modeling the current reactor, an adjustment factor around 1.0 was multiplied to the heat transfer coefficient to compensate modeling errors.

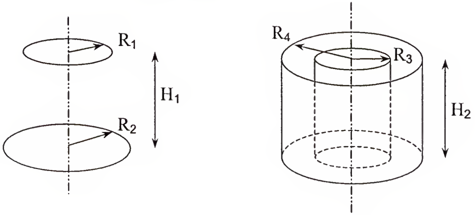

(a) (b)

Figure 2-5. Two fundamental configurations in the view factor calculations: (a) parallel disks and (b) concentric cylinders.

View factors between solid surfaces were calculated numerically using the view factor algebra [Sie72]. Two fundamental cases are shown in Figure 2-5 and the corresponding view factors for these configurations are [Sie72]:

$$F_{12} = \frac{1}{2}\left(X - \sqrt{X^2 - 4(R_2/R_1)^2}\right) \qquad (2\text{-}8a)$$

and

$$F_{34} = 1 - \frac{1}{\pi}\left\{\cos^{-1}\left(\frac{B}{A}\right) - \frac{1}{2L}\left[\sqrt{(A+2)^2 - 4R^2}\,\cos^{-1}\left(\frac{B}{RA}\right) + B\sin^{-1}\left(\frac{1}{R}\right) - \frac{\pi A}{2}\right]\right\}$$

(2-8b)

where

$X = 1 + (H_1^2 + R_2^2)/R_1^2$, $L = H_2/R_3$, $R = R_4/R_3$, $A = L^2 + R^2 - 1$, and $B = L^2 - R^2 + 1$.

Because the reactor had axisymmetry, all view factors between any two elementary surfaces inside the reactor could be calculated using the fundamental cases in Figure 2-5.

Mass. For impenetrable non-reacting surfaces, the boundary condition was simply

$$\vec{n} \cdot \left\{ \sum_{i=1}^{\lambda-1} L_{ki} \nabla w_i + G_k \nabla \ln T \right\} = 0 \tag{2-9}$$

where $\vec{n}$ is the vector normal to the surface and L_{jm} and G_j are defined in Eq. 2-6. On the susceptor surface, all the mass flux toward the surface should be equal to the net species consumption rate by surface reactions:

$$\vec{n} \cdot \left\{ \sum_{i=1}^{\lambda-1} L_{ki} \nabla w_i + G_k \nabla \ln T \right\} + M_k R_k^S = 0 \tag{2-10}$$

where R_k^S is the molar adsorption rate of species k at the substrate. R_k^S is usually estimated from kinetic theory as the following expression [Mou91, Pes98, Saf97]:

$$R_k^S = \frac{p}{\sqrt{2\pi M_k RT}} x_k \, s_k(\phi) \tag{2-11}$$

where x_k is the mole fraction of species k in the gas phase just above the substrate surface and s_k is the sticking coefficient for species k as a function of surface coverage ϕ. Because the adsorption is rapid at high temperature [Asp89] and deposition processes are limited by mass transfer [Has84, Li98], the sticking coefficient is usually set to one for simplicity [Mou93, Saf97].

2.3.3 Derivation of Mass Diffusion Flux Equation

In earlier CVD studies, the binary diffusion model was widely used because active components were dilute. Binary diffusion coefficients are independent of composition and furthermore this dilute situation simplifies analysis of the CVD process by decoupling mass transport from the other transport processes. In nitride cases, such a low concentration assumption is no longer valid. The concentration of metal sources is still low but that of ammonia is not. Therefore, the binary diffusion model is not applicable to nitride cases and all mass transport processes are coupled.

The mass diffusion flux of component k, $\vec{\mathbf{j}}_k$ was previously summarized as

$$\vec{\mathbf{j}}_k = -\sum_{i=1}^{\lambda-1} L_{ki} \nabla w_i - G_k \nabla \ln T \tag{2-6}$$

where L_{ki} and G_k represent the multi component diffusion and thermal diffusion effects, respectively. Eq. 2-6 was derived from the following Maxwell-Stefan form of the mass flux expression, which was suggested by Curtiss and Bird [Cur99], instead of the Fickian form, for multi component diffusion problems:

$$\sum_{k\neq i}^{\lambda} \tilde{C}_{ik} \left(\frac{\vec{\mathbf{j}}_k}{\rho_k} - \frac{\vec{\mathbf{j}}_i}{\rho_i} \right) = \frac{1}{cRT} \left(\nabla p_i - w_i \nabla p - \rho_i \vec{\mathbf{f}}_i + w_i \sum_{j=1}^{\lambda} \rho_j \vec{\mathbf{f}}_j \right) - \sum_{k\neq i}^{\lambda} \tilde{C}_{ik} \left(\frac{D_k^T}{\rho_k} - \frac{D_i^T}{\rho_i} \right) \nabla \ln T \tag{2-12}$$

where λ, c, R, T, and p are the number of components, total molar concentration, gas constant, temperature, and pressure of the system, respectively. In addition, D_k^T, ρ_k, w_k, $\vec{\mathbf{j}}_k$, $\vec{\mathbf{f}}_k$, and $\tilde{C}_{ik}$ are the thermal diffusion coefficient, density, mass fraction, diffusive mass flux, external force, and multi component inverse diffusivity of component k (see Eq. 2-6c), respectively. In this writing, bold face letters with an arrow are used for vector quantities. The thermal diffusion coefficient of component k, D_k^T was calculated according to Hirschfelder *et al.* [Hir54]. It is know that some of the physical quantities in the above equation have the following constraints [Cur99]:

$$\sum_{k=1}^{\lambda} \tilde{C}_{ik} = 0, \quad \sum_{k=1}^{\lambda} D_k^T = 0, \text{ and } \quad \sum_{k=1}^{\lambda} \vec{j}_k = 0. \tag{2-13}$$

The first relation is from the definition of multi component inverse diffusivity. The second and third are from the diffusion characteristic.

The two body force terms containing $\vec{f}_k$ cancel each other when gravity is the only external force [Cur99]. If the gas mixture is assumed ideal and dilute, the pressure gradient (∇p) is negligible and $\tilde{C}_{ik} = x_i x_k / D_{ik}$ where D_{ik} is the binary diffusion coefficient between components i and k [Cur49]. With these assumptions and the constraints in Eq. 2-13, the diffusive mass flux for component k, $\vec{j}_k$ was derived (Eq. 2-6). The binary diffusion coefficient is independent of the concentration and therefore the Maxwell-Stefan form is convenient for multi component problems, while the Fickian form contains the multi component diffusivity that is strongly dependent on the concentration.

The Maxwell-Stefan equation (Eq. 2-12) is written for component i, and an explicit form of it is necessary for the species balance equation. The left-hand side (LHS) of the equation is considered first.

$$\begin{aligned}(\text{LHS of Eq. 2-12}) &= \sum_{k \neq i}^{\lambda} \tilde{C}_{ik} \left(\frac{\vec{j}_k}{\rho_k} - \frac{\vec{j}_i}{\rho_i} \right) \\ &= \sum_{k \neq i}^{\lambda-1} \tilde{C}_{ik} \frac{\vec{j}_k}{\rho_k} + \tilde{C}_{i\lambda} \frac{\vec{j}_\lambda}{\rho_\lambda} + \tilde{C}_{ii} \frac{\vec{j}_i}{\rho_i}\end{aligned}$$

$$= \sum_{k=1}^{\lambda-1} \tilde{C}_{ik} \frac{\vec{j}_k}{\rho_k} - \sum_{k=1}^{\lambda-1} \tilde{C}_{i\lambda} \frac{\vec{j}_k}{\rho_\lambda} = \sum_{k=1}^{\lambda-1} \left(\frac{\tilde{C}_{ik}}{\rho_k} - \frac{\tilde{C}_{i\lambda}}{\rho_\lambda} \right) \vec{j}_k$$

In the third line, the first constraint in Eq. 2-13 was used. The term within the parentheses in the third line is an element of the matrix $\mathbf{B}$, i.e. B_{ik}. With the matrix inversion, the expression for mass flux $\vec{j}_k$ is obtained:

$$\vec{j}_k = \sum_{i=1}^{\lambda-1} \left(\mathbf{B}^{-1}\right)_{ki} \left[\nabla x_i - \left\{ \sum_{m \neq i}^{\lambda} \tilde{C}_{im} \left(\frac{D_m^T}{\rho_m} - \frac{D_i^T}{\rho_i} \right) \right\} \nabla \ln T \right], \quad B_{ik} = \frac{\tilde{C}_{ik}}{\rho_k} - \frac{\tilde{C}_{i\lambda}}{\rho_\lambda} \qquad (2\text{-}14)$$

where x_i is the mole fraction of component i. The capital letter with the bold face is used to designate matrices and superscript (-1) means inverse of the matrix. It is more convenient to express mass diffusion flux in terms of mass fraction than mole fraction in numerical calculations. With the relation between mole fraction x_i and mass fraction w_i, mass diffusion flux $\vec{j}_k$ was expressed in terms of mass fraction w_i:

$$\vec{j}_k = -\sum_{i=1}^{\lambda-1} L_{ki} \nabla w_i - G_k \nabla \ln T \qquad (2\text{-}6)$$

where

$$L_{ki} = \left(\frac{1}{M_i} - \frac{1}{M_v} \right) \sum_{m=1}^{\lambda-1} \left(\mathbf{B}^{-1}\right)_{km} \frac{M^2}{M_m} w_m - \frac{M}{M_i} \left(\mathbf{B}^{-1}\right)_{ki}, \qquad (2\text{-}6a)$$

$$G_k = \sum_{i=1}^{\lambda-1} \left(\mathbf{B}^{-1}\right)_{ki} \left\{ \sum_{m \neq i}^{\lambda} \tilde{C}_{im} \left(\frac{D_m^T}{\rho_m} - \frac{D_i^T}{\rho_i} \right) \right\} \qquad (2\text{-}6b)$$

The above flux equation (Eq. 2-6) was applied to the species balance and gave Eq. 2-5.

One aspect is awkward with the above equation from a computational point of view. The density of a component may become zero at some point in the reactor model during the numerical modeling. This embarrassing situation is resolved by using

$\tilde{C}_{ik} = x_i x_k / D_{ik}$ or $\tilde{C}_{ik} = \rho_i \rho_k M^2 / \rho^2 D_{ik} M_i M_k$ and the matrix component B_{ik} is rewritten depending on cases and used in coding the reactor model.

$$B_{ik} = \begin{cases} -\sum_{j \neq i}^{\lambda-1} \frac{w_j M^2}{\rho D_{ij} M_i M_j} - \frac{(w_j + w_\lambda) M^2}{\rho D_{i\lambda} M_i M_\lambda} & \text{for } i = k \\ \frac{w_i M^2}{\rho M_i} \left(\frac{1}{D_{ik} M_k} - \frac{1}{D_{i\lambda} M_\lambda} \right) & \text{for } i \neq k \end{cases} \tag{2-15}$$

Similarly, the term G_k becomes as follows:

$$G_k = \sum_{i=1}^{\lambda-1} \left(B^{-1} \right)_{ki} \left\{ \sum_{m \neq i}^{\lambda} \frac{M^2}{\rho D_{im} M_i M_m} (w_i D_m^T - w_m D_i^T) \right\} \tag{2-16}$$

2.3.4 Property Estimation for Simulations

Properties of common gases are well reported, but those of metal organic sources and their reaction derivatives are scarcely or not available, while they are prerequisite in modeling MOCVD reactors. In most modeling studies of MOCVD processes, the necessary properties were estimated using the Chapman-Enskog theory. For example, the binary diffusivity, viscosity, and thermal conductivity are, respectively, given by the following equations [Bir60]:

$$D_{12} = 2.2680 \times 10^{-7} \frac{\sqrt{T^3 (M_1 + M_2)/2M_1 M_2}}{p \sigma_{12}^2 \Omega_{12}^D} \quad [\mathrm{m^2/s}] \tag{2-17}$$

$$\mu = 2.6693 \times 10^{-6} \frac{\sqrt{MT}}{\sigma^2 \Omega^\mu} \quad [\mathrm{Pa \cdot s}] \tag{2-18}$$

$$k = 8.322 \times 10^{-2} \frac{\sqrt{T/M}}{\sigma^2 \Omega^k} \quad [\mathrm{J/m \cdot s \cdot K}] \tag{2-19}$$

where σ and Ω's are the collision diameter (or characteristic diameter) and appropriate collision potentials. The collision integrals are mostly computed using the Lennard-Jones

(12-6) potential [Neu72] and then three physical properties can be estimated given the collision diameter (σ in Å) and characteristic energy (ε/k_B in Kelvin) of interaction between molecules. In this work, the following regression forms of collision integrals were used [Neu72]:

$$\Omega^D = \frac{1.06036}{T_*^{0.15610}} + \frac{0.19300}{e^{0.47635T_*}} + \frac{1.03587}{e^{1.52996T_*}} + \frac{1.76474}{e^{3.89411T_*}} \tag{2-20a}$$

$$\Omega^\mu = \frac{1.16145}{T_*^{0.14874}} + \frac{0.52487}{e^{0.77320T_*}} + \frac{2.16178}{e^{2.43787T_*}} \tag{2-20b}$$

where $T_* = k_B T/\varepsilon$. The two Lennard-Jones potential parameters (σ, ε/k_B) were estimated using the physical properties of the gas at its critical or boiling point:

$$\frac{\varepsilon}{k_B} = 0.77\,T_c \quad \text{and} \quad \sigma = 0.841\,V_c^{1/3} \tag{2-21a}$$

$$\frac{\varepsilon}{k_B} = 1.15\,T_b \quad \text{and} \quad \sigma = 1.18\,V_b^{1/3} \tag{2-21b}$$

where subscripts c and b, respectively, stand for the critical state and normal boiling point (i.e., 1 atm). The unit of molar volume is cm^3/mol in both equations. The liquid molar volume at the normal boiling point is usually estimated for MOCVD precursors and their reaction derivatives using additive methods [Hol92, Pol01].

The above property estimations are based on simple collisions and this approach is still valid for diffusivity and viscosity estimations of polyatomic molecules [Bir60]. The thermal conductivity estimation based on that assumption is not valid for polyatomic molecules because they have rotation and vibration motions as well as translation. A simple semi empirical method by Eucken [Euc13] was used for the thermal conductivity estimation in this study, instead of Eq. 2-19:

$$k = 2.6693 \times 10^{-3} \frac{\sqrt{T/M}}{\sigma^2 \Omega^{\mu}} \left(C_p + \frac{5}{4} R \right) \qquad [\mathrm{J/m \cdot s \cdot K}] \qquad (2\text{-}22)$$

Rotational and vibrational contributions to the heat capacities of metalorganic sources and their reaction derivatives were calculated based on quantum chemistry. This subject is further discussed in Chapter 3.

2.4 Penalty Finite Element Method

2.4.1 The Galerkin Method

For any differential governing equation, a residual of the equation can be defined, the value of which is zero for the exact solution in the domain Ω. Suppose that an incompressible flow problem is given and that its geometry has axisymmetry. In this case, the residuals are:

$$R_1 = \rho \left(u \frac{\partial u}{\partial r} + v \frac{\partial u}{\partial z} \right) + \frac{\partial p}{\partial r} - \frac{\partial \tau_{rr}}{\partial r} - \frac{\partial \tau_{rz}}{\partial z} - \frac{\tau_{rr} - \tau_{\theta\theta}}{r} - f_r \qquad (2\text{-}23a)$$

$$R_2 = \rho \left(u \frac{\partial v}{\partial r} + v \frac{\partial v}{\partial z} \right) + \frac{\partial p}{\partial z} - \frac{\partial \tau_{rz}}{\partial r} - \frac{\tau_{rz}}{r} - \frac{\partial \tau_{zz}}{\partial z} - f_z \qquad (2\text{-}23b)$$

$$R_3 = \frac{\partial u}{\partial r} + \frac{u}{r} + v \frac{\partial v}{\partial z} \qquad (2\text{-}23c)$$

where R_i 's are the residuals of the governing equations and ρ is the density of the fluid. In addition, u, v, p, f_r, and f_z are r- and z- components of velocity, pressure, and r- and z- components of body force. τ_{ij} is a component of the stress tensor in the cylindrical coordinates. The given problem is to find the solution (u, v, p) that makes the residuals null in the domain Ω. This strict requirement can be abated so as to find a solution that satisfies the following [Bur87]:

$$\int_{\Omega} R\,\mathrm{w}\,d\Omega = 0 \tag{2-24}$$

where R represents the three residual components in Eq. 2-23. In addition, the function w is a weight function or variation, and u, v, and p are the trial functions. Now, the original requirement was weakened in that the residuals are to be zero in a weighted average. By definition, a weight function or variation has the value of zero at the boundary of the domain Ω [Hug79, Pla84].

A weight function can be expressed in a linear combination of linearly independent functions, i.e. basis functions, if a set of basis functions is infinity, e.g. Fourier series expansion. Trial functions can also be expanded with an infinite set of basis functions. In any actual situation, of course, only a finite number of basis functions are used and therefore the obtained solution is only an approximation to the true solution. Of course, the larger a basis set is, the better the obtained solution is. Once all functions in Eq. 2-24 are substituted by linear combinations of corresponding sets of basis functions, solving the problem is changed to obtaining coefficients of the linear combinations. Trial and weight functions are not necessarily made up with the same set of basis functions. If the same basis set is used, the solution method is called the Galerkin method [Bur87].

$$\mathrm{u} = \sum_{i=1}^{M} \mathrm{u}_i \psi_i , \quad \mathrm{v} = \sum_{i=1}^{M} \mathrm{v}_i \psi_i , \quad \mathrm{p} = \sum_{i=1}^{N} \mathrm{p}_i \varphi_i \tag{2-25}$$

where ψ_i's and φ_i's are basis functions for velocities and pressure, respectively. For stability of a numerical solution procedure, ‘M’ is usually greater than ‘N’. With a Newtonian fluid and the Galerkin method, the following set of equations was obtained:

$$\sum_{j=1}^{M} \left(A_{ij} \mathrm{u}_j + B_{ij} \mathrm{v}_j \right) - \sum_{k=1}^{N} D_{ik} \mathrm{p}_k = x_i \tag{2-26a}$$

$$\sum_{j=1}^{M}\left(B_{ji}\,u_j + C_{ij}\,v_j\right) - \sum_{k=1}^{N} E_{ik}\,p_k = y_i \tag{2-26b}$$

$$\sum_{j=1}^{M}\left(D_{ji}\,u_j + E_{ji}\,v_j\right) = 0 \tag{2-26c}$$

where

$$A_{ij} = \langle r\psi_i \,|\, \rho u \psi_{j,r}\rangle + \langle r\psi_i \,|\, \rho v \psi_{j,z}\rangle + 2\langle r\psi_{i,r} \,|\, \mu \psi_{j,r}\rangle + \langle r\psi_{i,z} \,|\, \mu \psi_{j,z}\rangle + 2\left\langle \psi_i \,\middle|\, \frac{\mu}{r}\psi_j \right\rangle,$$

$$B_{ij} = \langle r\psi_{i,z} \,|\, \mu\psi_{j,r}\rangle, \quad D_{ik} = \langle \psi_i \,|\, \varphi_k\rangle + \langle r\psi_{i,r} \,|\, \varphi_k\rangle, \quad E_{ik} = \langle r\psi_{i,z} \,|\, \varphi_k\rangle,$$

$$C_{ij} = \langle r\psi_{i,r} \,|\, \mu\psi_{j,r}\rangle + 2\langle r\psi_{i,z} \,|\, \mu\psi_{j,z}\rangle + \langle r\psi_i \,|\, \rho u\psi_{j,r}\rangle + \langle r\psi_i \,|\, \rho v\psi_{j,z}\rangle,$$

$$x_i = \langle r\psi_i \,|\, f_r\rangle, \quad \text{and} \quad y_i = \langle r\psi_i \,|\, f_z\rangle$$

where the bracket symbol represents integration of its content over the domain and the subscript comma denotes a differentiation with respect to the followed independent variable.

There are also energy and species balance equations left in the model (Eqs. 2-4 and 2-5). Applying the Galerkin method to them gives:

$$\sum_{j=1}^{M} H_{ij}\,T_j = q_i \tag{2-27}$$

$$\sum_{k=1}^{M} K_{ik}^{j}\,w_k + \sum_{k=1}^{M} M_{ik}^{j}\,T_k = r_{G,i}^{j} + r_{S,i}^{j} \tag{2-28}$$

where

$$H_{ij} = \langle r\psi_i \,|\, \rho C_p u\psi_{j,r}\rangle + \langle r\psi_i \,|\, \rho C_p v\psi_{j,z}\rangle + \langle r\psi_{i,r} \,|\, k\,\psi_{j,r}\rangle + \langle r\psi_{i,z} \,|\, k\,\psi_{j,z}\rangle,$$

$$K_{ik}^{j} = \langle r\psi_i \,|\, \rho u\psi_{k,r}\rangle + \langle r\psi_i \,|\, \rho v\psi_{k,z}\rangle + \sum_{m=1}^{\lambda-1}\langle r\psi_{i,r} \,|\, L_{jm}\,\psi_{k,r}\rangle + \sum_{m=1}^{\lambda-1}\langle r\psi_{i,z} \,|\, L_{jm}\,\psi_{k,z}\rangle,$$

$$M_{ik}^{j} = \langle r\psi_{i,r} \,|\, G_j\,\psi_{k,r}\rangle + \langle r\psi_{i,z} \,|\, G_j\,\psi_{k,z}\rangle, \quad r_{G,i}^{j} = \langle r\psi_i \,|\, r_j\rangle,$$

$$r_{S,i}^{j} = -\left\langle\left\langle r\psi_i \middle| r_j^S \right\rangle\right\rangle, \quad \text{and} \quad q_i = \left\langle\left\langle r\psi_i \middle| k\frac{\partial T}{\partial r} + k\frac{\partial T}{\partial z} \right\rangle\right\rangle,$$

where the superscript j denotes that the equation is for species j and the double bracket symbol means surface integration over the boundary of the domain. The quantity q_i is energy gain at the boundary, e.g. radiation heat transfer in the current reactor model. L_{jm} and G_j are defined in Eq. 2-6.

Construction of basis functions is not specified in the above statements. For a simple geometry and a low dimensional problem, the construction brings no difficulties. This job becomes grave if the geometry of interest is complicated or its dimensionality is increased. A systematic way to build basis functions is necessary to deal with such cases. The finite element method is a viable method taking advantage of the concept of the finite element, a subregion of the domain. Basis functions are constructed over each finite element with the same basic rule for all elements, and therefore it is possible to deal with very complex geometry easily. If a domain is divided into finite elements, then Eq. 2-26 is applied to each finite element and the assembly of equations from each element gives whole equations to be solved for the whole domain.

2.4.2 Penalty Formulation

With proper boundary conditions, Eq. 2-26 in the previous section can be solved for (u, v, p). For a big problem, reducing one variable saves a lot of computational cost and time. Furthermore, explicit presence of the incompressibility constraint in the problem sometimes brings numerical difficulties [Gru89, Red93]. There is no pressure term in the continuity equation and therefore there are zero entities in the corresponding element positions in the whole matrix (see Eq. 2-26) and this causes difficulties sometimes, e.g. matrix inversion.

The continuity equation can be recognized as a constraint for the solution to satisfy. Solving a given problem, e.g. Eq. 2-26, is equivalent to minimizing the corresponding variational functional, the term $I(u, v)$ in Eq. 2-29, with constraints. It is possible to write this minimization problem in two different ways: the Lagrange multiplier method (Eq. 2-29) and the penalty functional method (Eq. 2-30).

$$L(u, v, \lambda) = I(u, v) + \int_{\Omega} \lambda\, G(u, v)\, d\Omega \tag{2-29}$$

$$J(u, v) = I(u, v) + \frac{\varepsilon}{2} \int_{\Omega} [G(u, v)]^2 \, d\Omega \tag{2-30}$$

where λ is the Lagrange multiplier and the functional G is a constraint, e.g. the continuity, and ε is the penalty parameter. It is shown that pressure is negative of the Lagrange multiplier [Red82]. With comparison of Eqs. 2-29 and 2-30, pressure has the following relationship with the continuity:

$$p = -\varepsilon \nabla \cdot \vec{v} \tag{2-31}$$

As shown in Eq. 2-30, the incompressibility constraint is more strictly enforced with a larger value of the penalty parameter ε. Weak formulation of Eq. 2-31 gives

$$\sum_{j=1}^{N} F_{ij}\, p_j = -\varepsilon \sum_{k=1}^{M} \left(D_{ki}\, u_k + E_{ki}\, v_k \right) \tag{2-32}$$

where $F_{ij} = \langle r\varphi_i | \varphi_j \rangle$ and the rest terms are defined in Eq. 2-26. Finally, the problem given in Eq. 2-26 becomes, in the vector and matrix form,

$$\mathbf{Au} + \mathbf{Bv} + \varepsilon\left[\mathbf{DF}^{-1}\mathbf{D}^{T}\mathbf{u} + \mathbf{DF}^{-1}\mathbf{E}^{T}\mathbf{v}\right] = \mathbf{x} \tag{2-33a}$$

$$\mathbf{B}^{T}\mathbf{u} + \mathbf{Cv} + \varepsilon\left[\mathbf{EF}^{-1}\mathbf{D}^{T}\mathbf{u} + \mathbf{EF}^{-1}\mathbf{E}^{T}\mathbf{v}\right] = \mathbf{y} \tag{2-33b}$$

where the bold face indicates that the symbols are column vector or matrix representations of the corresponding terms in Eqs. 2-26 and 2-32. In this set of equations, the continuity constraint and pressure terms are explicitly removed. Velocity components are efficiently calculated with this set of equations. Pressure could be calculated by the relationship given in Eq. 2-32 after the velocity field is obtained. It is explained in Eq. 2-30 that the larger penalty parameter ensures better enforcement of the constraint. Because of a limited number of digits in computers, too large penalty parameter can produce trivial solutions. The penalty terms in Eq. 2-33 end up with singular quantities due to reduced integration techniques and therefore, a penalty parameter that is too large makes the singular parts (penalty part) dominant in Eq. 2-33 and produces trivial solutions only ("locking" [Hei81]). Selection of a proper magnitude of the penalty parameter is discussed by Heinrich and Marshall [Hei81].

2.4.3 A Simple Test

The penalty formulation was tested with driven cavity flow in the Cartesian coordinates. The computational domain was $\{(x, y) \in 0 \leq x \leq 1 \ \& \ 0 \leq y \leq 1\}$ and no slip conditions were applied to all boundaries except at $y = 1$, i.e. the lid of the cavity at which velocity was set at (-1). The current results were compared in Figure 2-6 with previously reported results for the Reynolds number = 400.

Reported simulation results with 400 biquadratic elements are shown with empty circles (O) and the square markers were obtained with a similar number (480) of bilinear elements as in the biquadratic case. The bilinear results are not close to the reported velocity profile. The number of nodes with 400 biquadratic elements is 1681 and the same numbers of nodes are available with 1600 bilinear elements. The solid lines show good matches with the reported velocity profiles, where 2500 bilinear elements were used. For the current reactor model, using a large number of bilinear elements is preferred to using the same number of computational nodes with biquadratic elements, because the incompressibility condition was used in the penalty formulation (Eq. 2-33).

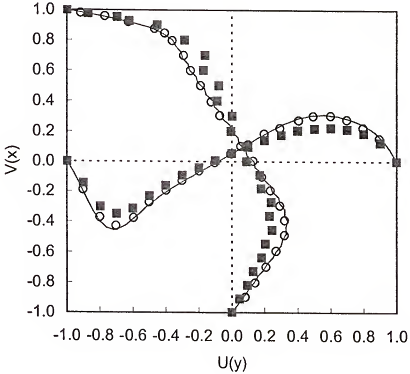

Figure 2-6. Velocity profiles at x = 0.5 (V) and y = 0.5 (U) for Re = 400. Symbols: o, 400 biquadratic elements [Hei81]; ■, 480 bilinear elements; solid line, 2500 bilinear elements.

2.5 Summary

Configuration of an up flow measurement reactor with which an *in situ* probing tool could be interfaced was presented, and a numerical model of the reactor was developed to describe momentum, heat, and mass transport in the reactor. In the model, the solid part as well as gas part of the reactor was considered to describe radiation heat transfer inside the reactor. In addition, both multi component diffusion and thermal diffusion were incorporated. To handle a set of PDE's and complex reactor geometry, a finite element description was used. The pressure term in the governing equation was removed using a penalty formulation to reduce computation cost. Finally, the FEM code was tested with the driven cavity flow.

CHAPTER 3
RAMAN SCATTERING AND COMPUTATIONAL CHEMISTRY

3.1 Introduction

MOCVD processes are influenced by numerous factors such as carrier gas, properties of the reactor wall, flow patterns inside the reactor, and thermal conditions. In addition, temperature variation within a MOCVD reactor is generally steep and therefore chemical changes of reactants occur very rapidly. To study reaction kinetics within a MOCVD reactor, in most cases, small amount of the reacting material is taken from the reactor through a sampling tube and analyzed apart from the reactor (*ex situ* analysis). Passing through the sampling tube, the sampled material containing active reaction intermediates experiences different conditions from those in the reactor and therefore different chemical paths are possibly followed. Consequently, what is observed with *ex situ* methods may not properly reflect actual phenomena within the reactor. For instance, decomposition of phospine (PH_3) was studied with *ex situ* and *in situ* techniques by several researchers [Abr91, Lar87, Luc88] and the observed decomposition behaviors of phospine showed strong dependence on the nature of a selected probing method (Figure 3-1). Therefore, *in situ* investigation of a process under actual conditions can give more adequate information of the process.

It is also important not to disturb the process to ensure correct information about it. For example, if temperature is to be measured with a thermocouple, then the presence of the thermocouple renders disturbances to the original flow pattern inside the reactor and subsequently the original temperature profile could be no longer available. In this aspect, non-intrusive probing is also required. Optical or spectroscopic probing can satisfy both requirements, i.e. *in situ* and non-intrusive probing. Raman spectroscopy has been a popular *in situ* technique to characterize the MOCVD process [Fot90a, Par02, Sed76, Sto86].

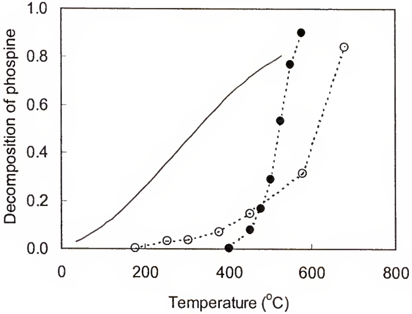

Figure 3-1. Observed decomposition behavior of phospine depending on probing methods. The solid line was obtained using *in situ* technique (Raman scattering [Abr91]) and the dotted lines were using *ex situ* methods; (●) mass spectroscopy [Lar87] and (O) coherent anti-Stokes Raman scattering (CARS) [Luc88].

Several optical or spectroscopic methods are available for *in situ* probing chemical changes. Concentration of intact metalorganic sources has been determined by UV/Vis spectroscopy (e.g., TMAl [Ito88], TMGa [Ibu89], TMIn [Hai83]). Electronic excitation is accompanied by changes in vibrational and rotational energies, and the resulting spectrum is complex and difficult to resolve even if the molecule is small. IR or Raman spectroscopy is also applicable to detecting those parent precursors. Peak positions are distinctive and useful for monitoring species.

Significantly less spectroscopic data are available on fragments of metalorganic sources. Monomethylgallium (MMGa) was observed by fluorescence spectroscopy [Mit85] but the spectrum was not distinctive enough to be used for quantitative analysis. Very little is known about the spectroscopy of dimethyl fragments of Group III metal-organic precursors. Atomic metals such as Ga, In, and Al could form as a result of decomposition. Ground states for Ga, In, and Al are commonly $^2P_{1/2}$ and $^2P_{3/2}$ and the first allowed excited electronic state is the $^2S_{1/2}$ state. Laser-induced fluorescence (LIF) offers the highest detection sensitivity [Heb90]. The transitions are, however, not easily accessible because they fall in the violet or UV regions. Spin-orbit splitting between the two ground states can be detected by electronic Raman scattering [Par02b, Vri75]. Splitting for Group III atoms are summarized in Table 3-1.

Table 3-1. Electronic transitions of Group III atoms.

Atom	$^2S_{1/2} \leftarrow {}^2P_{1/2}$ (cm^{-1})	$^2S_{1/2} \leftarrow {}^2P_{3/2}$ (cm^{-1})	Splitting (cm^{-1})
B	40040	40024	16
Al	25348	25235	113
Ga	24788	23962	826
In	24373	22160	2213

Gas phase decomposition of metalorganic precursors has also been analyzed *ex situ* by mass spectroscopy [Che91, Tho96, Yas85] and the results showed that stable hydrocarbon products include methane, ethane, and ethylene. These hydrocarbons are also detectable by Raman spectroscopy, but detection of radicals, e.g. CH_3, is difficult even though they have Raman-active vibrations, because radicals are expected to be in very low concentration. It was reported that methyl radicals were observed with IR-diode laser monitoring [Heb90].

Raman and IR spectroscopies have been popular in studying MOCVD reactions in terms of optical techniques. IR has been traditionally used for kinetics studies in many areas. IR is sensitive to changes in metal-carbon bonds during MOCVD reactions and therefore it is capable of following reactions in a MOCVD process. For example, reactions between TMGa and ammonia were studied at various temperature ranges with IR and the kinetic data were reported [Kim94, Maz89, Syw91]. Durig and co-workers [Dur82] reported IR and Raman spectra of $(CH_3)_3Ga:NH_3$ and $(CH_3)_3Ga:ND_3$ at 77 K and identified the peaks. Monteil *et al.* [Mon86] took Raman spectra of TMGa and arsine (AsH_3), and their reaction product and confirmed the formation of the gallium-asenic bond. These results were, however, mostly obtained under conditions far from those of actual MOCVD processes, i.e. high temperature and flow conditions.

Both IR and Raman have their own advantages [Ing88]. Efficiency of the IR absorption process is higher than that of Raman: cross-sections for IR and Raman processes are typically 10^{-18} and 10^{-29} cm^2, respectively. An observed IR signal contains, however, sum of all information from molecules present along the light path due to the nature of absorption. In contrast, in the Raman case, it is possible to focus a laser line at a specific position and this gives excellent spatial resolution. Raman scattering possibly provides thermal and species information at the same time, and its intensity is directly proportional to the number density of a scattering source. In addition, Raman detectors have short response time and that makes Raman spectroscopy a suitable technique to investigate intermediate species in reactions, even though the process efficiency is lower than IR. Advantages of Raman spectroscopy for reaction kinetic studies are available elsewhere [Has79].

Species identification using Raman (or IR) spectroscopy usually requires characteristic vibration frequencies. Parent metalorganic precursors can be easily tested to give characteristic vibrations. Identification of their reaction intermediates is, however, a more complex problem and is related with their reaction mechanism. Quantum chemistry can be useful to help identify observed vibrations of molecules formed during the reaction. Thermodynamic properties can also be estimated using quantum chemistry, and therefore more information is attainable to understand the reaction mechanism.

Raman intensity is directly proportional to the power of the light source as well as the number density of a selected species. Laser light sources are widely used for Raman scattering experiments because they give higher radiance than any other conventional light source. Conversely, this forte of laser sometimes could cause adverse effects during probing, e.g. heating and/or photolysis of the observed molecules. It was, however, reported that there was no discernable heating with an argon ion laser (488 nm) up to 5 W [Fot90a]. If a higher power light source is used, the heating effect should be tested. As for the photolysis, decomposition studies of TMAl, TMGa, and TMIn were reported [Beu91]. According to the results, TMAl and TMGa decompose if the light is more energetic than 290 nm. Therefore, visible light unlikely causes decomposition of metalorganic precursors.

3.2 Theoretical Background of Raman Scattering

Of oscillations of electric dipoles, magnetic dipoles, and their higher order multipoles, the oscillation of electric dipoles is the most important source of electromagnetic radiation used in Raman and IR spectroscopy. When a molecule experiences a transition between two specific quantum states, the specific electromagnetic wave associated with the transition is radiated. Analyzing the electromagnetic wave gives information about the molecule. For a specific spectroscopic technique, the transition moment tells whether the transition between states i and f is observable or not. Using the bracket notation, the transition moment is defined as $< f\,|\vec{\mu}|\,i >$ where $\vec{\mu}$ is the dipole moment and 'f' and 'i' represent the wave functions of the final and initial states, respectively. If the transition moment is zero, then the corresponding transition is not observable. This definition reveals that a constant dipole does not contribute to the transition moment and that only variations in the dipole moment can contribute. Such variations occur when vibrations of a molecule change the magnitude of the dipole moment or an induced dipole moment is produced by the interaction between a vibration mode of the molecule and an external electric field: the first case is the source of IR absorption and the second is that of Raman scattering.

3.2.1 Selection Rules for Raman Scattering

A partial quantum mechanical treatment [Lon77] gives an instructive picture of the scattering process. As mentioned previously, a transition between two quantum states of a molecule can be observed if the relevant transition moment $[\mu]_{fi}$ is not zero.

$$[\mu]_{fi} = \langle \psi_f | \hat{\mu} | \psi_i \rangle \tag{3-1}$$

A dipole moment may change upon vibrations of the molecule and this is relevant to the IR process. For a scattering process, an induced dipole moment is the source of electromagnetic radiation, which is expressed as $\vec{\mu} = \vec{\alpha} \cdot \vec{E}$ where $\vec{E}$ is the external (or incident) electric field vector and $\vec{\alpha}$ is the polarizability tensor of the molecule and its component upon the molecular vibration is expanded as

$$\alpha_{ij} = (\alpha_{ij})_0 + \sum_k \left(\frac{\partial \alpha_{ij}}{\partial Q_k} \right)_0 Q_k + \frac{1}{2} \sum_{l,m} \left(\frac{\partial^2 \alpha_{ij}}{\partial Q_l \partial Q_m} \right)_0 Q_l Q_m + \cdots \tag{3-2}$$

where the subscript '0' denotes the equilibrium configuration of the molecule and Q_j the normal coordinate of a vibration mode with frequency ν_j. The classical expansion of the polarizability tensor is useful in considering selection rules that predict observable scattering transitions. Assuming that the wavelength of the external electric field is sufficiently larger than the size of the molecule, the amplitude of the induced dipole moment is written as follows:

$$[\mu_0]_{fi} = \langle \psi_f | \tilde{\alpha} | \psi_i \rangle \cdot \vec{\mathbf{E}}_0 = [\tilde{\alpha}]_{fi} \cdot \vec{\mathbf{E}}_0 \tag{3-3}$$

where the subscript '0' denotes the amplitude of the quantity. If the incident radiation has (i) higher enough energy than rotational and vibrational states of the molecule, (ii) lower enough energy than electronic transition energy of the molecule, and (iii) the electronic ground state is not degenerate, then the vibration and/or rotation parts are separated from the electronic part [Lon77].

$$[\alpha_{xy}]_{fi} = \langle \phi_{v^f} \theta_{R^f} | \alpha_{xy} | \phi_{v^i} \theta_{R^i} \rangle \tag{3-4}$$

where α_{xy} is a space fixed component of the polarizability tensor, and ϕ and θ are the wave functions for vibration and rotation, respectively. The space fixed component can be expanded in terms of molecule fixed components.

$$\alpha_{xy} = \sum_{x',y'} \alpha_{x'y'} \cos(xx') \cos(yy') \tag{3-5}$$

Because α_{xy} is a function of vibration coordinates only, the matrix component $[\alpha_{xy}]_{fi}$ is written as

$$[\alpha_{xy}]_{fi} = \sum_{x',y'} \langle \phi_{v^f} | \alpha_{x'y'} | \phi_{v^i} \rangle \langle \theta_{R^f} | \cos(xx') \cos(yy') | \theta_{R^i} \rangle \tag{3-6}$$

With the harmonic oscillator approximation, a vibrational wave function is the product of harmonic wave functions (the Hermite polynomials) for each normal mode of vibration. Then, by using Eq. 3-2, the vibration part of Eq. 3-6 becomes

$$\langle \phi^f | \alpha_{x'y'} | \phi^i \rangle = (\alpha_{x'y'})_0 \left\langle \prod_m \phi_{v_m^f}(Q_m) \middle| \prod_m \phi_{v_m^i}(Q_m) \right\rangle$$

$$+ \sum_k \left(\frac{\partial \alpha_{x'y'}}{\partial Q_k} \right)_0 \left\langle \prod_m \phi_{v_m^f}(Q_m) \middle| Q_k \middle| \prod_m \phi_{v_m^i}(Q_m) \right\rangle + \cdots \qquad (3\text{-}7)$$

The first term of Eq. 3-7 corresponds to the Rayleigh scattering and the second to the Raman scattering and each process occurs if corresponding term is not zero. Properties of the eigenfunctions, i.e. the Hermite polynomials, dictate the selection rules for the scattering processe [Lon77]:

$$\left\langle \phi_{v_k^f}(Q_k) \middle| \phi_{v_k^i}(Q_k) \right\rangle = \delta_{v_k^f v_k^i} \qquad (3\text{-}8a)$$

$$\left\langle \phi_{v_k^f}(Q_k) \middle| Q_k \middle| \phi_{v_k^i}(Q_k) \right\rangle = \begin{cases} \sqrt{v_k^i + 1}\, b_k & \text{for } v_k^f = v_k^i + 1 \\ 0 & \text{for } v_k^f = v_k^i \\ \sqrt{v_k^i}\, b_k & \text{for } v_k^f = v_k^i - 1 \end{cases} \qquad (3\text{-}8b)$$

where $b_k^2 = h / 8\pi^2 c \tilde{v}_k$ where h and c are the Planck constant (= 6.626×10^{-34} Js) and speed of light (= 2.998×10^{10} cm/s), respectively. Eq. 3-8a is for the Rayleigh scattering, which is an elastic scattering. The Raman selection rule for vibrational transitions is $\Delta v_k = \pm 1$ as in Eq. 3-8b: the first case in Eq. 3-8b is called the Stokes Raman scattering and the third is the anti-Stokes Raman scattering. Similarly, for the second derivative terms in Eq. 3-7, the selection rules are $\Delta v_k = \pm 2$ for "overtone" transitions and $\Delta v_k = \pm 1$ and $\Delta v_l = \pm 1$ for "combination" transitions.

The second part of Eq. 3-6 governs rotational transitions and the eigenfunctions of rotational states are the spherical harmonics, characteristic of which gives the selection rule for rotational transitions of scattering: $\Delta J = 0$ or ± 2 where J is the rotational quantum number.

3.2.2 Intensity of Raman Scattering

The radiation intensity **I** due to the transition moment $[\mu_0]_{fi}$ is defined as

$$\mathbf{I} = k'_{\tilde{v}}\,\tilde{v}^4[\mu_0]^2_{fi}\sin^2\theta \tag{3-9}$$

where $k'_{\tilde{v}} = \pi^2 c / 2\varepsilon_0$ and μ_0 is the transition moment amplitude. $\tilde{v}$ is the wave number of the scattered radiation and ε_0 is the permittivity of free space (8.854×10^{-12} F/m). The angle θ represents the angle of observation (or detection) relative to the incident light. If the observation angle is 90°, the sine term is one. In the current study, the Raman equipment configuration takes advantage of this simplicity.

Suppose that illumination whose z-component only is not zero ($E_z \neq 0$ only) is along the y-axis and the scattered light is observed on the positive x-axis (this is the experimental configuration used throughout this work). For this experimental setup, the scattering plane is the xy-plane and the relevant components of the polarizability tensor are α_{yz} and α_{zz} only. Therefore, the observed intensity consists of two parts related to those polarizability components. For a molecule that undergoes Stokes Raman scattering, the two parts are

$$^{\perp}\mathbf{I}_{/\!/} = k'_{\tilde{v}}\,\tilde{v}^4(v^i_k + 1)b^2_{v_k}\overline{(\alpha'_{yz})^2_k}E^2_{z0} \tag{3-10a}$$

$$^{\perp}\mathbf{I}_{\perp} = k'_{\tilde{v}}\,\tilde{v}^4(v^i_k + 1)b^2_{v_k}\overline{(\alpha'_{zz})^2_k}E^2_{z0} \tag{3-10b}$$

where the subscripts // and $\perp$ denote directions of the scatter electric fields relative to the scattering plane and the bar represents the space average of its underneath term, and Eqs. 3-7 to 3-9 were used here. The prime (') on the polarizability component means the derivative with respect to the kth vibration coordinate (Eq. 3-7). There are *N* randomly oriented molecules in a detection volume in practice. In this case, the following sum is necessary to obtain intensity. The Harmonic oscillator approximation is assumed in this summation.

$$N\sum_{\mathrm{i}}(\mathrm{v}_{\mathrm{k}}^{\mathrm{i}}+1)f_{\mathrm{v}_{\mathrm{k}}^{\mathrm{i}}}=\frac{N}{1-\exp(-\mathrm{hc}\tilde{\mathrm{v}}_{\mathrm{k}}/\mathrm{k_B T})} \tag{3-11}$$

where $f_{\mathrm{v}_{\mathrm{k}}^{\mathrm{i}}}$ is the fraction of molecules in vibrational state $\mathrm{v}_{\mathrm{k}}^{\mathrm{i}}$ and the Boltzmann distribution is used. With this result, Eq. 3-10 becomes

$$^{\perp}\mathbf{I}_{//}=N\,\frac{\tilde{\mathrm{v}}^{4}\,\mathrm{h}\,\mathrm{k}'_{\tilde{\mathrm{v}}}\,\overline{(\alpha'_{yz})_{\mathrm{k}}^{2}}\,\mathrm{E}_{z0}^{2}}{8\pi^{2}\mathrm{c}\,\tilde{\mathrm{v}}_{\mathrm{k}}[1-\exp(-\mathrm{hc}\tilde{\mathrm{v}}_{\mathrm{k}}/\mathrm{k_B T})]} \tag{3-12a}$$

$$^{\perp}\mathbf{I}_{\perp}=N\,\frac{\tilde{\mathrm{v}}^{4}\,\mathrm{h}\,\mathrm{k}'_{\tilde{\mathrm{v}}}\,\overline{(\alpha'_{zz})_{\mathrm{k}}^{2}}\,\mathrm{E}_{z0}^{2}}{8\pi^{2}\mathrm{c}\,\tilde{\mathrm{v}}_{\mathrm{k}}[1-\exp(-\mathrm{hc}\tilde{\mathrm{v}}_{\mathrm{k}}/\mathrm{k_B T})]} \tag{3-12b}$$

Degeneracy was not considered during the derivation of Eq. 3-12. If vibration mode k has a degeneracy of g_{k}, the observed intensity will be g_{k} times as intense as the above results (Eq. 3-12). The sum of two terms in Eq. 3-12 is an experimentally observed intensity and ratio of the two gives information on the molecular geometry.

The scattering intensity for rotation is similarly calculated. In the rotation case, energy spacing is not constant as in the harmonic oscillator assumption and therefore a summation similar to Eq. 3-11 is not necessary.

$$^{\perp}\mathbf{I}_{//}=\mathrm{k}'_{\tilde{\mathrm{v}}}\,\tilde{\mathrm{v}}^{4}_{\mathrm{v',J';v'',J''}}\,N_{\mathrm{v'',J''}}\,\overline{[\alpha_{yz}]^{2}_{\mathrm{v',J';v'',J''}}}\,\mathrm{E}_{z0}^{2} \tag{3-13a}$$

$$^{\perp}I_{\perp} = k'_{\tilde{\nu}}\, \tilde{\nu}^{4}_{v',J';v'',J''} N_{v'',J''} \overline{[\alpha_{zz}]^{2}_{v',J';v'',J''}} E^{2}_{z0} \tag{3-13b}$$

where v" and J" are respectively initial states for vibration and rotation transitions and the terms with bar are space-averaged squares of transition polarizability components. For diatomic molecules, the space-averaged squares are reported [Lon77]. $N_{v,J}$ is the number of the molecules in state (v, J). For initial state (0, J),

$$N_{J} = N \frac{g_{J}(2J+1)\exp[-F(J)hc/k_{B}T]}{\sum_{J} g_{J}(2J+1)\exp[-F(J)hc/k_{B}T]} \tag{3-14}$$

where F(J) is the rotational term. g_J is the degeneracy due to the nuclear spin statistics and should be considered when the molecule has a center of symmetry [Ber95, Lon77]. The term $(2J+1)$ is the degeneracy for rotational state J. For the ground vibrational state, the rotational term F(J) is

$$F(J) = B_{0}J(J+1) - D_{0}J^{2}(J+1)^{2} + \cdots \tag{3-15}$$

where B_0 is the rotational constant and D_0 the centrifugal distortion constant. The subscript '0' denotes that the vibrational quantum number is zero. In the current study, temperature is determined by using rotational transitions at the vibrational ground state. In Eq. 3-15, the first term is from the rigid rotor approximation and the second and higher order terms account for nonrigidity. For nitrogen, the values of B_0 and D_0 are 1.989574 and 5.76×10^{-6} cm^{-1}, respectively [Ben74]. This means that the rigid rotor approximation is valid for nitrogen.

3.3 Applications of Raman Scattering

3.3.1 Raman System

A schematic diagram of the Raman system used in this work is depicted in Fig. 3-2. The Raman system consisted of laser line sources, optical circuit to provide photons to excite sample molecules, macro chamber, spectrometer, detector, and recorder. This system was also capable of solid-state Raman micro probing.

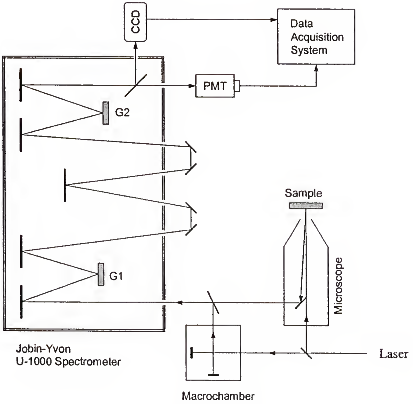

Figure 3-2. Schematic of the Raman system.

Two kinds of light sources were available: a solid-state laser (Verdi-8, Coherent Lasers) and an argon ion laser (Innova 90, Coherent Lasers). The solid-state laser had a single line emission at 532 nm and the argon ion laser mainly produced a 488 or 514 nm line, depending on the wavelength selection. A laser line was directed by the optical circuit and focused by a lens (focal length = 110 mm) into the macro chamber where a reactor or a gas flow cell was located. Raman scattering signals from the sample were collected at right angle to the incident laser line and reflected into the spectrometer (U-1000, Jobin-Yvon). The spectrometer was equipped with two gratings denoted G1 and G2 in Figured 3-2, which had a groove density of 1800 lines/mm. This spectrometer covers the spectral range from 440 to 750 nm. Scattered light is thereby dispersed and then observed with either a photo multiplier tube (PMT) or charge coupled device (CCD). Finally, electric signals from either of the detectors are processed on a personal computer. Spectral position of the spectrometer was calibrated by using the mercury emission line at 546.074 nm before every experiment.

Spectral resolution. The spectral resolution of a spectrometer is determined by the spectral bandpass related to the dispersion characteristics of the spectrometer. If the slit width is not small, aberration and diffraction effects caused by the slit are negligible and spectral bandpass is determined geometrically [Ing88] and that is called geometric spectral bandpass, s_g. The geometric spectral bandpass is given by

$$s_g = R_d W_s \tag{3-16}$$

where R_d and W_s are the reciprocal linear dispersion and slit width, respectively. The reciprocal linear dispersion is determined by the setup of a specific spectrometer. For U-1000, the value was 0.243 nm/mm at 514.5 nm. As a typical example, slit width setting to 100 μm gives a geometric spectral band pass of 0.0243 nm. The spectral resolution is calculated by

$$\Delta\tilde{v} = \left(\frac{1}{514.532} - \frac{1}{514.532 + 0.0243} \right) \times 10^7$$
$$\approx 0.9 \quad [\mathrm{cm}^{-1}]$$

for the 514 nm line of an argon ion laser. Spectral resolutions were calculated for several combinations of the slit width and laser line (see Table 3-2).

Table 3-2. Calculated spectral resolutions (cm^{-1}).

Wavelength Slit width	488 nm	514 nm	532 nm
100 μm	1.0	0.9	0.9
200 μm	1.9	1.8	1.8
400 μm	3.9	3.7	3.5

Focal cylinder. To increase the spatial resolution of the Raman system and observed scattering intensity, the excitation line was focused by a lens. It is known that a laser beam is focused in a cylindrical shape, i.e. focal cylinder, and its diameter (D) and length (L) are given by the following equations [Lon77]:

$$D = 4\lambda f / \pi d \tag{3-17a}$$

$$L = 16\lambda f^2 / \pi d^2 \tag{3-17b}$$

where λ, f, and d are, respectively, the wavelength of the laser, focal length of the lens, and diameter of the laser line before focusing. For example, if f, d, and λ are respectively 110 mm, 3 mm, and 488 nm, then the diameter the focal cylinder is 0.023 mm and its length is 3.34 mm. This gives a volume of 1.4×10^{-3} mm^3 and for an ideal gas at 1 atm a total of 3.7×10^{13} molecules are detected.

3.3.2 Temperature Determination

3.3.2.1 Formulation

A rotational state distribution of gas molecules is governed by temperature as shown in Eq. 3-14. Conversely, the temperature of the gas can be extracted from a measured distribution of the rotational states of the gas molecules. There are several reports on the determination of temperature profiles in MOCVD reactors with Raman spectroscopy [Kop84, Mon86, Par02]. It was reported that temperature measurements using rotational state distribution could be accurate with less than 5 % uncertainty in the range 10 to 3000 K [Dra82].

Rotational transitions at the ground state of vibration are generally used for temperature measurements and therefore vibration quantum numbers can be dropped. For Stokes Raman scattering, the observed intensity **I** is

$$\mathbf{I} = \left(\tilde{\nu}_0 - \tilde{\nu}_{J+2,J}\right)^4 \frac{g_J\,(2J+1)\exp[-F(J)hc/k_B T]}{\sum_J g_J\,(2J+1)\exp[-F(J)hc/k_B T]} N \frac{7}{45} \frac{3(J+1)(J+2)}{2(2J+1)(2J+3)} C_0 \qquad (3\text{-}18)$$

where $\tilde{\nu}_0$ is the wave number of the incident light and C_0 is a constant $(= k_{\tilde{\nu}}^{\cdot}\gamma_0^2 E_{z0}^2)$ under given experimental conditions. The intensity of a rotational transition is the sum of the two parts in Eq. 3-13 and spaced-averaged squares of transition probability components are expressed with the rotational quantum number J [Lon77]. A few correction factors to this equation are needed to account for non-ideality. Every spectroscopy system has its own spectral response as a function of wavelength. In addition, the anisotropy γ_0^2 is influenced by the centrifugal distortion of the molecule. With these considerations, the observed intensity is finally expressed as follows:

$$\mathbf{I} = \left(\tilde{\nu}_0 - \tilde{\nu}_{J+2,J}\right)^4 \frac{\mathrm{g}_J \cdot (2J+1) \cdot \exp[\text{-}\mathrm{F}(J)\mathrm{hc}/\mathrm{k_B T}]}{\sum_J \mathrm{g}_J \cdot (2J+1) \cdot \exp[\text{-}\mathrm{F}(J)\mathrm{hc}/\mathrm{k_B T}]} N \frac{7}{45} \frac{3(J+1)(J+2)}{2(2J+1)(2J+3)} \mathrm{C}_0$$

$$\times R(J;\tilde{\nu}_0) \cdot f(J) \qquad (3\text{-}19)$$

where $R(J;\tilde{\nu}_0)$ is the spectral response of the spectrometer and $f(J)$ is the correction to the anisotropy (γ_0^2) of the polarizability. $R(\tilde{\nu})$ is an equipment-specific quantity and it is determined experimentally using a well-known light source such as a tungsten strip lamp. An expression for $f(J)$ is theoretically given as the following form:

$$\mathrm{f}(J) = 4\chi^{-1} (\mathrm{B_e}/\omega_e)^2 [J(J+1) + (J+2)(J+3)] \qquad (3\text{-}20)$$

where χ and $\mathrm{B_e}/\omega_e$ are respectively 0.45 and 8.476×10^{-4} for nitrogen [Asa80]. By taking the natural logarithm of Eq. 3-19 and rearranging the result, the following is obtained:

$$\ln\left\{\frac{(2J+3)\mathbf{I}}{\left(\tilde{\nu}_0 - \tilde{\nu}_{J+2,J}\right)^4 \mathrm{g}_J (J+1)(J+2)\, R(J;\tilde{\nu}_0) f(J)}\right\} = \mathrm{C}_1 - \frac{\mathrm{F}(J)\mathrm{hc}}{\mathrm{k_B T}} \qquad (3\text{-}21)$$

where $\mathrm{C}_1 = \ln\left\{7N\mathrm{C}_0 / 30 \sum_J \mathrm{g}_J (2J+1) \exp[\text{-}\mathrm{F}(J)\mathrm{hc}/\mathrm{k_B T}]\right\}$ and this quantity is a constant for a given experimental setup. Therefore, if the spectral response $R(\tilde{\nu})$ and the correction to the anisotropy, $f(J)$, are known, the temperature is determined with the linear regression method from a set of rotational peaks. At high temperature, population at the next excited vibrational state increases and another correction for that should be included as well as $R(\tilde{\nu})$ and $f(J)$. For nitrogen, this correction is not necessary up to around 10^3 K [Dra82] due to its high vibration frequency (2331 cm^{-1}).

3.3.2.2 Applications

The rotational Raman spectrum in Figure 3-3a was obtained from pure nitrogen at 23.6 °C, which was separately measured with both a mercury thermometer and a k-type thermocouple. The first peak on the spectrum is for rotational quantum number J = 2. To protect the detector, lower transitions were not observed. With application of the aforementioned procedure (Eq. 3-21), a good linear relationship was produced (Figure 3-3b).

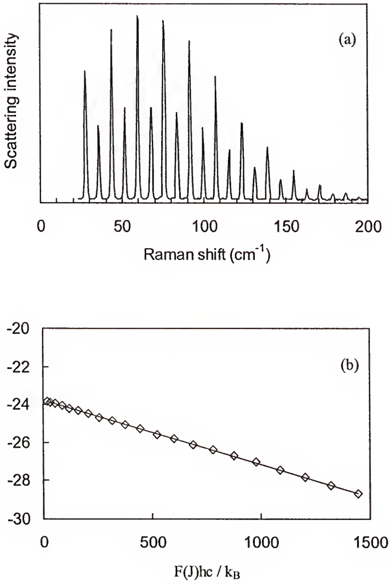

Figure 3-3. Temperature determination: (a) a rotational Raman spectrum of nitrogen taken at 23.6 °C and (b) application of the relationship given in Eq. 3-21. The temperature is obtained from the slope of the straight line.

The temperature obtained from this procedure was 23.7 ± 0.8 °C, which was a very good match with 23.6 °C. It should be noted from the figure that rotational transitions with higher quantum numbers more significantly contributed to the accuracy of the temperature determination. The intercept in Figure 3-3b also contains the temperature information as shown in Eq. 3-21. Using the intercept, however, requires a quantitative determination of C_1, which is specific to a experimental setup, while the slope does not have any setup-specific information.

When nitrogen is mixed with other gases, some of nitrogen rotation peaks may overlap with peaks from other species and those peaks should be excluded from the temperature estimation. A typical example of such a situation occurs when nitrogen is mixed with ammonia, which is a popular nitrogen source for nitride semiconductor materials.

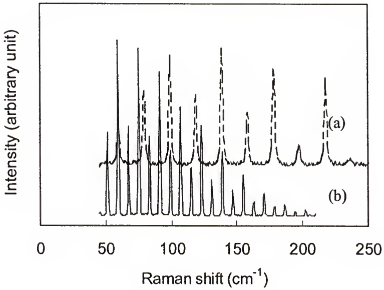

Figure 3-4. Overlap of spectra in the nitrogen rotation band: (a) ammonia and (b) nitrogen.

3.3.3 Concentration Determination

3.3.3.1 Formulation

There is a common structure within Eqs. 3-12 and 3-13: $\mathbf{I} \propto N(\partial\sigma/\partial\Omega)$ where the term in the parentheses is the differential cross-section at a specified observation angle (=90 ° throughout this work) with respect to the incident laser line and the term is a function of the incident light and temperature of the scattering molecule. For the vibration case, the differential cross-section is deduced from Eq. 3-12 as follows:

$$\left(\frac{\partial\sigma}{\partial\Omega}\right)_k = C_k \frac{(\tilde{v}_0 - \tilde{v}_k)^4}{\tilde{v}_k[1 - \exp(-hc\tilde{v}_k/k_B T)]} \qquad (3\text{-}22)$$

where C_k is a constant, which contains specific information of the k^th^ vibration mode. The value of C_k is determined by performing experiments with a known concentration and then the absolute cross-section for the vibration can be obtained. In practice, cross-sections are usually reported relative to that of the Q-branch of nitrogen at 2331 cm^{-1} because nitrogen is sufficiently stable to be an internal standard and the cross-section of nitrogen closely follows the $(\tilde{v}_0 - \tilde{v}_k)^4$ dependence in the visible wavelength region [Sch79]. In the ultraviolet region, however, resonance enhancement ordinarily comes in and Eq. 3-22 is no longer valid. With the nitrogen Q-branch standard, the relative cross-section Σ_k for vibration mode k is defined as

$$\Sigma_k = \frac{C_k\,\tilde{v}_Q}{C_Q\,\tilde{v}_k} = \frac{(\partial\sigma/\partial\Omega)_k}{(\partial\sigma/\partial\Omega)_Q} \frac{(\tilde{v}_0 - \tilde{v}_Q)^4}{(\tilde{v}_0 - \tilde{v}_k)^4} \frac{1 - \exp(-hc\tilde{v}_k/k_B T)}{1 - \exp(-hc\tilde{v}_Q/k_B T)} \qquad (3\text{-}23)$$

The relative cross-section defined in Eq. 3-23 is nearly independent of experimental conditions such as temperature and wavelength of the incident light. The spectral response, $R(\tilde{\nu})$, of the spectrometer must be incorporated in calculations when measured intensities are dealt with, because $\tilde{\nu}_k$ and $\tilde{\nu}_Q$ are usually different.

When mass dispersion or reaction kinetics is investigated with Raman spectroscopy, a relationship between the Raman intensity ratio and the number density ratio for two components is necessary to calculate the concentration in a detection region. One of two components is assumed to be an internal standard for simplicity. Using Eqs. 3-12 and 3-23, the number density ratio of components j and Q is related to their intensity ratio (Eq. 3-24).

$$\frac{N_Q}{N_j} = \frac{(\tilde{\nu}_0 - \tilde{\nu}_j)^4}{(\tilde{\nu}_0 - \tilde{\nu}_Q)^4} \frac{1 - \exp(-hc\tilde{\nu}_Q/k_B T)}{1 - \exp(-hc\tilde{\nu}_j/k_B T)} \frac{\mathbf{I}_Q}{\mathbf{I}_j} \Sigma_j \tag{3-24}$$

where N_k and $\mathbf{I}_k$ are the number density and measured intensity of component k, respectively. Then, for a binary system, the mole fraction of component j is given by

$$x_j = \frac{N_j}{N_j + N_Q} \ . \tag{3-25}$$

3.3.3.2 Applications

The relative Raman cross-section was experimentally determined for three gas mixtures: 28.8% NH_3/N_2, 71.7 % H_2/N_2, and 22.6 % NH_3/H_2. The characteristic vibration frequencies of N_2, NH_3, and H_2 are 2331, 3335, and 4157 cm^{-1}, respectively. Relative Raman cross-sections are usually reported with respect to the nitrogen Q-branch at 2331 cm^{-1}. However, the third mixture (NH_3/H_2) was included here because the first component has a lower characteristic vibration frequency than the second.

An aluminum flow cell with quartz windows in four directions was used for these experiments (Figure 3-5) to remove transport issues. The temperature of the flow cell was controlled to investigate thermal effects on experimentally observed relative Raman cross-sections. To establish homogeneous thermal conditions, the stainless gas lines and the flow cell body were wound with a heating tape and a heating power was maintained constant during the experiments. The mixture concentrations were controlled by adjusting mass flow controllers and the 532 nm line was used as the excitation light source in these experiments.

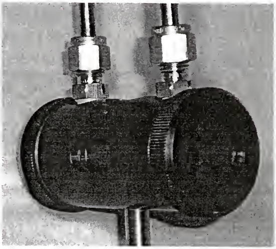

Figure 3-5. A gas flow cell used in the Raman cross-section study.

Table 3-3. Apparent relative Raman cross-sections for three gas mixtures.

	Apparent cross-section	Change (%)	Temperature (^oC)	Vibrations (cm^{-1})
28.8 % NH_3/N_2	4.529 ± 0.005	0	24	3335 / 2331
	4.194 ± 0.001	-7.4	80 ± 3	
	3.999 ± 0.003	-11.7	114 ± 2	
71.7 % H_2/N_2	1.251 ± 0.010	0	24	4157 / 2331
	1.141 ± 0.012	-8.8	80 ± 1	
	1.076 ± 0.011	-14.0	113 ± 1.5	
22.6 % NH_3/H_2	3.169 ± 0.006	0	24	3335 / 4157
	3.242 ± 0.006	+2.3	80 ± 2	

Using Eqs. 3-24 and 3-25, relative Raman cross-sections were determined from experimental measurements of scattering intensities. The results are summarized in Table 3-3. The temperatures in Table 3-3 were calculated from rotational spectra of nitrogen except for the NH_3/H_2 case, where the temperature was obtained from a rotational band of hydrogen. It is obvious from the table that obtained relative Raman cross-section values depend on heating. The results show a tendency that a larger difference in vibration frequencies between constituents gives a larger change in apparent relative Raman cross-section values. Each of the three gas species has high vibration frequency compared to the available thermal energy at the experimental condition and therefore vibrational excitations are not responsible for the tendency. In addition, any conformational changes of the gas species are not plausible at the experimental conditions. Therefore, it seems reasonable that the observed changes in the relative Raman cross-sections were not originated from the gas species themselves.

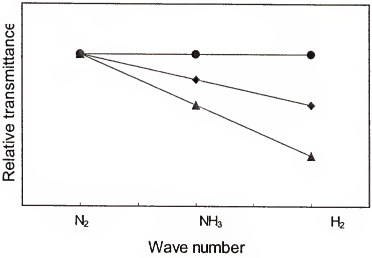

Figure 3-6. Hypothetical spectral transmittance of quartz at (●) low, (◆) medium, and (▲) high temperature. Transmittance values are normalized with that of nitrogen.

In the current experimental setup, scattered signals passed through a quartz window of the gas flow cell before they entered the spectrometer, and transmittance changes of the quartz upon heating could give changes in the observed cross-section values. The spectral transmittance of quartz is well reported at room temperature and shows a decreasing behavior in the long wavelength region [Ing88], while its higher temperature behavior is not available. Suppose that transmittance of the quartz decreases upon heating and it is a decreasing function of the wavelength of passing light: this hypothesis is schematically depicted in Figure 3-6. The tendency observed in the experiments can be explained with Eq. 3-24 and the hypothesis described in Figure 3-6. Therefore, optical properties of quartz should be carefully examined when it is used at high temperature.

3.4 Computational Chemistry

Raman spectroscopy was used to probe processes in an up flow cold-wall CVD reactor, which is known to render species information as well as temperature. Species information was obtained from the pertinent peak position and intensity of the peak in this work. In principle, Raman shift position and intensity of a vibration mode and, further, thermodynamic properties of the molecule can be calculated in view of computational chemistry [Cra02, Lev91, Sza89]. For a molecule, its quantum states are described by wave functions of the following eigenvalue problem:

$$\hat{\mathrm{H}}(\vec{\mathbf{R}},\vec{\mathbf{r}})\Psi(\vec{\mathbf{R}},\vec{\mathbf{r}}) = \mathrm{E}\,\Psi(\vec{\mathbf{R}},\vec{\mathbf{r}}), \tag{3-26}$$

where $\hat{\mathrm{H}}$ and Ψ are, respectively, the Hamiltonian of the molecule and its eigenfunction. Vectors $\vec{\mathbf{R}}$ and $\vec{\mathbf{r}}$ are position vectors of nuclei and electrons, respectively. By the Born-Oppenheimer approximation, motions of electrons are assumed to be independent of those of nuclei, and the Hamiltonian can be separated into two parts for nuclei and electrons and the original wave function is expressed as a product of two separate parts ($\chi(\vec{R})$ and $\varphi(\vec{r})$). The nuclei part of the wave function $\chi(\vec{R})$ is further represented as a product of the translational, vibrational, and rotational parts: $\chi(\vec{R}) = \chi_{cm}\chi_{vib}\chi_{rot}$. Accordingly, energy of the nuclear part consists of three contributions:

$$E_N = \frac{3n^2h^2}{8mV^{2/3}} + h\sum_{i=1}^{3N-5(6)} \nu_e\left(v_i + \frac{1}{2}\right) + \frac{J(J+1)h^2}{8\pi^2 I} \tag{3-27}$$

where n, v_i, J, and h are the translational, vibrational, rotational quantum numbers, and Planck constant, respectively. ν_e, m, and V are the equilibrium vibration frequency, mass of the molecule, and volume, respectively. In addition, all components of moment of inertia were assumed identical in x, y, and z-directions for simplicity, and the Harmonic oscillator approximation was used in Eq. 3-27.

The electronic part should be considered to produce the total energy of the molecule. The electronic Hamiltonian ($\hat{H}_{el}$) is written in Eq. 3-28 in atomic unit.

$$\hat{H}_{el}(\vec{r};\vec{R}) = -\sum_{i=1}^{N_e}\left(\frac{1}{2}\nabla_i^2 + \sum_{\alpha=1}^{N}\frac{Z_\alpha}{r_{\alpha i}}\right) + \sum_{i<j}\frac{1}{r_{ij}} \tag{3-28}$$

where N_e, N, and Z_α respectively designate the numbers of electrons and nuclei in the molecule and the charge number of the α^{th} nucleus. Indices i and j are used for electrons and $r_{ij} = r_j - r_i$. This Hamiltonian is parametrically dependent on the nuclei positions ($\vec{R}$) due to the Born-Oppenheimer approximation. The eigenvalue problem with this electronic Hamiltonian has been numerically treated with several techniques [Cra02, Lev91, Sza89]. Throughout this work, a computational chemistry tool, *Gaussian 03* [Fri03] was used to solve this kind of eigenvalue problems with affordable techniques. Some issues to be considered in computation are addressed in the following.

3.4.1 Vibration Frequency

Every atom in a molecule is constantly moving around its equilibrium position. These motions in a molecule are characterized with normal modes of the vibrations and they are useful in identifying chemical species. Each normal mode frequency can be calculated from the shape of the potential energy surface corresponding to the vibration.

3.4.1.1 Harmonic vibration

Harmonic vibrational frequencies are determined from the shape of the corresponding potential energy surface at its bottom using the Harmonic oscillator approximation. Calculated vibration frequencies are useful in identifying observed peaks and experiments can be conducted efficiently with expected vibrational frequencies. Especially, reaction intermediates of metalorganic precursors are usually unstable and therefore their spectral positions are frequently not available in literature and quantum chemistry calculations are the only way to obtain information before experiments. As an example, frequency calculation results for TMIn and monomethylindium (MMIn) are presented in Table 3-4. The calculations were done with two kinds of model chemistry.

Table 3-4. Experimental and calculated vibrational frequencies (cm^{-1}).

	MP2/LanL2DZ [Hay85, Dun77]		B3LYP/Gen*	
	TMIn	MMIn	TMIn	MMIn
$\nu(\text{In-C})_{\text{observed}}$	476	430	476	430
$\nu(\text{In-C})_{\text{calculated}}$	463	415	477	432
Scale factor	1.028 →		0.998 →	
$\nu(\text{In-C})_{\text{expected}}$	476	427	476	431

*Gen: SDB-aug-cc-pVTZ [Ber93, Mar01] for indium and 6-311++G(2d,2p) [Kri80] for carbon and hydrogen.

The scale factors in the table were obtained by comparing experimental and calculation results for TMIn, and the same scale factor was used to predict the vibration frequency of MMIn. For both model chemistry cases, the calculations give good expectation values when the scale factors are used. If the shape of the potential surface is exactly described by a selected model chemistry, the scale factor will be one. Scale factors depend on the level of theory and basis sets used in the calculation and they have been extensively studied [Sco96]. It should, however, be mentioned that a scale factor is not universal. Each scale factor shown in Table 3-4 is only good for the In-C stretching vibration with the given model chemistry. Therefore, the scale factors in the table may not valid for the C-H vibration in similar molecules.

3.4.1.2 Hot band transition

In the above calculations, the harmonic oscillator approximation was used and it is a reasonable assumption for most of the low temperature situations. Potential energy surfaces are, strictly speaking, not harmonic and hot band transitions appear at different spectral positions from its fundamental position at elevated temperature. The harmonic oscillator approximation works fine for light molecules, e.g. N_2 and H_2, because their vibrational frequency is very high and the population in the first excited state is very small even at quite high temperature. The harmonic oscillator approximation would, however, give considerable error for metalorganic molecules, because heavy atoms are present in the molecules and therefore its vibration excitation can take place at normal MOCVD temperatures. In these cases, it is meaningful to investigate the effects of anharmonicity of the potential energy surface on hot band transitions.

The Morse potential is simple and capable of describing anharmonicity:

$$V(r) = D\left(1 - e^{-\beta(r - r_e)}\right)^2 \tag{3-29}$$

where r_e is the equilibrium bond distance. The Morse potential shows anharmonicity in its shape and dissociation limit at $V(r) = D$ as the bond distance $r \to \infty$. In addition, it is known [Tow75] that 1-D Schrödinger equations are analytically solvable when the potential well is described by the Morse potential. The eigenvalues are

$$\frac{E}{hc} = G(v) = \omega_e\left(v + \frac{1}{2}\right) - \omega_e\chi_e\left(v + \frac{1}{2}\right)^2 + \ldots \tag{3-30}$$

where

$$\omega_e = \beta\sqrt{\left(\frac{Dh \times 10^2}{2\pi^2 c\mu}\right)} \quad \text{and} \quad \omega_e\chi_e = \frac{h\beta^2 \times 10^2}{8\pi^2 \mu c}$$

and 'v' is the vibrational quantum number. D and β are in cm^{-1} and all the others in SI units in the above equation. With the energy expression given above, the hot band transition can be calculated as well as the fundamental transition. Rotation terms were ignored in the energy given in Eq. 3-30.

The above procedure was applied for the symmetric In-C vibration of TMIn. A potential energy curve was calculated with the MP2/LanL2DZ chemistry. In this investigation, the symmetric stretching of In-C bond was considered and the potential energy curve was constructed by changing the bond distance. The *ab initio* calculation results were divided by three because there are three equivalent In-C bonds in TMIn (see Figure 3-7). Accordingly, the reduced mass used here was 15.024, which is the mass of CH_3.

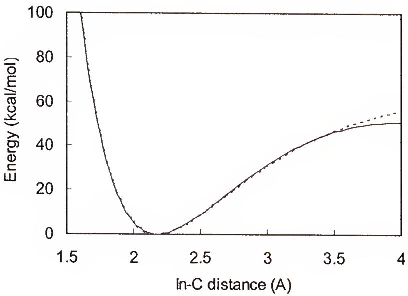

Figure 3-7. Curve fitting the calculated potential (—) with the Morse potential (---).

Even though the Morse potential gives a better description of anharmonicity of the potential curve than the Harmonic approximation, it also deviates at longer bond distances. The dashed line in Figure 3-7 was obtained from the Morse potential with the following parameters:

$D = 0.1050985$ Hartree
$\beta = 1.4048724$ $Å^{-1}$
$V_0 = -40.29655$ Hartree

After applying the scaling factor of 1.0636, the harmonic term (ω_e) and anharmonic term ($\omega_e \chi_e$) were determined to be 480.7 and 2.35 cm^{-1}, respectively. Vibrational transitions, including hot bands, can be estimated using the following equation:

$$\Delta G(v) = \omega_e - 2\omega_e \chi_e (v+1) \qquad (3\text{-}31)$$

with the obtained parameters. Using this equation, vibrational transitions of TMIn are expected at 476, 471, 467 cm^{-1}, etc.

A similar procedure was applied to MMIn, which is a reaction intermediate in the TMIn decomposition. The same model chemistry was used as in the TMIn case and the reduced mass was 13.2856. The harmonic and anharmonic terms in Eq. 3-31 for MMIn are 434.1 and 2.05 cm^{-1}, respectively. Hot bands of MMIn were reported previously from the overtone observation [Par02]. They are compared with current calculation results in Table 3-5. The calculated and observed results showed very good agreements even for higher transitions.

Table 3-5. Vibrational transitions of MMIn.

Transition	Experimental (cm^{-1})	Calculated (cm^{-1})
$1 \leftarrow 0$	430	430.0
$2 \leftarrow 1$	424	425.9
$3 \leftarrow 2$	419	421.8

The vibration energy of 430 cm^{-1} corresponds to 5 kJ/mol and the Boltzmann factor becomes e^{-1} at 344 °C. Therefore, the hot band transitions are expected to occur considerably in TMIn decomposition conditions, where gas temperature can be higher than 500 °C, and broader peaks are possibly to be observed due to the hot bands.

3.4.2 Basis Set Superposition Error

Basis set superposition error (BSSE) on energy calculations comes from the size limitation of the basis set in practice. In computational chemistry, true wave functions are approximately expanded with a finite number of basis functions and therefore available size of basis function for a specific atom is virtually changing during an association or fragmentation process. This concept is visualized with a dimer of helium (Figure 3-8).

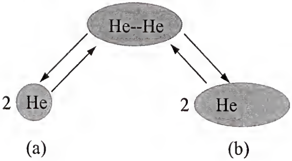

Figure 3-8. Size of the available basis set in (a) is different from that in (b).

The figure shows that size of the basis set that a helium atom feels is bigger in Case (b). Therefore, interaction energy calculated by a simple energy difference between one helium dimer and a set of two infinitely separated helium atoms contains inherent errors. BSSE can be mitigated using the counterpoise (CP) correction [Boy70]. The idea is exemplified for the adduct formation between TMGa and NH_3 in Figure 3-9. The two parts are deformed to the corresponding structures in the adduct and then the deformed parts are combined into the adduct. The interaction energy (ΔE) for the whole process is written by

$$\Delta E = E(AB, \alpha+\beta) - E(A', \alpha+\beta) - E(B', \alpha+\beta) + E(A', \alpha) - E(A, \alpha) + E(B', \beta) - E(B, \beta) \tag{3-32a}$$

Or

$$= E(AB, \alpha+\beta) - E(A, \alpha) - E(B, \beta) + E(A', \alpha) - E(A', \alpha+\beta) + E(B', \beta) - E(B', \alpha+\beta). \tag{3-32b}$$

The first line in Eq. 3-32b is the conceptual interaction energy and the second line is the CP correction given basis sets. BSSE comes from incompleteness of practical basis sets in calculations and therefore this error term becomes smaller as bigger basis sets are used for the calculations.

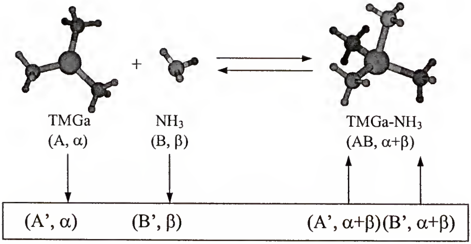

Figure 3-9. Adduct formation from TMGa and ammonia. The prime (') denotes that the fragment has the same structure as in the adduct (TMGa-NH_3) and Greek letters are used to designate size of basis functions.

3.4.3 Calculation of Thermodynamic Properties

With calculated energy states, e.g. Eq. 3-27, thermodynamic properties can be estimated using statistical mechanics [Cra02]. As an example, the Ga-C bond energies of TMGa were calculated. TMGa is the most popular gallium source for compound semiconductor material growth and has been assumed to decompose by sequential homolytic fission of the metal-carbon bond to yield methyl radicals. The homogeneous decomposition of TMGa was first studied by Jacko and Price [Jac63] using toluene as a carrier gas at low pressure. Experimental activation energy for the first bond dissociation of TMGa has been reported in the range 58 to 64 kcal/mol [Jac63, Mou91], while that for the second was 35.4 kcal/mol [Jac63]. Thermodynamically, however, the average bond energy for the Ga-C bond in TMGa was measured to be 57.7 kcal/mol [Lon58].

The bond energies were calculated for the range 300 to 800 °C, using *ab initio* methods, for three consecutive decomposition steps:

Setp 1: $Ga(CH_3)_3 \rightarrow GaCH_3 + CH_3$
Step 2: $Ga(CH_3)_2 \rightarrow GaCH_3 + CH_3$

Step 3: $GaCH_3 \rightarrow Ga + CH_3$

MP2 theory was used with two different basis sets. The G2 method that is an extrapolation procedure specific to *Gaussian* [Fri03] was also used for comparison. The averaged results for 300 ~ 800 °C are summarized in Table 3-6. For MP2 theory, BSSE was compensated with the CP method, while no correction was made for the extrapolation procedure, G2.

Table 3-6. Ga-C bond energies in TMGa decomposition (kcal/mol).

	Setp 1	Step 2	Step 3	Average
MP2/LanL2DZ	60.6	26.9	51.0	46.2
MP2/cc-pVDZ	70.4	33.5	60.3	54.7
G2	78.9	31.6	65.0	58.5
Experimental	58 – 64$^{(1)}$	35.4$^{(2)}$	-	57.7$^{(3)}$

(1) Jac63 and Mou91, (2) Jac63, and (3) Lon58.

The average Ga-C bond energy increases as the basis set was larger and the extrapolation procedure method (G2) produced a close value to the thermodynamically determined value. Calculated bond energies for the first step showed, however, noticeable difference compared with the experimental range of the value. As pointed out by McDaniel and Allendorf [Mcd00], decomposition reactions of metalorganic sources are easily susceptible to experimental conditions such as the reactor type. Therefore, it is important to set up experimental conditions that render an effective separation of the involved reactions.

CHAPTER 4
MODEL VALIDATION FOR HEAT AND MASS TRANSPORT

4.1 Heat Transport

4.1.1 Background

Since CVD reactors are commonly operated in the mass transport limited regime [Has84, Li98], the quality and uniformity of the deposited layers are strongly influenced by the gas phase dynamics. It is beneficial to establish a uniform flow field in the reactor to minimize the reactant switching time and unwanted impurity incorporation in the layers. Some of compound semiconductor materials are grown at very high temperature (~ 1000 ^{o}C) and a large thermal gradient normal to the substrate surface can produce recirculation flow patterns in the reactor, causing growth rate variations, delayed impurity incorporation, and graded heterojunctions [Jen89]. These issues were addressed in several modeling and experimental investigations [Fot90b, Gil82, Jen91, Pat89] with conventional CVD reactors (e.g. horizontal, vertical down flow, and rotating disk configurations). There exist, however, very little experimental data beyond growth rates [Saf97] to validate reactor models, though many modeling investigations have been performed to obtain a better insight of MOCVD processes.

In the following, the heat transfer part of the reactor model developed in Chapter 2 is validated with experimental data in the reactor and effects of thermal conditions on the gas phase dynamics are investigated. Axial temperature profiles along the centerline of the reactor were measured by gas phase Raman spectroscopy and used to validate the reactor model.

4.1.2 Validation of the Heat Transport Model

In the experiments, pure nitrogen was introduced to the reactor (Figure 2-2) and the heater temperature (T_{Heater}) was set at 500 °C. A single gas velocity was set for all three inlets, and temperature profiles were measured along the centerline of the reactor for two different nominal gas velocities, 2.5 and 3.5 cm/s. Gas temperatures were obtained from rotational Raman spectra of nitrogen using the procedure explained in Chapter 3. At steady state, the thermocouple-measured temperatures (T_{Bottom}) at the bottom of the reactor for 2.5 and 3.5 cm/s were 32 and 31 °C, respectively, due to radiation heat transfer from the heating unit.

Experimental data and simulation results are presented in Figure 4-1. The solid lines were obtained from the simulations using the reactor model developed in Chapter 2. There were several adjustable parameters in the heat transport part of the model. Most of the required physical properties (e.g. thermal conductivity and emissivity) are well reported, while thermal conductivities of the resistance block and the porous layers need to be determined to produce good matches between the experimental and simulation results. It is important to see they are within reasonable ranges while giving good reproduction of the experimental results. Two simulation results shown in Figure 4-1 were obtained with the same set of physical parameters except the gas velocity values. The current numerical model was also able to reproduce experimental temperature profiles when pure hydrogen was used as presented in Section 4.1.3. Therefore, the heat transport model was capable of describing the actual heat transport process in the reactor. In the next part, the characteristic of gas dynamics of the reactor is discussed in more detail.

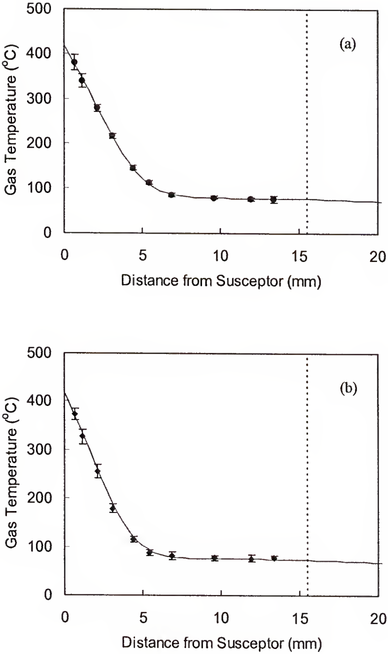

Figure 4-1. Axial temperature profiles for two inlet velocities: (a) 2.5 and (b) 3.5 cm/s. The heater was set at 500 °C and pure N_2 was used. The vertical dashed line designates the position of the inlet tip.

4.1.3 Gas Phase Dynamics

The gas dynamics of the inverted, stagnation flow CVD reactor was studied by both experiment and modeling. Axial centerline temperature profiles in the reactor were measured by analysis of the rotational Raman spectra from the common carrier gas, i.e. nitrogen or hydrogen, as a function of the inlet gas velocity. The heater temperature was set at 650 °C and a single value of gas velocity was set at the inlets. The gas velocities tested were 0.05, 1.5, and 3.0 cm/s at the inlets for both gas cases.

The results of the numerical calculations are shown in Figure 4-2 as solid and dashed lines and are compared with the measured temperature values. The calculated results are in good agreement with the experimental results. These results clearly show that the use of an N_2 carrier gas produces a steeper temperature gradient normal to the susceptor surface than the use of a H_2 carrier gas. The same behavior was obtained by other investigators using both horizontal [Fot90a, Gil82, Jen91, Kop84, Mof86, Sto86, Van86,] and vertical down flow [Mon86, Mon88] reactor geometries. The result is easily understood by considering the nearly eight times higher thermal conductivity of H_2, compared with that of N_2.

It is interesting that the extrapolated surface temperature at the susceptor (~530 °C for N_2 and ~430 °C for H_2) is considerably lower than the set temperature (650°C). This result suggests that a significant thermal contact resistance exists between the heating block and the inside wall of the quartz envelope, though this resistance was considerably reduced with change of the heating unit design later.

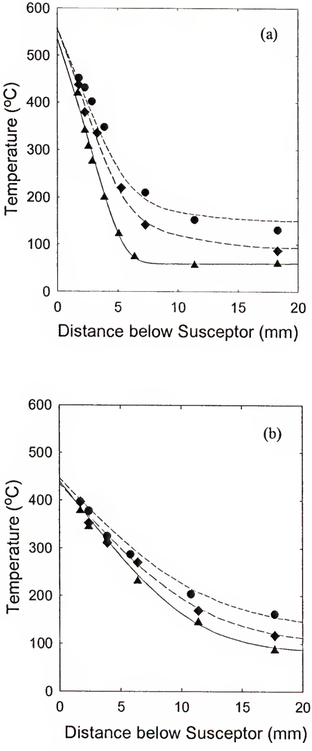

Figure 4-2. Temperature profiles along the centerline of the reactor: (a) nitrogen and (b) hydrogen carrier gases with varying gas velocities: ●, $v_0 = 0.09$ cm/s; ◆, $v_0 = 1.5$ cm/s; and ▲, $v_0 = 3.0$ cm/s.

Measuring temperature at the susceptor surface is an extremely difficult task because measuring devices, e.g. thermocouple, disturbs the already developed temperature profile. By using Raman spectroscopy and the reactor model, it was possible to estimate the temperature at the solid surface without affecting it.

Measured temperature profiles with the N_2 carrier gas show that the gas temperature approached a constant value sufficiently away from the susceptor surface (Figures 4-1 and 4-2a). For example, the gas temperature became nearly constant from the point about 6 mm away from the susceptor. Presumably, this was caused by radiation heating of the stainless steel and packing material within the inlets, which subsequently pre-heated the inlet gas. Therefore, including radiation heat transfer in the reactor model was found to be necessary to match experimental gas temperature. The importance of including radiation in CVD reactor models is supported by recent numerical studies [Dur95, Kad95] of a horizontal CVD reactor that indicated the temperature of the upper wall facing the heated surface varied by 40-70 °C depending on the wall material and the value of the susceptor emissivity. A numerical study [Chi91] of a vertical upflow reactor with a design similar to the current one further supports the importance of radiation heat transport.

The effect of changing the inlet gas velocity on the axial temperature profile is also shown in Figure 4-2. As expected, the decreased residence time in the rector with increased gas velocity resulted in a steeper temperature gradient. In case of the N_2 carrier gas, most of the temperature change occurred less than 6.0 mm from the susceptor surface at an inlet velocity of 3.0 cm/s.

Several factors can cause the actual gas dynamics in the reactor to deviate from the calculated results. For example, in real reactors purely axisymmetric boundary conditions cannot be achieved (e.g., alignment of the center inlet tube, temperature variations across the susceptor surface). Sharp corners and sudden expansions (or contractions) in the flow cross-sectional area can also produce laminar vortices. The two-dimensional analysis performed in this study, however, provides insight into the gas dynamics in the reactor, and it successfully represents the experimentally measured axial temperature profile using reasonable boundary conditions.

With the validated reactor model, the gas dynamics in the reactor was closely explored. Figures 4-3 and 4-4 show the calculated flow profiles and isotherms in the reactor as a function of the inlet flow velocity using N_2 and H_2 carrier gases, respectively. At the very low inlet flow velocity (0.09 cm/s) the isotherms spread toward the gas inlet for both N_2 (Figure 4-3b) and H_2 (Figure 4-4b), indicating a relatively small temperature gradient normal to the susceptor surface. Recirculation flow patterns are produced at this velocity due to the transverse thermal gradient. A more complex recirculation was observed in the N_2 carrier gas (Figure 4-3a) compared to that in the H_2 carrier gas (Figure 4-4a), because the sidewall heating is greater when using N_2. As the inlet flow velocity increases to 3.0 cm/s, the isotherms contract toward the susceptor (Figures 4-3d and 4-4d), and the fluid flow becomes simpler as forced convection dominates (Figures 4-3c and 4-4c). The isotherms are more confined to the vicinity of the susceptor and parallel to the susceptor at the highest velocity studied with the use of a N_2 carrier gas (Figure 4-3d).

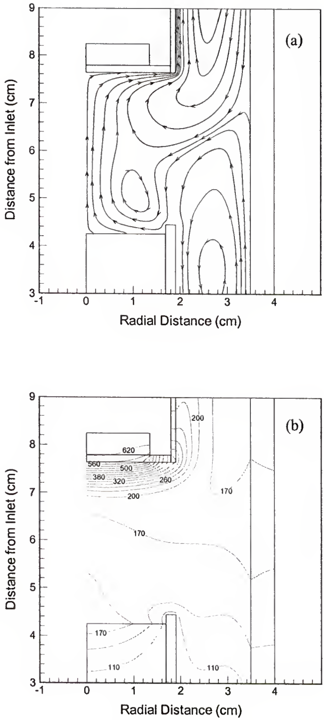

Figure 4-3. Calculated streamlines and isotherms in the reactor for N_2 carrier gas for two gas velocities: (a) streamlines and (b) isotherms for the gas velocity of 0.09 cm/s; and (c) streamlines and (d) isotherms for the gas velocity of 3.0 cm/s. The temperature spacing between adjacent isotherms is 30 °C.

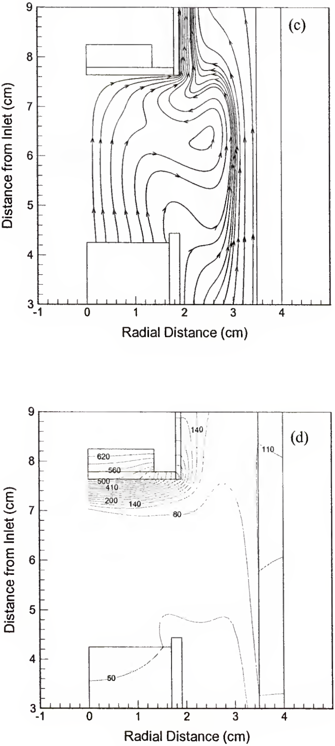

Figure 4-3. Continued.

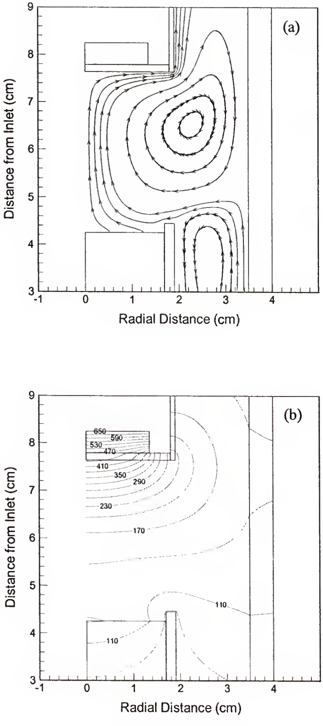

Figure 4-4. Calculated streamlines and isotherms in the reactor for H_2 carrier gas for two gas velocities: (a) streamlines and (b) isotherms for the gas velocity of 0.09 cm/s; and (c) streamlines and (d) isotherms for the gas velocity of 3.0 cm/s. The temperature spacing between adjacent isotherms is 30 °C.

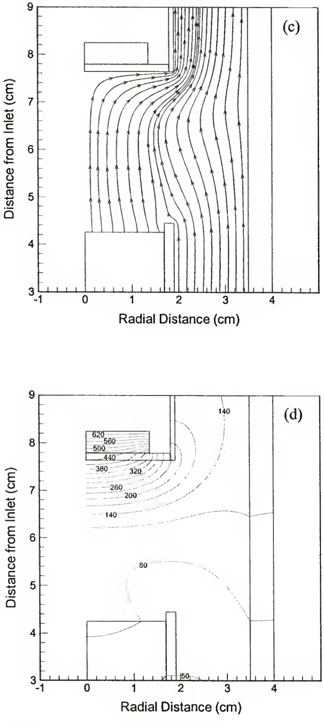

Figure 4-4. Continued.

The isotherms developed in the reactor with the use of the more conductive H_2 carrier gas, however, were not confined to the vicinity of the susceptor even at the highest velocity studied (3.0 cm/s). The recirculation flow patterns were not strong in the entire operating range used in this study except for the case with very small gas velocity (0.09 cm/s), for both N_2 and H_2 carrier gases. The numerical results indicate that the H_2 carrier gas provides more stable flow profiles than the N_2 carrier gas at the same matched inlet velocities. The higher thermal conductivity of H_2 reduces the transverse thermal gradients, and therefore natural convection is weaker. The upflow reactor geometry used in this study and the relatively low susceptor temperature appear to be responsible for the prediction of only weak recirculation flow patterns. To support this conclusion, simulations were performed with the same reactor geometry but oriented in the direction of the gravity vector. The results for H_2 are shown in Figure 4-5. At the inlet velocity of 3.0 cm/s, a strong flow recirculation pattern exists (Figure 4-5a) and the isotherms spread out towards the gas inlet (Figure 4-5b). The flow recirculation patterns became more complex and stronger for the N_2 carrier gas. These results clearly indicate the effect of the inverted design on suppressing flow recirculation.

From the viewpoint of the gas dynamics, the use of a N_2 carrier gas at high velocity seems to be preferred for the growth of epitaxial layers. Isotherms confined and parallel to the substrate surface help prevent parasitic gas phase reactions, and uniform flow fields allow more uniform mass transfer. The work of Sacilotti et al. [Sac83] showed that more uniform epitaxial layers were deposited in the deposition of InP from $In(CH_3)_3$ and PH_3 in a horizontal reactor when N_2 was used as the carrier gas as compared to H_2.

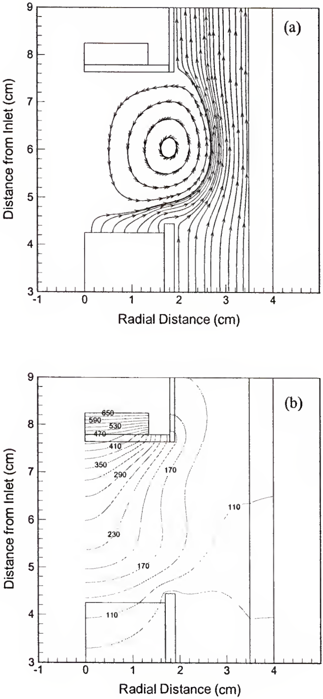

Figure 4-5. Calculated (a) streamlines and (b) isotherms in the reactor with H_2 carrier gas when the gravity is inverted. The gas velocity at the inlets was 3.0 cm/s.

Other problems such as the purity of the N_2 carrier gas and the positive role of H_2 in the deposition chemistry (e.g., reducing carbon incorporation by reaction with methyl radicals), however, must be considered when selecting the carrier gas. From the perspective of gas dynamics in a vertical reactor, the upflow reactor configuration is preferred, since it can more easily provide forced convection dominated flow fields due to the stabilizing density gradient developed in the reactor. It also provides a more favorable arrangement for particle rejection. Substrate handling issues related to automation, however, need to be carefully addressed for successful operation.

4.1.4 Summary

The heat transport part of the reactor model developed in Chapter 2 was validated with experimental temperature profiles measured by the pure rotational Raman scattering from diatomic carrier gas molecules. Using the model, gas dynamics of an inverted, stagnation flow CVD reactor was investigated. It was found that a larger temperature gradient normal to the susceptor surface was obtained with a higher gas flow velocity and the use of N_2 carrier gas. Detailed treatment of heat transport was found to be critical in obtaining realistic predictions. The stabilizing density gradient provided by the upflow geometry was a positive characteristic of this reactor.

4.2 Mass Transport

4.2.1 Background

In case of a simple flow cell experiment, which is usually used with absorption spectroscopy to investigate chemical reactions of metalorganic precursors, experimental data are gathered as a function of time at a constant temperature. Analysis of data in this case is quite simple because non-homogeneity of temperature or concentration distribution is neglected, and gives kinetic information without any accompanied difficulty. Most of the previous reaction kinetics studies on MOCVD precursors have been conducted in this way. One major shortcoming of this approach is that this description of phenomena in the reactor is oversimplified. In contrast, Raman spectroscopy is capable of simultaneously giving thermal and species information within a flow reactor with good spatial resolution. Therefore, it is possible to obtain detailed kinetic information of the chemical reactions under inhomogeneous conditions using a conventional Raman system. Most of metalorganic precursors, e.g. TMIn, TMGa, and TMAl, are detectable with Raman spectroscopy. In the current work, an up flow stagnation flow reactor within which temperature and concentration is not homogeneous was used and data were recorded at various spatial positions within the reactor. It should be, however, mentioned that reaction conditions in the reactor were too complicated to do a simple analysis as with a flow cell. Therefore, a simulation tool is required to extract more information about reactions after concentration and temperature profiles are obtained from experiments. Analysis of experimental data with a proper model can give information about transport properties as well as reaction kinetics. To do this kind of job successfully, the model should be validated before its use.

In this section, the mass transport model was verified using a tracer, methane. There are no adjustable parameters in the model if experiments are performed at a constant temperature, and therefore validation of the mass transport model is a difficult job. Methane was chosen because it has a large Raman cross-section and properties of methane are well known. In addition, it is a stable, simple species and its properties can be well estimated using the Lennard-Jones potential parameters (Section 2.3.4). Although most of its physical properties are well known, its Raman cross-section is not uniquely reported [Sch79]: 6.8, 8.7, and 9.2 relative to the Q-branch intensity of nitrogen at 2331 cm^{-1} for the symmetric C-H vibration at 2917 cm^{-1}. Raman cross-section is one of the most crucial parameter in quantitatively analyzing mass transport-related phenomena. Before validating the mass transport part of the model, the Raman cross-section of methane was measured using a mixture of methane and nitrogen with known concentration. A mixture was purchased from the BOC Gases and its certified concentration was 10 ± 0.5 %. Six sets of methane and nitrogen spectra were taken with the 488 nm line of an argon ion laser at 23 °C and the relative Raman cross-section of methane was calculated using Eqs. 3-24 and 3-25: the relative cross-section was determined to be 8.57 with standard deviation of 0.24. Using this relative Raman cross-section, the mass transport model of the reactor was validated.

4.2.2 First Inlet Configuration

Mass dispersion experiments were conducted using methane as the tracer at room temperature. The first inlet design used is depicted in Figure 4-6. In this inlet configuration, the annulus inlet was first filled with glass beads the diameter of which was 3 mm and then a stainless steel screen was put. The distance between the susceptor surface and the tip of the center/annulus inlet defined a separation distance. Aspect ratio was defined as the ratio of the separation distance to the inner diameter (D_e) of the annulus inlet.

The 10 % methane in nitrogen was introduced through the annulus inlet (the second inlet from the center), and nitrogen through the center and sweep inlets. A single gas velocity was set at all three inlets. The experiments were performed for two aspect ratios (0.5 and 1.0) with the single gas velocity of 1.5 cm/s. Raman spectra were taken along the centerline of the reactor at 2331 and 2917 cm^{-1} for nitrogen and methane, respectively. Mole fraction of methane was calculated from each pair of peaks using Eqs. 3-24 and 3-25. Simulations were also conducted with the experimental conditions to see if the actual situations were adequately incorporated into the model.

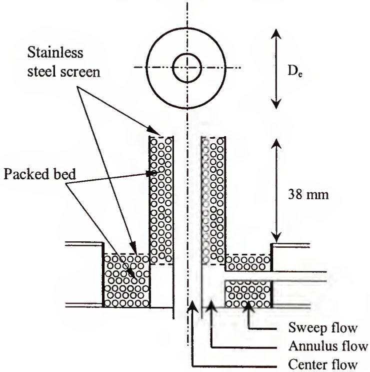

Figure 4-6. The first inlet configuration used in the model validation.

The experimental and simulation results are presented in Figure 4-7. The error bars in the figure represent the 99.7 % confidence interval for each point. The axial distance from the susceptor surface is in the x-axis and the vertical dashed line denotes the position of the inlet tip. The experimental concentration profiles show that methane concentration was low near the inlets and increased along the centerline. Near the susceptor, the concentration became saturated for aspect ratio = 0.5, while slightly dropped for aspect ratio = 1.0.

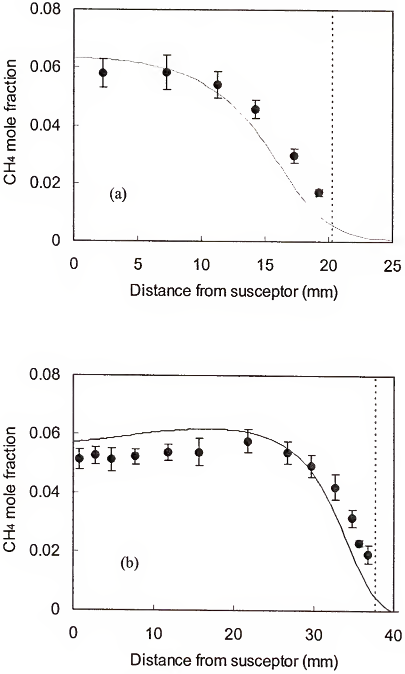

Figure 4-7. Axial concentration profiles along the centerline of the reactor. Aspect ratio = (a) 0.5 and (b) 1.0. The gas velocity at the inlets was 1.5 cm/s for both cases.

Methane diffuses toward the centerline as gases flow toward the susceptor and its concentration reaches at a maximum at some distance from the inlet. If further distance is available for the flow to travel, then methane concentration at the centerline becomes higher than that of the neighboring region because pure nitrogen is supplied through the sweep inlet. Therefore, methane diffuses out radially and its concentration at the centerline starts to drop from the maximum.

Simulation results showed reasonable trends of the concentration profiles. There are, however, two distinct features in Figure 4-7: the simulations underestimated experimental results near the inlet and overestimated near the susceptor. Lateral transport of methane toward the centerline seemed to be expedited near the inlet by some means, e.g. disturbances to the flow caused by the presence of the stainless steel screen, glass beads, and inlet wall. As a result, methane concentration reaches its maximum prematurely and starts to diffuse out radially and the concentration becomes lower than expected by the simulations (Figure 4-7).

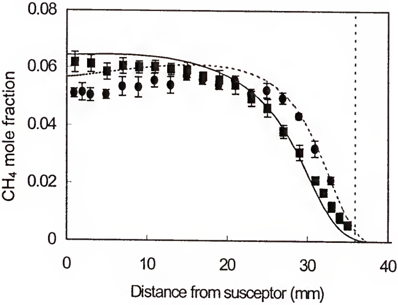

Figure 4-8. Axial concentration profiles along the centerline of the reactor for the gas velocities of (●) 1.5 cm/s and (■) 2.5 cm/s with aspect ratio = 1.0.

Non-reactive mass transport at a constant temperature leaves no adjustable physical parameters except modification of the finite element mesh. To increase the inward transport of methane near the inlet, the annulus inlet wall was trimmed in the finite element mesh. The calculation results for aspect ratio = 1.0 are presented in Figure 4-8. As intended, methane concentration near the inlet was increased for both velocity cases, while unsatisfactory prediction still remained near the susceptor surface. Consequently, modification of finite element mesh was not a good remedy to obtain better reproduction of the experimental data by simulation. It was considered that the actual phenomena were too complex in the experimental setup to be simply modeled.

Because the methane stream was delivered to the annulus channel through a small diameter tube (3 mm) at one side of it, glass beads and a stainless screen were put in the annulus inlet to prevent the methane flow from channeling. The screen, however, left only about 30 % of the cross-sectional area of the annulus for flow, and further the diameter of the glass bead was not small compared with the size of the annulus. This combination of the glass beads and stainless steel screen could cause complex flow patterns near the inlet tip and enhance mixing between flows from the two inlet channels, i.e. the center and annulus. This situation is not easy to be simply modeled and therefore actual flow pattern at the inlet should be simplified to represent it by conceivable boundary conditions. For the disturbances caused by the packing materials to diminish, the glass bead bed was lowered by 13 mm in the annulus, leaving 25 mm height of the glass bead bed. With this new inlet geometry, experiments were repeated for aspect ratio = 0.5 and the results are presented in Figure 4-9.

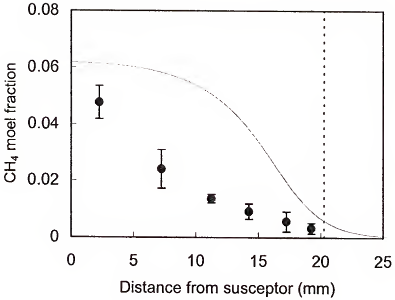

Figure 4-9. Concentration profile with partially removed glass beads. Aspect ratio was 0.5 and gas velocity at the inlets was 1.5 cm/s.

The difference between experimental and simulation results, however, became even larger and implied that channeling of the methane stream though the glass bead bed or other complex phenomena occurred. This result indicated that the minimum height of the glass bead bed should be about 40 mm to stabilize flows in the reactor and therefore a conceivable way to stabilize the inlet boundary condition was to allow more space for the flow to fully develop.

4.2.3 New Inlet Configuration and Flow Instability

Lack of fit observed in the previous section was considered to come from improper modeling of the boundary conditions at the inlets. Based on the results in Section 4.2.2, a new inlet configuration was designed (Figure 4-10) to make the boundary conditions simpler than those in the previous methane dispersion experiments.

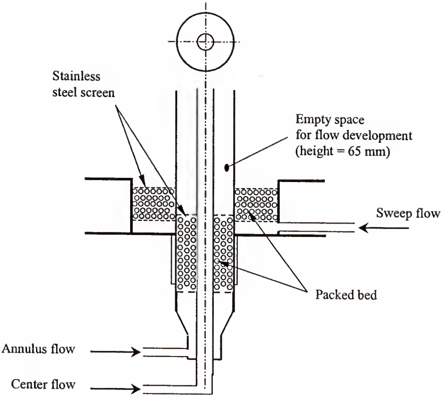

Figure 4-10. Modified inlet configuration.

In the new configuration, there was a 65 mm height of empty space in the annulus after a 40 mm-high glass bead layer for the flow to fully develop. The length of the empty space was determined based on the entrance length (L_e) calculated using a simple correlation, $L_e = 0.035\ D\ Re$, where D is an equivalent diameter of the annulus and Re is the Reynolds number. For the new inlet configuration, estimated entrance length for air was about 2.5 cm for the velocity of 3.0 cm/s and was about 5.0 cm for 6.0 cm/s. The entrance length correlation is, however, obtained when the incoming flow has a totally parallel velocity profile. That assumption was not completely met under the current conditions and therefore slightly longer empty space was put in the new inlet configuration. The height of the empty space was 65 mm at maximum due to physical limitation of the experimental apparatus.

Methane dispersion experiments were conducted with the modified inlet configuration for three different gas velocities: 1.5, 3.0, and 4.5 cm/s at 23 °C. For each velocity case, a single gas velocity was set at all three inlets. 10 % methane in nitrogen was supplied through the annulus inlet, while pure nitrogen was through the center and sweep. Intensities of methane and nitrogen vibrations at 2917 and 2331 cm^{-1}, respectively, were recorded along the centerline of the reactor for each gas velocity case. Methane mole fraction was calculated with the previously determined relative Raman cross-section of methane, 8.57.

Measured concentration profiles along with simulation results are shown in Figure 4-11. Contrary to the expectation, the simulations did not reproduce experimental results very well except the 4.5 cm/s. Maximum concentration observed in the experiments was the highest in 4.5 cm/s and the lowest in 1.5 cm/s. If stable flow field were established in the reactor for all three cases, the order in concentration should be reversed. It was also noticed that poor reproduction of experimental data was significant at the low velocities, while a fairly good reproduction was made at 4.5 cm/s. Therefore, it was considered that the flow fields in the reactor were not simple laminar at low gas velocities and became laminar as gas velocity increases.

Increased gas velocity gives two consequences: (1) improved flow distribution due to an increased pressure drop across the glass bead bed and (2) tolerance of a given flow field with respect to disturbances.

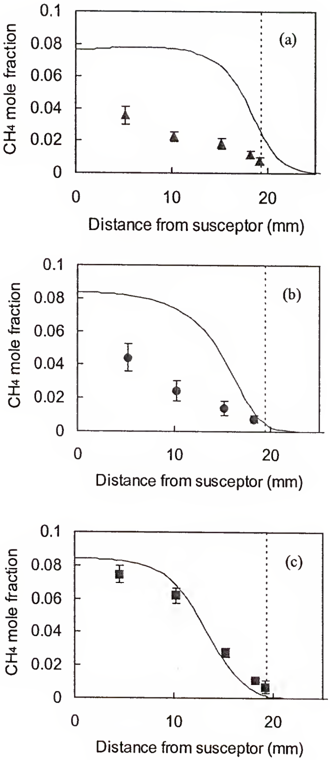

Figure 4-11. Axial concentration profiles of CH_4 with the modified inlet configuration at (a) 1.5, (b) 3.0, and (c) 4.5 cm/s. The initial CH_4 concentration was 10 %.

The first proposition was not acceptable because a more reasonable profile was measured with the same height of glass bead bed in the old inlet configuration (Figure 4-7). The second needs to be considered further in the following.

To better understand the nature of this new regime, axial methane concentrations were measured at two radial positions (r = 0 and 10 mm), introducing 10 % methane in nitrogen through the annulus inlet and pure N_2 through the center and sweep inlets with a matched gas velocity of 1.5 cm/s. It was anticipated that these experimental conditions pushed the flows into the new regime. The experimental results are represented in Figure 4-12.

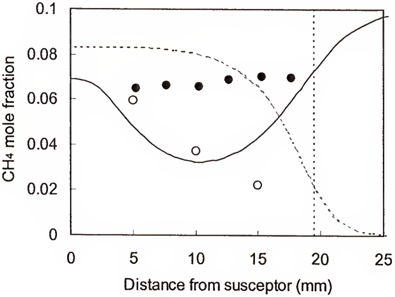

Figure 4-12. Axial concentration profiles of CH_4 at r = 0 mm (O, ---) and r = 10 mm (●, —) at 24 °C. The initial concentration was 10 % and velocity was set at 1.5 cm/s. The vertical dashed line denoted the axial position of the inlet.

The concentrations denoted by open circles in Figure 4-12 were axially measured along the centerline (at r = 0 mm) and those denoted by filled circles were at r = 10 mm which was about the middle of the annulus region. The calculation results are presented as the broken (r = 0 mm) and solid (r = 10 mm) lines in Figure 4-12. The considerable differences between the experimental and calculated concentrations apparently denoted that the methane transport toward the centerline of the reactor was efficiently restrained and methane apparently remains around the initial radial position while flowing axially. As the calculations with the validated 2-D mass transport model predicted (Figure 4-12), the flow strength in this case did not seem strong enough to suppress observable mass transport (dispersion) as efficiently as shown in the experimental observations. Furthermore, if any flow instability occurs only just above the center and annulus region, the concentrations measured along the centerline will be higher than the calculations with the model, due to effective gas mixing in the center and annulus flow region. For the same reasons, mixing of methane and nitrogen would be enhanced even if the flow were time-dependent. Therefore, it was considered that the flow in the reactor was no longer two-dimensional and fresh N_2 was supplied from the sweep (pure N_2) flow. Onset of a three-dimensional flow from a stable axisymmetric flow due to thermally driven buoyancy was predicted in a downward stagnation-flow reactor [San00]. It was suggested in that study that the three-dimensional flow change temperature profiles significantly, i.e. three-dimensional temperature distribution. In the current case, a large solutal density gradient could trigger flow instability and changed flow regimes. Using the validated 2-D mass transport model, streamlines and contour lines in the reactor were calculated for 10 % CH_4/N_2 with and without gravity at the gas velocity of 1.5 cm/s to see the effects of buoyancy on mass and momentum transport.

As shown in Figure 4-13, there is a strong driving force, due to buoyancy, for the sweep flow to be pushed toward the centerline of the reactor when gravity is turned on.

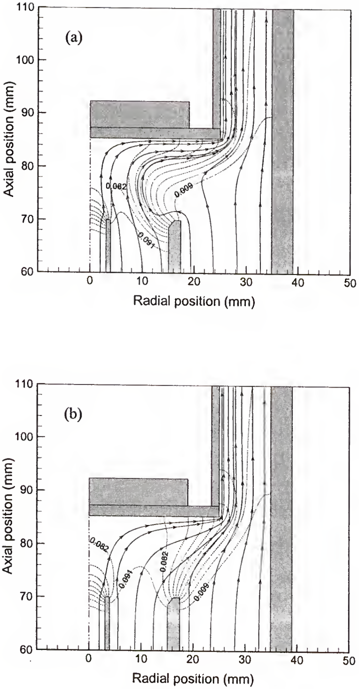

Figure 4-13. Streamlines and concentration contours in the reactor when 10 % CH_4/N_2 is introduced through the annulus inlet with (a) and without (b) gravity. The gas velocity is 1.5 cm/s for both cases.

If the driving force is well balanced azimuthally, the flow will remain two-dimensional, i.e. axisymmetric. That is expected when the 2-D mass transport model is used. The experimental observations, however, suggested that the balance is susceptible to disturbances when the driving force is large enough. Therefore, it was considered that a 3-D flow was developed in the reactor with loss of the balance in the driving force caused by solutal density gradients and then a stream of fresh nitrogen was supplied from the sweep flow into the center/annulus region.

To further study solutal effects on the flow field in the reactor, inlet concentration was lowered and axial concentration profile along the centerline of the reactor was measured at room temperature. Three concentrations (1.91, 5.0, and 7.5 % CH_4/N_2) were tested for a matched inlet velocity of 2.5 cm/s.

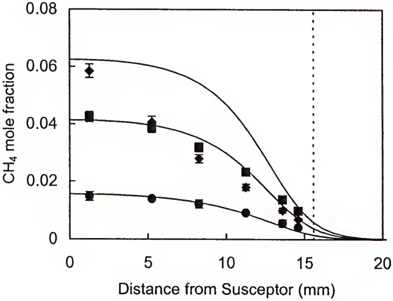

Figure 4-14. Axial concentration profiles of CH_4 for three different inlet concentrations at 23.3 °C: (●) 1.91 %, (■) 5.0 %, and (◆) 7.5 %. Gas velocities are set at 2.5 cm/s for all cases.

The results presented in Figure 4-14 clearly show that the reactor model reproduced the experimental profile at the 1.91 % case, but not the 7.5 % case. It was considered that this discrepancy between the experimental observations and calculations in the 7.5 % case was not produced by the presence of stable recirculation flow patterns in the reactor. For example, in the 5.0 % case, the model predicted recirculation patterns (Figure 4-15) and still reproduced the experimental concentration profile fairly well (Figure 4-14). This observation suggested that the flow regimes are considerably changed for the 7.5 % case and the mass transport model used here is not capable of describing flows in the new regime.

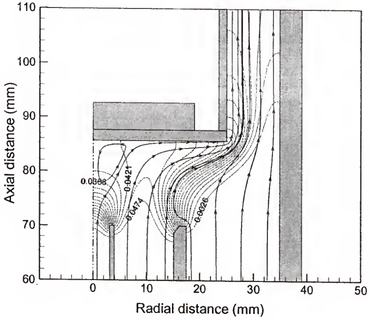

Figure 4-15. Streamlines and concentration contours in the reactor when 5 % CH_4/N_2 is introduced through the annulus inlet, while pure N_2 is through the center and sweep inlets. The gas velocity is 2.5 cm/s.

The experimental results presented thus far in this section were obtained with the modified inlet configuration depicted in Figure 4-10. One prominent feature of the modified configuration was the 65 mm space for flows to develop in. The empty space, however, should promote the occurrence of the new flow regime by increasing the characteristic length if the distance traveled by the gas is an important length scale of the transition process. To test this hypothesis, the annulus inlet was further filled with glass beads to leave only 6 mm height of empty space and the other inlets remained unchanged. With this modification, two concentration cases, 10 and 14.5 %, were examined with a single gas velocity (2.5 cm/s). The CH_4 concentration was probed along the centerline of the reactor and presented in Figure 4-16 along with simulation results. With the reduced length of the free space in the annulus channel, the model reproduced experimental observations reasonably well even for the 10 % case. At the same gas velocity (2.5 cm/s), the 7.5 % case in Figure 4-14 showed that the model was not able to reproduce experimental data.

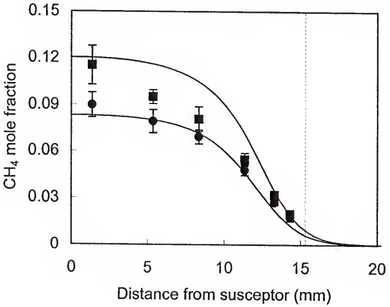

Figure 4-16. Axial concentration profiles of CH_4 with a reduced gas-travel length at 23 °C: (●) 10 % and (■) 14.5 %. Gas velocity was set at 2.5 cm/s.

This implies that the empty space in the annulus region, through which the CH_4/N_2 mixture travels, affected the onset of the flow instability and that the distance travel by the gas mixture was an important characteristic length for the onset of the new flow regime. An even higher concentration (14.5 %) caused experimental measurements to significantly deviate from calculated concentration profile.

The influence of the annulus packing on the driving force to the new flow regime was investigated by re-calculating the Figure 4-13a case with a fully packed annulus. It is noticeable from the results (Figure 4-17) that methane concentration is more homogenized, i.e. the area under 0.082 gets larger, by filling the annulus channel. At the same time, the degree of pushing by the sweep flow becomes weaker and therefore flows in the reactor tend to be stabilized.

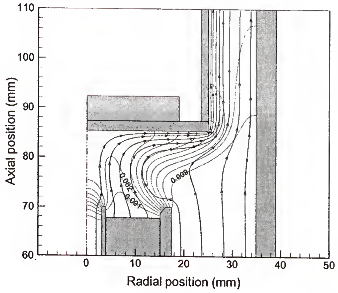

Figure 4-17. Effects of filling the annulus channel on streamlines and concentration contours. The initial concentration is 10 %. The reference state is shown in Figure 4-13a.

From the above observations, it was considered that onset of the new flow regime was influenced by the gas velocity (Figure 4-11), solutal density difference (Figure 4-14), and characteristic distance traveled by the gas (Figures 4-13a and 4-17). The dimensionless group charactering the instability phenomena should consist of these terms. Gr/Re^2 represents relative strength of the buoyancy forces to inertia forces and contains those characterizing terms:

$$\frac{Gr}{Re^2} = \frac{gL\Delta\rho}{V^2\rho} \approx \frac{gL}{V^2}\left(1 - \frac{M_{CH_4}}{M_{N_2}}\right)x_{CH_4} \tag{4-1}$$

where the characteristic gravity, length scale, velocity scale, density, molecular weight, and mole fraction are represented by L, g, V, ρ, M, and x, respectively. The second part of the equation includes the assumption of an ideal gas. The effects of the gas velocity (V), concentration (x), and gas-traveled distance (L) on the instability are explained with this dimensionless group. The values of the dimensionless group are, respectively, 14 and 21 for the 10 and 14.5 % CH_4 cases in Figure 4-16. It is, however, considered that the relative strength of the buoyancy forces to inertia forces has different dependence on the characterizing terms, depending on the reactor geometry and specific boundary conditions as reported for the thermal buoyancy case [Eva87, Fot90b]. In addition, it is noticed that the molecular weight difference between gas components can be a major factor to promote natural convection in MOCVD reactors.

4.2.4 Mass Transport Characteristics in the Reactor

A series of room temperature, steady state experiments were performed to better understand the mass transport characteristic in the reactor. In these experiments, a CH_4/N_2 mixture was introduced through the annulus inlet, while nitrogen was introduced through the center and sweep inlet channels. Steady state methane concentration profiles were measured along the centerline of the reactor using *in situ* Raman spectroscopy. Three values of the inlet gas velocity were studied (2.5, 3.5, and 4.5 cm/s), while maintaining a single velocity was set for all three inlets. The methane concentration at the annulus was also varied (1.91, 1.36, and 1.06 % for the 2.5, 3.5, and 4.5 cm/s inlet velocity conditions, respectively). Measured concentration profiles are presented in Figure 4-18 along with simulation results depicted in solid lines, where the previously determined relative Raman cross-section of 8.57 was used to analyze scattered Raman signals.

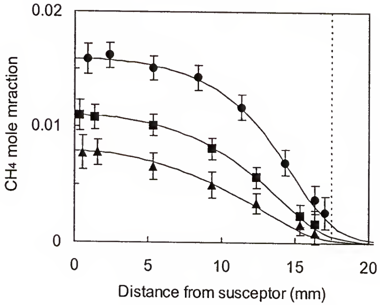

Figure 4-18. Methane concentration profiles at 24 °C along the centerline for three inlet velocity values: 2.5 (●), 3.5 (■), and 4.5 (▲) cm/s. The inlet methane concentrations are 1.91, 1.36, and 1.06 % for 2.5, 3.5, and 4.5 cm/s, respectively. The vertical dashed line denotes the axial inlet position.

The mass transport model was clearly able to reproduce experimental results without any adjustable parameters, though the experimental data in the figure showed a systematic positive deviation near the inlet position becomes larger at higher gas velocities. It is likely that the finite thickness of the inlet tubes disrupted the streamlines and promoted transverse mixing.

The validated model was then used to calculate concentration profiles in the reactor for various operating conditions to select interesting experimental conditions. As an example, Figure 4-19 shows calculated radial concentration profiles at three axial positions (1, 8, and 14 mm below the susceptor) at the gas velocity of 2.5 cm/s at all inlets. In this calculation, a 1.91 % CH_4/N_2 mixture was introduced at the annulus inlet, while pure nitrogen was delivered at both the center and sweep inlets.

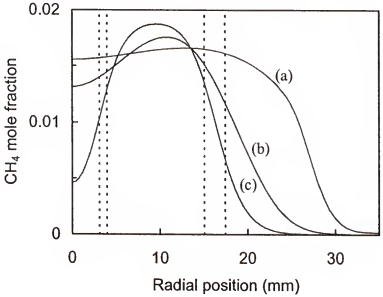

Figure 4-19. Radial CH_4 concentration profiles at different axial positions: z = (a) 1, (b) 8, and (c) 14 mm from the susceptor. The regions between vertical dashed lines represent the inlet wall positions.

The methane confined to the annulus at the inlet position then disperses towards both the center and the wall. The simulated radial concentration profiles seem reasonable when the flow characteristics of a stagnation-point-flow reactor and diffusive mass transport are taken into account. The figure reveals that the CH_4 probe gas is effectively isolated from the reactor wall at r = 35 mm. Such species confinement to the gas phase is often desired to avoid undesirable complexities caused by reactions at walls, for example, in the study of gas phase decomposition of metalorganic precursors. The wide range of reported values of the activation energy for TMAl pyrolysis (9 [Suz86] to 38 kcal/mol [Suz85]) are likely related to complications from wall reactions.

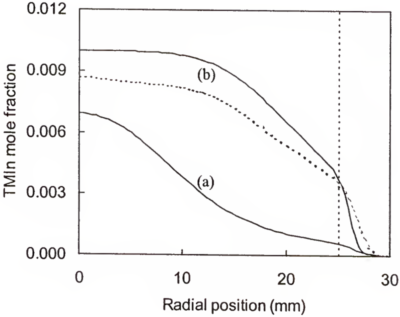

Figure 4-20. Calculated radial concentration profiles of TMIn for aspect ratio of (a) 1.0 and (b) 0.5. The dashed curve represents the susceptor rotation case. The vertical dashed line denotes the radius of susceptor.

In addition to adjusting the inlet velocity and gas composition, the position of the inlet relative to the susceptor is a common design variable. Figure 4-20 shows the purely calculated radial concentration profile of TMIn at aspect ratios 1 and 0.5 for 3.0 cm/s matched inlet velocities (the heater temperature was 900 °C, but no reactions were assumed). The aspect ratio was defined as the ratio of the separation distance between the substrate and the inlet to the inlet diameter. In this calculation, a 1.0 % TMIn in N_2 mixture was introduced to the reactor at the combined center-annulus inlet.

It is desirable that the radial concentration profiles of reactants near the substrate be uniform to deposit good quality films. As shown in Figure 4-20, the radial concentration profiles near the substrate depend significantly on the value of the aspect ratio. For a given velocity, a smaller aspect ratio, i.e. short distance between the susceptor and the inlet tip, gives less residence time and thus less radial transport and better uniformity at the substrate. The dashed concentration profile in this figure was calculated with rotation of the substrate at 60 rpm. As expected, rotating the substrate helps establish a flatter concentration profile near the substrate.

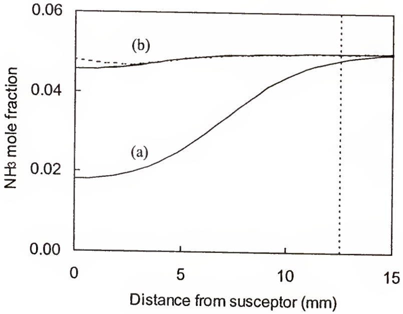

Figure 4-21. Calculated centerline concentration profiles of NH_3 for aspect ration of (a) 1.0 and (b) 0.5. The gas velocities were set at 3.0 cm/s and the NH_3 concentration was 5.0 % at the center inlet. The dashed curve represents the susceptor rotation case (60 rpm).

In applications of the reactor to measuring transport and gas phase kinetics, the optimal conditions to estimate mass diffusivity are different from those used to study homogenous reactions. If the reactor is being used to investigate pure mass transport behavior of chemical species and extract their transport properties (e.g., gas diffusivity), it is better to establish an axial concentration profile showing large gradients (see Figure 4-21a). On the other hand, to study reactions and estimate reaction rate constants from the measured profiles, it is better to have a centerline concentration that shows little variation (see Figure 4-21b), since observed variations in centerline concentration are then primarily determined by the extents of reactions.

4.2.5 Conclusions

The mass transport part of the reactor model developed in Chapter 2 was validated with experimental data. Inlet configuration of the reactor was modified during this validation process. Mass transport characteristic of the reactor was studied using the validated model. It was shown that the validated model could be used to customize experimental or operation conditions for specific objectives. In addition, flow instability caused by solutal density gradients was observed. Onset of instability was characterized by solutal density difference, gas velocity, and distance traveled by the gas.

CHAPTER 5
PARAMETER ESTIMATION PROCEDURE

5.1 Background

Most simulation problems dealing with physical phenomena are solved with *a priori* known parameters and boundary or initial conditions so as to give distributions of state variables, e.g. temperature, concentration, and velocity components. As a typical example, suppose that a temperature distribution within a specified geometry is to be solved. In this case, it is assumed that the thermal conductivity, density, heat capacity, and other physical properties are known. Solution procedures for this kind of problems (direct problems) are quite straightforward. Conversely, suppose that a set of measured temperatures within the domain is experimentally obtained and one or more physical parameters that govern the temperature distribution are unknown at the moment. Given a model the unknown parameter(s) are to be determined utilizing experimental measurements. This type of problems is called the parameter estimation problem (or an inverse problem). In practice, a numerical model describing a phenomenon is composed of a set of partial differential equations containing several physical parameters. In addition to the established model, a set of experimental data to be compared with estimates by the model complete a parameter estimation problem. This is the description of a distributed parameter estimation problem [Van78]. Distributed parameter estimation problems are widely used in determination of physical parameters such as heat conductivity, heat transfer coefficient, viscosity, reaction kinetic constants, and so on

[God78, Kub77]. Among parameter estimation studies, the non-linear kinetic parameter estimation has been one of most active subjects [Par01, Par98, Wan01].

In this chapter, a parameter estimation procedure is established, which consists of *in situ* experimental data collection, a validated reactor model, and an optimization procedure. The first and second components are discussed in previous chapters and the last component is developed here.

5.2 Establishment of Parameter Estimation Procedure

5.2.1 Fundamental Formulation

Solution of a parameter estimation problem (so called "inverse problem") is based on the method of maximum likelihood [Dra81]. To extract physical parameters from the experimental observations, e.g. Raman scattering intensities and temperatures, an optimization scheme is required as well as a validated reactor model. The optimization (or solution) procedure is to locate a parameter vector that minimizes the difference between experimental data ($\mathrm{f_i}$) and model-produced values ($\mathrm{\hat{f}_i}$) in the least squares sense. In general, this procedure can be written using an objective function S(**k**) as follows:

$$\text{Minimize} \quad \left(\mathrm{S}(\mathbf{k}) = \sum_{\mathrm{i=1}}^{\mathrm{M}} \left(E_{\mathrm{i}}(\mathbf{k}) \right)^2 \right) \tag{5-1}$$

where $E_\mathrm{i}(\mathbf{k}) = \mathrm{f_i} - \mathrm{\hat{f}_i}$, 'M' is the total number of experimental observations, and **k** is a parameter vector, which in general consists of transport properties, reaction kinetic constants, relative Raman cross-sections, and other physical parameters.

To evaluate the model part ($\mathrm{\hat{f}_i}$) in Eq. 5-1 in this work, the two-dimensional, axisymmetric model developed in Chapter 2 is used. Coupled balance equations in the model were numerically solved by using a Galerkin finite element method. It is well known for finite element formulations that the explicit presence of the incompressibility constraint in a problem introduces numerical difficulties in matrix manipulations [Gru89, Red93]. With a penalty function formulation employed in this work, the pressure term and the continuity constraint are removed from the balance equations (but implicitly included) to calculate the momentum transport more efficiently. The detailed description of the solution method is explained in Chapter 2.

With a set of estimated parameters obtained by minimizing the objective function (Eq. 5-1), it is informative to know the level of confidence of them. A confidence region of the estimates [Dra81, Mez67], in which the true parameter values are expected to reside, can be shown as a contour of the value ($S(\mathbf{k})$) given in Eq. 5-2. Correlation among the estimates can also be revealed in the contour.

$$S(\mathbf{k}) = S(\hat{\mathbf{k}})\left[1 + \frac{p}{M - p} F(p, M - p, \alpha)\right] \tag{5-2}$$

where $\hat{\mathbf{k}}$ is the estimated parameter vector and 'p' and 'M' represent the number of parameters in the model and the number of observed points, respectively. 'F' is the value of the F-distribution [Dra81] with 'p', 'M', and 'α'. The contour of $S(\mathbf{k})$ shows the 100(1-α) % confidence region for the estimates of parameters.

Alternatively, given an estimated parameter vector ($\hat{\mathbf{k}}$), confidence intervals can be simply estimated from shape of the objective function around the estimates ($\hat{\mathbf{k}}$). In this case, the objective function is linearized around the estimates (Eq. 5-3), the gradient of it is set to zero (Eq. 5-4), the parameter vector is linearized near the estimates (Eq. 5-5), and the variance-covariance matrix (A) for the estimates is obtained (Eq. 5-6).

$$S(\mathbf{k}) \approx \sum_{i=1}^{M} \left(E_i(\hat{\mathbf{k}}) + \left[\nabla_{\mathbf{k}} E_i(\hat{\mathbf{k}}) \right]^T (\mathbf{k} - \hat{\mathbf{k}}) \right)^2 \tag{5-3}$$

$$\nabla_{\mathbf{k}} S(\mathbf{k}) \approx 2 \sum_{i=1}^{M} \left(E_i(\hat{\mathbf{k}}) + \left[\nabla_{\mathbf{k}} E_i(\hat{\mathbf{k}}) \right]^T (\mathbf{k} - \hat{\mathbf{k}}) \right) \nabla_{\mathbf{k}} E_i(\hat{\mathbf{k}}) = 0 \tag{5-4}$$

$$\mathbf{k} \approx \hat{\mathbf{k}} + \mathbf{A}^{-1}\mathbf{c} \tag{5-5}$$

where

$$\mathbf{A} = \sum_{i=1}^{M} \left[\nabla_{\mathbf{k}} E_i(\hat{\mathbf{k}}) \right] \left[\nabla_{\mathbf{k}} E_i(\hat{\mathbf{k}}) \right]^T \tag{5-6}$$

$$\mathbf{c} = -\sum_{i=1}^{M} \left[\nabla_{\mathbf{k}} E_i(\hat{\mathbf{k}}) \right] E_i(\hat{\mathbf{k}}) \tag{5-7}$$

The confidence interval of a parameter is calculated from the corresponding diagonal element of the inverse of matrix **A**, and the Pearson coefficient of correlation between any two parameters is also evaluated from the inverse [Mil86]. It is difficult to illustrate a confidence region in three or more parameter cases and therefore a confidence interval for each parameter can be useful.

The error term $E_i(\mathbf{k})$ in Eq. 5-1 can be written to include experimental uncertainty (σ_i^2) of each experimental observation.

$$E_i(\mathbf{k}) = \frac{f_i(\alpha) - \hat{f}_i(\beta)}{\sigma_i^2} \tag{5-8}$$

where the original parameter vector **k** is divided into two parts (α and β). The quantity σ_i^2 is the variance of measurements for the i-th experimental observation, and it can be approximated with the residual mean square. When Raman spectroscopy is used to obtain concentration information, scattering intensities are raw data measured from the experiments and Raman cross-sections of the measured species are to be extracted. In this case, the cross-section terms should be included in the observation part ($f_i(\alpha)$), and the rest of parameters in the model part ($\hat{f}_i(\beta)$).

5.2.2 Optimization Scheme

5.2.2.1 Deterministic methods

Calculus-based deterministic methods to solve a minimization problem, e.g. Eq. 5-1, usually need evaluation of the first and/or higher order derivatives and inversion of matrices. For instance, in the Newton method [Baz93], an objective function ($S(\mathbf{k})$) is expanded in a Taylor series and a better set of parameters is formulated from the expansion.

$$S(\mathbf{k}^{i+1}) \approx S(\mathbf{k}^{i}) + \left\{\nabla_{\mathbf{k}} S(\mathbf{k}^{i})\right\}^{T}(\mathbf{k}^{i+1}-\mathbf{k}^{i}) + \frac{1}{2}(\mathbf{k}^{i+1}-\mathbf{k}^{i})^{T}\left\{\mathbf{H}(\mathbf{k}^{i})\right\}(\mathbf{k}^{i+1}-\mathbf{k}^{i}) \qquad (5\text{-}9)$$

where $\mathbf{H}(\mathbf{k}^i)$ is the Hessian matrix of $S(\mathbf{k})$ at $\mathbf{k}^i$. If the parameter set $\mathbf{k}^{i+1}$ gives a minimum of the objective function, the first derivative of $S(\mathbf{k})$ at $\mathbf{k}^{i+1}$ is assumed to be zero and an improved parameter set is produced:

$$\mathbf{k}^{i+1} = \mathbf{k}^{i} - \left\{\mathbf{H}(\mathbf{k}^{i})\right\}^{-1}\nabla_{\mathbf{k}} S(\mathbf{k}^{i}) \qquad (5\text{-}10)$$

The first and second derivatives are required to achieve $\mathbf{k}^{i+1}$ as shown in Eq. 5-10. It is not an easy task to evaluate derivatives from experimental data because there are experimental errors confounded in each experimental observation f_j and modeling errors in the estimation $\hat{f}_j$. Derivatives evaluated from experimental data are usually prone to be unstable [Par00] and this instability frequently makes the Hessian matrix ($\mathbf{H}(\mathbf{k}^i)$) uninvertible. Therefore, parameter estimation problems are generally characterized “ill-posed” and not easy to solve. If this is the case, a chosen deterministic method possibly does not work. If the Hessian matrix is positive definite, it is invertible and ensures that a new parameter set $\mathbf{k}^{i+1}$ is better than the previous $\mathbf{k}^{i}$. Therefore, a given problem is necessarily changed to a well-pose one. In a modification of the Newton method, a specific matrix is added to the original Hessian matrix so as to make it positive definite. For example,

$$\mathbf{k}^{i+1} = \mathbf{k}^{i} - \left\{\mathbf{H}(\mathbf{k}^{i}) + \lambda\mathbf{I}\right\}^{-1} \nabla_{\mathbf{k}} \mathrm{S}(\mathbf{k}^{i}) \qquad (5\text{-}11)$$

where $\mathbf{I}$ is the identity matrix and λ is a scalar which is a function of the parameters ($\mathbf{k}^{i}$). This modified method is called the Levenberg-Marquardt method. λ is increased so that the modified Hessian matrix ($\mathbf{H}(\mathbf{k}^{i}) + \lambda\mathbf{I}$) is invertible. If λ is big enough, Eq. 5-11 becomes the method of steepest descent, while λ becomes zero, the equation returns to Eq. 5-10. In practice, λ is adjusted at each step of the search procedure [Baz93]. Various methods are available in producing a decreasing direction or better parameter set such as a successive quadratic programming [Baz93, Tjo92]. As noted by Chavent [Cha73], gradient methods are practically applicable even if there is no result of uniqueness of a solution. Another way to solve Eq. 5-1 is the regularization method. Its basic idea is addition of a stabilizing functional to the original problem as follows:

$$\text{Minimize} \quad \left(\mathrm{M}^{\alpha}(\mathbf{k}) = \sum_{j=1}^{N} \left(E_{i}(\mathbf{k})\right)^{2} + \alpha\Omega(\mathbf{k}) \right) \qquad (5\text{-}12)$$

where $\Omega(\mathbf{k})$ and α are respectively the stabilizing functional and regularization parameter. Their evaluation requires estimations of derivatives and α [Tik77]. As easily recognized, a smoothed functional M^{α} is minimized instead of the original problem (Eq. 5-1) and uniqueness of a solution is an important premise [Ban89, Tik77]. A regularization method was successfully applied to obtain derivatives from experimental data [Par00]. This is basically a generalization of the least square method ($\alpha = 0$).

Calculus-based deterministic methods are usually fast convergent. Estimation of derivatives is, however, a crucial step in most of this kind of methods. The number of evaluations of derivatives increases dramatically as the number of parameters increases. Due to experimental and modeling errors, parameter estimation problems are potentially ill posed [Par00]. In addition, a model ($\hat{f}(\mathbf{k})$) is frequently nonlinear in practice and therefore an objective function ($S(\mathbf{k})$ in Eq. 5-1) possibly has more than one minimum in an interested parameter space. Calculus-based deterministic methods take advantage of properties of derivatives and therefore they are likely stuck at a local minimum. That is a general characteristic of most "hill-climbing" algorithms. Therefore, initial guesses are very important in locating the global optimum with this kind of methods.

In contrast, in a selection (or exhaustive) search, functions in a model are only evaluated and there are neither derivative estimations nor inversion operations. Therefore, the method is basically stable and more likely ensures the global optimum of a problem. Furthermore, the number of parameters does not effect on overall performance as seriously as in deterministic methods. One shortcoming of this kind of methods is that they are based on a lot of evaluations of the objective function and therefore more time-consuming than calculus-based algorithms are. If a selection search can be conducted efficiently, it will be a viable method to locate global minima. It is known that genetic algorithms provide efficient ways of conducting a full domain search.

5.2.2.2 Simple genetic algorithm

The ideas of natural selection and evolution are perceived by Charles Darwin in 1859. Genetic algorithms were developed by Holland [Hol75] in order to utilize these ideas in solving scientific and engineering problems. After that, genetic algorithms have been successfully used in control, parameter estimation, robotics, etc. [Gre86, Man96, Nou02, Par01, Sah00, Wan01]. Mathematical foundations and implementation of genetic algorithms are well explained in Goldberg [Gol89]. Most genetic algorithms commonly have three essential parts:

- **Preparation of the population**: A genetic algorithm works on population, not a single value or vector of parameter(s), and therefore initial population should be prepared.
- **Selection**: Based on fitness of each individual in the population, some individuals are selected for reproduction.
- **Reproduction**: Selected individuals give birth to their offspring. In this part, several genetic operations, e.g. crossover and mutation, are applied to the population. Once initial population is prepared, a genetic algorithm continuously gives better individuals by repeating the selection and reproduction processes.

The reproduction part is the most essential in every genetic algorithm and its working mechanism is explained with the concept of *schema* [Gol89]. In nature, genetic information is coded with the four bases. In a genetic algorithm, various choices of alphabets for the coding are possible to express parameters. Due to several reasons that will be mentioned later, Gray-coded binary representation is widely used in implementation of genetic algorithms. Suppose that the following set of individuals among the binary-represented population show above-average performance: {00111, 01110, 00111, 00110}. A similarity template, i.e. schema (H), can be easily recognized among these individuals: {0*11* : H} where the asterisk denotes any of the chosen alphabets, 0 or 1 in this case. For a schema, the number of fixed positions is called schema order (o) and distance between the first and last alphabets defines the schema length (δ). For the schema H, it has $o(H) = 3$ and $\delta(H) = 3$. High performance schemata (plural of *schema*) act as *building blocks* to form the optimal individual.

With the concept of schema, a mathematical interpretation of the genetic algorithm was formulated by Goldberg [Gol89], from which the following equations (Eqs. 5-13 to 5-16) about schema are summarized. At generation g, there are n instances (or individuals) of a particular schema H among the population; $n = n(H, g)$. At the next step, if selection is based on relative fitness of each individual, then the expected number of instances with the schema H is

$$n(H, g+1) = N\, n(H, g)\, f(H) / \sum_{i=1}^{N} f_i \tag{5-13}$$

where N is the size of the population and f is fitness. Suppose that the average fitness is $\bar{f}$ and that $f(H) = (1+\alpha)\bar{f}$. Then, the reproductive schema growth is rewritten as follows:

$$n(H, g+1) = n(H, 0) \times (1+\alpha)^{g}, \quad g = 0, 1, 2, \ldots \tag{5-14}$$

This equation clearly shows that above-average schemata ($\alpha > 0$) have more probability to reproduce and the fittest schema will prevail in the population in the end. If there are no mechanisms that would introduce new individuals into the population, this genetic algorithm ends up with the fittest out of the initially given individuals.

Two operations are basically used to give diversity to the population: crossover and mutation. Let p_c to be the crossover probability. Then, the reproduction schema growth is

$$n(H, \mathrm{g}+1) \geq n(H, \mathrm{g}) \frac{f(H)}{\bar{f}} \left[1 - \mathrm{p_c} \frac{\delta(H)}{l-1} \right] \tag{5-15}$$

where the term within the square brackets is the survival probability of the schema H after a crossover operation and l is the length of a coded string. The inequality comes because the same schema is involved in not all crossovers. It is noticed from Eq. 5-15 that short, above-average schemata will exponentially prevail in the population. Addition of the mutation operation with probability $\mathrm{p_m}$ (<< 1), the schema growth equation becomes

$$n(H, \mathrm{g}+1) \geq n(H, \mathrm{g}) \frac{f(H)}{\bar{f}} \left[1 - \mathrm{p_c} \frac{\delta(H)}{l-1} - \mathrm{p_m} \mathrm{o}(H) \right] \tag{5-16}$$

This equation is called the schema theorem and indicates that a short, low order, above-average schema will have more probability to reproduce.

5.2.3 Implementation of a Simple Genetic Algorithm

5.2.3.1 Parameters encoding

A parameter vector is encoded with a selected code system, while genetic information in nature is encoded with four bases. An encoded parameter vector, i.e. *structure* corresponds to a genotype in nature and each encoded parameter, i.e. *string* in the encoded vector does to a chromosome. A real parameter vector is obtained from an encoded parameter vector as a phenotype (i.e., organism) is realized from a genotype. All operations in genetic algorithms are performed in the encoded parameter level. The length of a string is determined by the number of required significant decimal digits to satisfactorily express the corresponding parameter. If the binary (*base*) system is adopted in encoding, then the string length (*lchro*) to express *lpara* digits in decimal is calculated in writing a simulation code using

$$lchro = \text{integer of}\left\{\frac{lpara}{\log_{10}(base)}\right\} + 1 \tag{5-17}$$

where the integer part of the content in the parentheses is considered. Total length of a structure is determined from the length of a string and the number of parameters to be estimated. In addition, there is the same number of structures as the size of population in each generation. All genetic operations are applied to whole population in each generation and therefore a predetermined number (N) of structures are initially generated randomly.

All operations in genetic algorithms are usually applied to encoded parameter vectors (structures), not real parameters. Various choices of parameter coding are acceptable in genetic algorithms. Binary coding is the most popular because it provides maximum number of schemata and minimum alphabets (0 and 1). Some limitations of binary coding should be, however, mentioned. If the number of parameters is large and required precision is high, then total size of a solution array becomes large and so is the size of search space. In this situation, it is recognized that binary coding is not efficient and floating point chromosome is a viable remedy [Mic95]. If normal binary numbers are used in coding, performance of the genetic algorithm is possibly hampered by the presence of a probabilistic barrier, called the Hamming wall. For example, decimal numbers 9 and 10 are 1001 and 1010, respectively, in the binary system. Two operations are required in changing a parameter from 1001 to 1010, even though the difference between them is only one. This problem is more serious if decimal digits are used in encoding parameters. When the Gray coding [Pre92b] is used, this wall is effectively removed because any two consecutive integers have only one bit difference in the Gray coding. Therefore, Gray-coded binary strings are used in representing parameters in the current implementation.

5.2.3.2 Selection

In the previous Goldberg's analysis, raw fitness was used in the selection process. One thing undesirable with using raw fitness is that the genetic algorithm may produce premature solutions because one exceptionally good individual can dominate reproduction. To prevent this premature convergence, fitness values are linearly scaled in the current implementation. Several issues about the linear scaling are discussed by Goldberg [Gol89]. A pair of individual strings is selected for reproduction with a Roulette wheel, which consists of scaled fitness values of all individuals.

5.2.3.3 Reproduction

A selected pair of structures undergoes the reproduction step where crossover, mutation, and other operations are performed. Some of operations in genetic algorithms were well explained in Man *et al.* [Man96]. Crossover is activated with a predetermined probability (p_c) and the number of crossover points is not necessarily one. The number of crossover points is currently set to two, and the positions are determined randomly. The parts between two crossover points are exchanged between the two selected structures and the crossover operation produces two offspring. Therefore, crossover operations generate new population of the same size as that of the previous one (N).

Mutation operations are applied to each individual of the new population with variable or fixed probability (p_m). The mutation operation in the current implementation is bitwise. If the random number generated at one specific bit position is bigger than the mutation probability, then the bit is altered to the complementary bit value. With variable mutation probability, diversity of population can be maintained throughout the solution process, while a fixed probability works better in some cases where diversity is provided by other measures, e.g. the crowding model that is depicted in Section 5.2.3.5. The mutation probability can be adjusted based on the difference between the fittest and median. Other genetic operations such as inversion can be added in order to give diversity to population, but they are not effective as cross over or mutation operations.

After the reproduction step, the number of total available structures, i.e. encoded parameter vectors, is twice as many as in the previous population. To maintain the size (N) of population in each generation, N structures are selected from the available 2N genotypes based on their fitness or newly generated population is simply transferred to the next generation. The best performing structure in the previous generation survives the reproduction step with the first strategy, or the best individual is directly copied to the next generation by replacing the worst among the new population (Elitism).

5.2.3.4 Performance tests

To evaluate capability of the current implementation of a simple genetic algorithm, two example problems were tested. In genetic algorithms, each operation was activated with a specific probability, e.g. crossover probability (p_c) and mutation probability (p_m). There are some guidelines to set these probabilities depending on the size of population [Gre86, Wan01]. Each probability is not universally fixed but dependent on a specific problem. Given size of population a proper range of each probability can be estimated while these test problems are performed.

Test case 1.

The first test problem [Gen97] is given in the following statement and the shape of the objective function is shown in Figure 5-1.

Problem 1: Maximize $\{x \sin(4\pi x) + y \sin(20\pi y) + 21.5\}$
where $x \in [-3.0, 12.1]$ and $y \in [4.1, 5.8]$.

The objective function has lots of local optima (Figure 5-1) and therefore a usual calculus-based method is prone to fall into one of local optima. In this test, the size of population was 30 and crossover and initial mutation probabilities were 0.95 and 0.022, respectively. As explained in the implementation section, the mutation probability was adjusted by monitoring diversity of the population. Number of significant digits was set to 5 in this test.

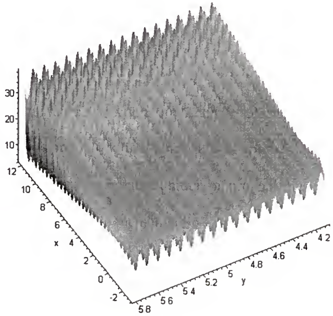

Figure 5-1. The shape of the objective function in Problem 1.

The test results are shown in Figure 5-2. The fittest and median of each generation are shown together with mutation probability as generations are developing. Performance of the best parameter set showed fast convergence and the mutation probability line showed adaptation to maintain diversity within population as intended.

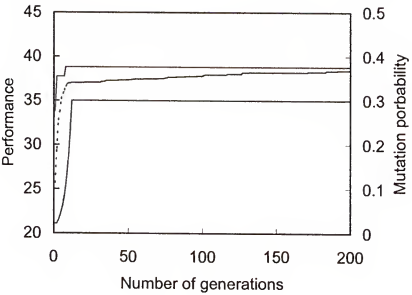

Figure 5-2. Performance of the genetic algorithm for Problem 1. The lines represent the best and median individuals and mutation probability from the top.

The obtained optimum of the objective function was 38.822 at (11.631, 5.7252). The value in the reference is 38.818 at (11.6314, 5.7248). It took 4190 evaluations of the objective function to reach these values in the reference whereas 300 evaluations in the current implementation. It should be, however, mentioned that this combination of population size, crossover and mutation probabilities does not always guarantee an outstanding convergence in other problems.

Test case 2.

The second test problem [Cha95] is stated in the following and the shape of the objective function is depicted in Figure 5-3.

Problem 2: Maximize $\left\{\cos^2(n\pi r)\exp[-(r/\sigma)^2]\right\}$

$$\text{where } r^2 = (x - x_0)^2 + (y - y_0)^2 \text{ and } \quad x, y \in [0, 1].$$

The objective function has its global maximum at 1 and the second maximum at 0.92. The area for the global maximum in the parameter range is very small and therefore the probability of finding the optimum is very low if a random search is performed. In this test, the population size, crossover probability, and initial mutation probability were 30, 0.95, and 0.023, respectively. To see problem-dependent performance of the genetic algorithm, the position (x_0 and y_0) of the optimum was changed.

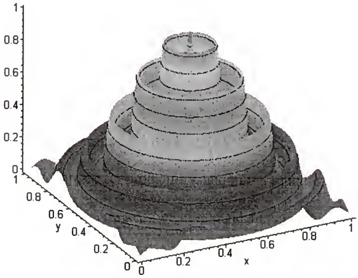

Figure 5-3. The shape of the objective function in Problem 2: $f(x,y) = \cos^2(n\pi r) \exp[-(r/\sigma)^2]$where $r^2 = (x-0.5)^2 + (y-0.5)^2$, $n = 9$ and $\sigma^2 = 0.15$.

The test results for this problem are represented in Figure 5-4, where the second maximum is marked with the dashed lines. The upper, middle, and lower lines represent the best and median parameter sets, and the mutation probability throughout the process. It is evident from Figure 5-4 that the genetic algorithm located a set of parameters that gave a better fitness than the second maximum within less than thirty generations for both cases: 14 for the first case and 29 for the second. The rest of generations were not essential for finding the optimum but for finalizing the parameters.

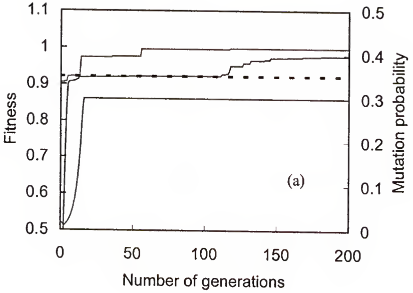

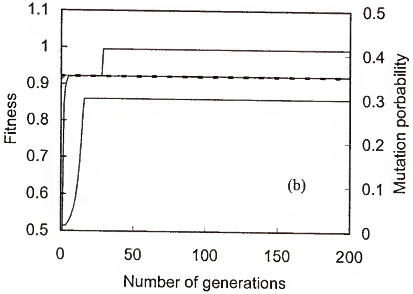

Figure 5-4. Test results for the second problem: (a) $x_0 = 0.3$ and $y_0 = 0.3$, and (b) $x_0 = 0.5$ and $y_0 = 0.5$ in Problem 2. The lines represent the best and median individuals and mutation probability from the top.

The above two tests show that the current genetic algorithm is capable of locating a neighborhood of the global optimum position quickly within initially given ranges of parameters. It is also noticed that the genetic algorithm is not good at fine-tuning the parameters. This characteristic is common in most genetic algorithms and therefore another method should be adapted for expediting the fine-tuning. Of cause, genetic algorithms would locate estimates with good accuracy if enough number of generations and string length were provided. In this work, the reactor model contains a number of partial differential equations (PDE's) and even a single evaluation of the objective function, S(**k**), in Eq. 5-1 costs considerably more computational time than the objective functions in two test problems. Therefore, it is a reasonable strategy to determine the neighborhood of the global optimum using the genetic algorithm and then to locate the global optimum using a locally convergent, more efficient algorithm. Several locally efficient algorithms are available, e.g., the Levenberg-Marquardt [Par01], Simplex [Wan01], or modified Powell [Oka98] method. Calculus-based deterministic algorithms [Baz93] usually show fast convergence, because they take advantage of extra information about the objective function, e.g. derivatives of the objective function. The number of required evaluations of derivatives, however, usually increases dramatically as the number of parameters increases. In addition, evaluating derivatives from experimental data is prone to be unstable [Par00a] and this can make the Hessian matrix uninvertible. Therefore, the simplex method [Pre92a] is chosen for fine-tuning estimated parameters in this work. No derivative estimation is required with this method and therefore there is no requirement for an objective function to well-behave.

5.2.3.5 Crowding model – an advanced concept

The simple genetic algorithm implemented in this chapter worked well for the complex objective functions in the test cases. It is, however, generally known that genetic algorithms may not perform efficiently on multimodal objective functions. This degraded performance was explained, in similarity, by increased competition for limited resources

[Gol89]. Technically speaking, most individuals become concentrated at a niche of a small region and therefore effectiveness of genetic algorithms is considerably lowered. To resolve this situation, it was suggested that resemblance between a parents and a newborn be utilized in selecting individuals to survive and be transferred to the next generation [Gol89]. This is the fundamental idea of the crowding model.

The crowding model in this work was implemented by adding an intermediate stage after the reproduction step. After the reproduction step, several newborns are selected given a parent and the newborn most resemble to the parent is selected to survive. The number of newborns in comparison is termed the crowding factor (CF). The crowding model would be activated for cases where objective functions are too complex to obtain reasonable estimates with the simple genetic algorithm.

5.2.4 Summary

A parameter estimation procedure was established to extract physical parameters related to CVD processes, which consists of *in situ* experimental data collection and computational analysis. A two-dimensional axisymmetric reactor model developed Chapter 2 was combined with an optimization scheme for physical parameter estimation. After getting estimates of the parameters, the confidence region or interval of each parameter should be evaluated. Specific applications would be shown in the following section.

A simple genetic algorithm was used in the minimization process, which performs a full domain search efficiently and does not need derivatives evaluation. The simple genetic algorithm was tested with two test problems and proven effective. The test results revealed that the simple genetic algorithm was fast in finding neighborhood of the global optimum, but slow in fine-tuning the estimates. To expedite the fine-tuning, a Simplex algorithm was adopted to follow the genetic algorithm. This strategy is reasonable because the reactor model in this work consists of several partial differential equations and a single evaluation of the model costs a long computation time.

5.3 Application to Mass Transport

5.3.1 Introduction

MOCVD is widely used to deposit thin semiconductor films with good crystalline quality and electrical properties [Kol98]. MOCVD processes are, however, influenced by several factors such as the choice of carrier gas [Tho96], substrate material and its surface preparation [Sug97], and the gas dynamics inside the reactor including the thermal boundary conditions [Fot90b]. Therefore, obtaining a realistic reactor model based on fundamental understanding of the process would be useful, for example, for optimizing an existing process or designing a new reactor. Accurate reaction kinetic information about homogeneous and heterogeneous chemical reactions in the reactor and the thermophysical properties of the gas components are required to develop a realistic model.

Raman spectroscopy can simultaneously provide temperature and composition information with good spatial resolution and therefore accurate reaction kinetic information can be obtained without disturbing the observed process. It requires, however, *a priori* Raman scattering cross-section data of the observed chemical species to quantitatively obtain the species concentration information from the measured scattering intensities. Given cross-sections, other physical properties such as the mass diffusivity in a carrier gas can be estimated measured composition profiles. While Raman scattering cross-sections of many common gases are well tabulated [Sch79], those of metalorganic precursors and their reaction derivatives are rarely available and need to be determined prior to quantitative treatment of Raman data taken from a MOCVD process.

Cross-sections of stable species are usually determined from controlled experiments with a known concentration of the gas mixture. Reaction intermediates of metalorganic precursors, however, are often not sufficiently stable to maintain their concentration constant during the measurement, and thus to independently measure cross-sections and other properties. For these species, it would be convenient to simultaneously estimate the cross-section along with other physical parameters (e.g., reaction kinetic constants, diffusivity) from a set of measurement results.

An up flow cold-wall CVD reactor was used in this study and experimental observation of composition profiles was made using *in situ* Raman spectroscopy. The detailed reactor model developed in Chapter 2 was combined with optimization algorithms to establish the estimation procedure. As test cases, binary diffusivities of CH_4/N_2 and NH_3/N_2 mixtures as well as Raman cross-sections of the constituents in the gas mixture were estimated by the procedure.

5.3.2 Experimental

An up flow, cold-wall CVD reactor interfaced with a high resolution Raman spectrometer was used for this study. The reactor incorporated an axisymmetric design to simplify the modeling work. Gases were introduced through three concentric inlets at the bottom of the reactor, and labeled center, annulus, and sweep inlets, respectively in Figure 5-5. Entering gases impinged upon a susceptor, which is the bottom surface of a quartz envelope and faces down towards the inlets at an adjustable distance. The heating unit was not activated. A Raman spectrometer (Ramanor U-1000, Jobin-Yvon) was used to collect Raman scattering signals from the chemical species in the reactor, and the signal collection was made along the centerline of the reactor. The 488 nm line of an argon ion laser (Innova 90, Coherent Lasers) was focused at a variable position on the centerline and Raman signals were gathered in a right angle configuration to the incident laser beam. The experimental set up is described in detail in Chapter 2.

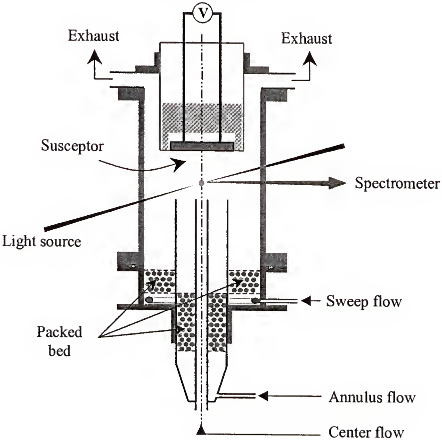

Figure 5-5. Schematic of the reactor used in parameter estimation.

Methane or ammonia diluted in nitrogen was used as a test gas and introduced into the reactor through the annulus inlet, while pure nitrogen was introduced through the other two inlets. Test gas concentrations at the annulus inlet were controlled by mass flow controllers. Each experiment in this study was conducted at room temperature (23 °C) and at 1 atm pressure, and a single value of the gas velocity was set at the three inlets. Methane dispersion experiments were carried out at three different gas velocities; 2.5, 3.5, and 4.5 cm/s, and, in those experiments, the methane concentration at the annulus inlet was maintained at 1.91, 1.36, and 1.06 mole %, respectively. The Raman scattering intensity of the symmetric C-H stretching vibration from methane at 2916 cm^{-1} was monitored to determine the methane concentration profile in the reactor. In the ammonia dispersion experiments, 4.0 and 8.0 mole % NH_3 in N_2 were used, and the gas velocities at the inlets were set at 2.5 cm/s. The ammonia signal was observed at 3335 cm^{-1}, which corresponds to the symmetric stretching of N-H. The intensity of the nitrogen Q-branch at 2331 cm^{-1} was also monitored at the same spatial position in the reactor and used as an internal standard for quantitative concentration measurement [Sch79].

5.3.3 Problem Formulation

Solution of the parameter estimation problem (so called "inverse problem") is based on the method of maximum likelihood [Dra81]. To extract physical parameters from the experimental observations, i.e. Raman intensities, an optimization scheme is required as well as a validated reactor model. The solution procedure is to locate a parameter vector that minimizes the difference between experimental data (f_i) and model-produced values ($\hat{\mathrm{f}}_i$) in the least squares sense. In general, the objective function (S(**k**)) to be minimized can be written as follows:

$$\mathrm{S}(\mathbf{k}) = \sum_{\mathrm{i=1}}^{\mathrm{M}} \left(E_{\mathrm{i}}(\mathbf{k})\right)^2 \tag{5-18}$$

where $E_{\mathrm{i}}(\mathbf{k}) = \mathrm{f}_{\mathrm{i}} - \hat{\mathrm{f}}_{\mathrm{i}}$, 'M' is the total number of observations, and **k** is a parameter vector, which in general consists of transport properties, reaction kinetic constants, relative Raman cross-sections, and other process parameters. In the present study, f_i and $\hat{\mathrm{f}}_i$ represent the observed and estimated species mole fractions, respectively. The parameter vector **k** has two elements, i.e., the binary diffusivity (*D*) and relative Raman cross-section (Σ_j) of species j. The relative Raman cross-section is defined as the ratio of the Raman cross-section of a species j to that of nitrogen Q-branch [Sch79]. In the optimization the cross-section is directly used, while the binary diffusivity (D in m^2/s) is reparameterized ($\widetilde{D}$) to render it more tractable:

$$\widetilde{D} = 7 + \log_{10} D \qquad (5\text{-}19)$$

The relative Raman cross-section is implicitly included in f_i because scattering intensities, not mole fractions (f_i), were recorded in the mass dispersion experiments, while the binary diffusivity is included in the model side ($\hat{f}_i$). This type of parameter separation is an approach to avoid complex formulation. Finally, the mathematical form of the objective function in this study becomes

$$S(\mathbf{k}) = \sum_{i=1}^{M} \left(\left\{ 1 + \left(\frac{\widetilde{\nu}_0 - \widetilde{\nu}_j}{\widetilde{\nu}_0 - \widetilde{\nu}_Q} \right)^4 \frac{1 - \exp(-hc\,\widetilde{\nu}_Q / k_B T_i)}{1 - \exp(-hc\,\widetilde{\nu}_j / k_B T_i)} \left(\frac{\mathbf{I}_Q}{\mathbf{I}_j} \right)_i \Sigma_j \right\}^{-1} - \hat{f}_i \right)^2 \qquad (5\text{-}20)$$

where $\widetilde{\nu}$, h, c, k_B, T, $\mathbf{I}$, and Σ_j represent wave number, Planck constant (= 6.626×10^{-34} Js), speed of light (= 2.998×10^{8} m/s), Boltzmann constant (= 1.381×10^{-23} J/K), thermodynamic temperature, scattering intensity, and the relative Raman cross-section of species j, respectively. Subscripts 0, j, and Q denote the incident light, species j, and nitrogen Q branch, respectively. Among these quantities, scattering intensity and temperature are measured experimentally.

To evaluate the model side ($\hat{f}_i$) in Eq. 5-20, a two-dimensional, axisymmetric model was developed in Chapter 2. Coupled balance equations in the model were numerically solved by using the Galerkin finite element method. It is well known for finite element formulations that the explicit presence of the incompressibility constraint in a problem introduces numerical difficulties in matrix manipulations [Gru89, Red93]. With the penalty function formulation employed in this study, the pressure term and the continuity constraint are removed from the balance equations (but implicitly included) to calculate the momentum transport more efficiently. The detailed description of the solution method is explained Chapter 2.

5.3.4 Optimization Scheme

A genetic algorithm was implemented for the parameter estimation procedure as an optimization scheme (i.e. minimization of Eq. 5-20). The reactor model in this study contains a set of nonlinear partial differential equations and therefore it is likely that the parameter space is highly non-linear. Experimental errors included in the objective function also make the problem more difficult. Genetic algorithms have been shown to be successful in solving optimization problems of nonlinear systems [Oka98, Par00b], and they are especially efficient for full domain searches. Genetic algorithms are, however, sometimes not successful in locating the global optimum value without proper fitness scaling and advanced operators to expedite the convergence [Gol89, Jun98]. The Simplex algorithm was combined with a simple genetic algorithm to expedite the convergence because it is known to be robust [Pre92a] and does not require evaluation of derivatives of the objective function.

In the current implementation of a genetic algorithm, the Gray coding scheme [Pre92b] was adopted to evade the Hamming wall, a linearly scaled fitness approach [Gol89] to prevent premature convergence, and Elitism to preserve the best parameter set of each generation. A two-point crossover scheme was also incorporated, as it is known in general to be more efficient than the one-point crossover approach [Gre86]. There are a few control parameters for the genetic algorithm (e.g., population size, crossover probability, mutation probability) and they were determined with the assistance of reported guidelines [Gre86, Wan01] and by solving test problems. The population size of 30, crossover probability of 0.95, and initial mutation probability of 0.023 were used in this study. The mutation probability was adjusted throughout generations to maintain diversity in population [Cha95].

5.3.5 Applications and Discussion

The parameter estimation procedure developed in this study was applied to extracting physical properties from experimentally measured Raman scattering intensities in a cold-wall CVD reactor (Figure 5-5). The gas diffusivity and Raman cross-section of methane and ammonia in nitrogen were determined from gas dispersion experiments at room temperature.

Results of the dispersion experiments for CH_4/N_2 and NH_3/N_2 are represented in Figures 5-6 and 5-7, respectively. These figures plot the concentration of a species introduced in the annulus and measured along the reactor centerline as a function of distance from the susceptor. The vertical dashed lines in these figures denote the position of the inlets. The measured centerline mole fractions represented by the symbols are very low near the inlet, and increase as the gas flows toward the susceptor due to mass transport at the high annulus concentration to the initially CH_4 or NH_3 free center inlet stream. If the distance traveled by the gas is sufficiently long, the mole fraction at the centerline of the reactor will decrease after it reaches a maximum value since mass transport in the radial direction is dominant after the maximum.

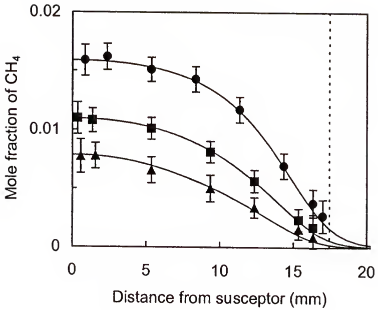

Figure 5-6. Measured and simulated axial concentration profiles for the gas velocity of 2.5 (●), 3.5 (■), and 4.5 (▲) cm/s at the inlets. Diluted methane was introduced through the annulus inlet and its location is indicated by the vertical dashed line.

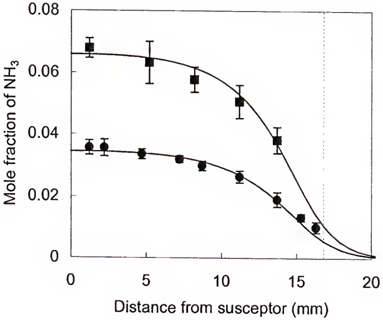

Figure 5-7. Measured and simulated axial concentration profiles for inlet concentration 4 (●) and 8 (■) mol % ammonia in N_2.

The experimental results shown in Figures 5-6 and 5-7 were calculated from intensities of Raman scattering signals with estimates of the relative Raman cross-sections. In addition, the solid lines in these figures were produced by the reactor model with the estimated values of the gas diffusivity. The same values of control parameters for the genetic algorithm were used as in the test problem. The search space for the diffusivity ranged from 10^{-6} to 10^{-4} m^2/s and that for the relative Raman cross-section ranged from 1 to 10. These ranges are reasonably wide for common gases.

Performance of the combined optimization procedure is shown in Figure 5-8 for the methane case with inlet velocity of 2.5 cm/s.

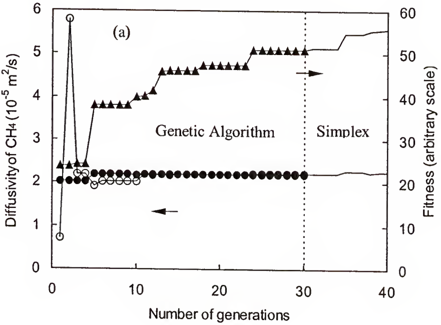

Figure 5-8. Performance of the parameter estimation procedure: (a) diffusivity (●,○) and (b) relative Raman cross-section (◆,◇) of methane at 23 °C. Fitness (▲) and mutation probability (■) are also shown for each generation. The filled and empty symbols respectively denote the best and medium performance parameters at each generation.

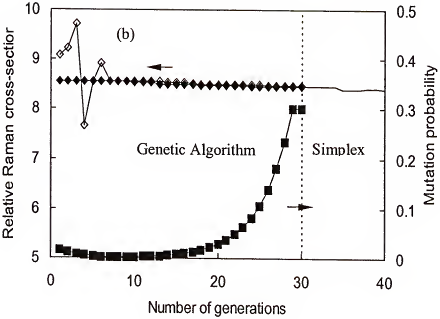

Figure 5-8. Continued.

With the genetic algorithm, the neighborhood of the optimum diffusivity was found in 5 generations (Figure 5-8a) and a good estimate of the Raman cross-section was found at the first generation (Figure 5-8b). The fitness behavior in Figure 5-8a clearly shows that most of the generations were used for fine-tuning the estimates as the Simplex algorithm was engaged. Open symbols in the figure represent values of the parameter with the medium performance in each generation. These show that diversity in population is still maintained even after the neighborhoods of optimum parameter values are found. The mutation probability was adjusted throughout the generations to maintain the diversity in population (Figure 5-8b). Performance behaviors of the estimation procedure for the 3.5 and 4.5 cm/s inlet velocity cases were found to be as efficient as the 2.5 cm/s case. The optimization procedure was also successful for the ammonia dispersion cases, yet slower than the methane cases, e.g. a neighborhood was found after 15 generations for the 4 mole % cases.

The estimated values of the parameters are summarized in Tables 5-1 and 5-2, and the ranges given in the tables for the two parameters are the confidence intervals with 95 % confidence, which were obtained by numerically evaluating Eq. 5-6, while the contour of Eq. 5-2 gives a more precise confidence region.

Table 5-1. Parameter estimation results from methane dispersion experiments.

Velocity (cm/s)	Diffusivity (10^{-5} m^2/s)	Cross-section (Σ_j)	Correlation
2.5	2.25 ± 0.13	8.40 ± 0.15	-0.635
3.5	2.42 ± 0.08	8.29 ± 0.11	-0.780
4.5	2.45 ± 0.30	8.14 ± 0.50	-0.854
Reference	2.14 [15]	6.8 – 9.2 [24]	-

Table 5-2. Parameter estimation results from ammonia dispersion experiments.

% NH_3	Diffusivity (10^{-5} m^2/s)	Cross-section (Σ_j)	Correlation
4.1	2.90 ± 0.31	4.30 ± 0.14	-0.471
8.0	2.81 ± 0.47	4.23 ± 0.05	0.193
Reference	2.33 [42]	4.5 – 6.4 [24]	-

The Pearson coefficient of correlation between the two parameters was evaluated as previously explained. The correlation is stronger if the absolute value of the coefficient is closer to one. For the methane cases, the average estimated diffusivity was $(2.37 \pm 0.11)\times10^{-5}$ m^2/s and that of Raman cross-section was 8.28 ± 0.18. The Chapman-Enskog theory gives the binary diffusivity of methane in nitrogen as 2.14×10^{-5} m^2/s, which is widely used for diffusivity estimation of species commonly used in MOCVD reactors [Hol92] and known to be valid for non-polar gases [Bir60]. The current estimate agrees within less than 10 % error with this value. Reported values of the relative cross-section of methane range from 6.8 to 9.2 [Sch79], and the current estimate lies in this range as well. Therefore, it is concluded that the parameter estimation procedure developed in this study provides accurate estimates of physical parameters.

For the ammonia cases (Table 5-2), the average values of the estimates were $(2.85 \pm 0.29)\times10^{-5}$ m^2/s and 4.26 ± 0.07 for the diffusivity and relative Raman cross-section, respectively. A reported diffusivity value of NH_3/N_2 is 2.33×10^{-5} m^2/s at 25 °C [Pol01], and reported values of the relative cross-section as measured in room temperature gas cells range from 4.5 to 6.4 [Sch79]. The wide range of the reported values of relative Raman cross-section suggests that experiments are sensitive to the measurement setup. The current estimate of the relative Raman cross-section is close to the reported range. The uncertainties of the diffusivities show that the current experimental data for NH_3/N_2 contain more experimental errors than for CH_4/N_2.

To further substantiate the effectiveness of the parameter estimation procedure and to obtain more precise information about trusted regions, an exhaustive search was conducted near the estimates for NH_3/N_2 and the result is shown in Figure 5-9. The contour at the center represents the 95 % confidence region in the parameter space, which is apparently wider than confidence intervals given in the previous paragraph: $3.92 \sim 4.78$ for the cross-section and $(2.14 \sim 4.17)\times10^{-5}$ m^2/s for the diffusivity. However, confidence regions in three or more dimensions are difficult to visualize, while the confidence interval for each parameter is easily calculated (Eq. 5-6).

The objective function seems to have distinctive minimum in the physically meaningful parameter space. It is noticed in Figure 5-9 that the objective function has a narrow, deep minimum for the reparameterized diffusivity at around the estimates, even though a wide range ($10^{-6} \sim 10^{-4}$ m^2/s) was searched in the actual diffusivity space. Therefore, it is considered that the proposed parameter estimation procedure is effective for estimating parameters from experimental observations.

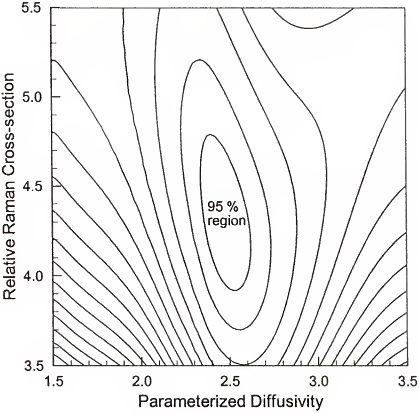

Figure 5-9. Shape of the objective function near the estimates for the ammonia case. The innermost contour represents the 95 % confidence region.

For a quantitative analysis of spectroscopic data, a value of the cross-section of an interested species is required. For stable species, cross-sections can be independently determined by measuring the scattering intensity of the species in a gas mixture of a known concentration. It is, however, very difficult to determine cross-sections of unstable species (e.g. reaction intermediates of metalorganic precursors) using the conventional methods, because their concentration is affected by chemical and/or transport processes and thus not readily known. In this respect, it is significant that the estimation procedure developed in this study is able to simultaneously extract cross-section and other physical parameters (e.g. diffusivity), which plays a major role in species transport in the reactor.

5.3.6 Conclusions

A parameter estimation procedure that combines *in situ* Raman probing, a detailed reactor modeling, and optimization algorithms has been established in this study. Two widely studied gas species, CH_4 and NH_3, were used to test the numerical procedure. The parameter estimation procedure was able to simultaneously extract physical parameters of test systems, i.e. relative Raman cross-section and diffusivity, from experimental data for these two species. The estimated values were in good agreement with those reported in the literature.

Although gas phase diffusivities can be reasonably estimated (e.g. Chapman-Enskog theory) and the Raman cross-section of a stable species can be experimentally probed in simpler reactor designs, the current analysis is anticipated to be particularly valuable in extracting Raman cross-sections of reaction intermediates. Values of the cross-sections of intermediates are necessary to quantitatively analyze *in-situ* experimental observation. It is important to note that a realistic reactor model can incorporate relevant transport phenomena as well as chemical reactions that control concentrations of the species under investigation. Therefore, it is anticipated that the parameter estimation procedure developed in this study can be effectively applied to studying gas phase reaction kinetics of metalorganic precursors in actual flow conditions, providing reaction kinetic data with less ambiguity. This procedure also has the potential to extract multiple parameters from a single experiment.

CHAPTER 6
BEHAVIOR OF AMMONIA AND TRIMETHYLALUMINUM

6.1 Ammonia Decomposition

6.1.1 Introduction

Ammonia is the most popular nitrogen source for Group III-nitrides semiconductor materials, but it is thermally stable even at usual nitrides growth temperatures. For example, it was reported [Mes98] that only 4 mole % of ammonia reacted with gallium and formed GaN film at 700 °C. This low decomposition efficiency is one of the reasons that a large excess of ammonia is used compared with that of the group III source (e.g., TMAl, TMGa, and TMIn).

The homogeneous decomposition of ammonia is very well studied and described by a second order reaction with activation energy greater than 90 kcal/mol [Dav90, Dov79]. Gas phase decomposition of ammonia is known to occur according to:

$$NH_3 + M \rightarrow NH_2 + H + M \qquad (6\text{-}1a)$$
$$NH_2 + H \rightarrow NH + H_2 \qquad (6\text{-}1b)$$

where M denotes a carrier gas or another ammonia molecule. The activation energy for the second reaction was reported to be 36.5 kcal/mol [Dav90]. The high activation energy for the first step, however, suggests that homogeneous decomposition is negligible at most of the MOCVD conditions (up to 1000 °C) and explains the aforementioned low decomposition efficiency of ammonia.

When surfaces are involved in ammonia decomposition, the following sequences were suggested:

$$NH_3(g) + S \rightarrow NH_3(ad) \tag{6-2a}$$
$$NH_3(ad) \Leftrightarrow NH(ad) + H_2(g) \tag{6-2b}$$

The heterogeneous decomposition of ammonia was studied for several surfaces [Kim94, Liu78, Mes98]. It was reported [Dil91] that ammonia dissociated upon adsorption even at 300 K on silicon surfaces. Using Fourier transmission infrared spectroscopy, Si-H_2 and Si-NH_2 were mainly observed at 300 K, while Si-H and Si_3-N were observed above 600 K. It was proposed in that study that Si-NH_2 decompose into Si-H and Si_3-N at high temperature and Si_3-N was the major species at temperatures higher than 700 K. H_2 was released from silicon surface above 660 K [Gup88].

Tamaru [Tam88] studied ammonia decomposition on transition metals and suggested the kinetic rate equations should be divided into two empirical models:

$$r = k K P_{NH_3} / \left(1 + K P_{NH_3}\right) \tag{6-3a}$$

$$r = k\left(P_{NH_3}^2 / P_{H_2}^3\right)^{\alpha} \tag{6-3b}$$

where k, K, and α are constants. The first equation was obtained using tungsten and the second was using iron. It was also reported that the decomposition of ammonia on most transition metals was described by the second equation.

In the following, ammonia is tested for possible gas phase and surface reactions using a measurement reactor, its validated model, and *in situ* Raman spectroscopy.

6.1.2 Experimental

An up flow, cold-wall CVD reactor was used in this study as schematically depicted in Figure 8-1. The height of the free space in the annulus channel after the glass bead packing was 6 mm. Nitrogen was supplied into the reactor through the center and sweep inlets, while 8 mole % NH_3/N_2 was introduced to the reactor through the annular inlet. The ammonia concentration at the inlet was controlled with mass flow controllers (UNIT Instruments). The nominal gas velocity was set at 2.5 cm/s for all inlet flows. The 532 nm line from a solid-state laser (Verdi 8, Coherent Lasers) was focused into a detection point on the centerline of the reactor. The laser power was set at 3 W. The reactor assembly was put on a 2-D stage to allow spatial scan with respect to the spatially fixed laser line.

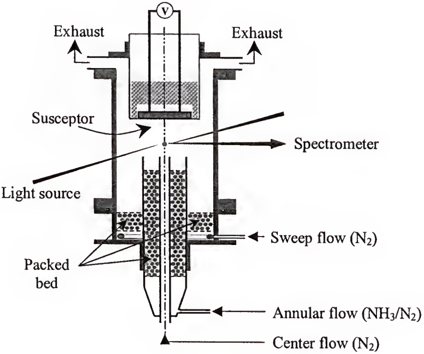

Figure 6-1. Schematic of the reactor for ammonia study.

The scattered signals from the focused spot were colleted at a right angle to the laser line with a Raman spectrometer (Ramanor U-1000, Jobin-Yvon). Gas temperature at each detection point was estimated from the nitrogen rotation band. For a quantitative analysis of ammonia concentration, intensities of the ammonia vibration at 3335 cm^{-1} and the nitrogen Q-branch at 2331 cm^{-1} were recorded for each detection point. A set of experiments was performed with four different heater temperatures: 300, 500, 700, and 900 °C. The heater temperature was measured with a thermocouple placed beneath the heater assembly.

6.1.3 Results and Discussion

The experimental results are presented in Figure 6-2. Open and filled circles in the figure respectively denote experimental values of gas temperature and ammonia mole fraction. The gas temperature was estimated from the nitrogen rotation band using Eq. 3-21. The ammonia mole fraction was calculated from the intensity ratio using the following equation (see Eqs. 3-24 and 3-25):

$$x_{NH_3} = \left\{ 1 + \left(\frac{\tilde{\nu}_0 - \tilde{\nu}_{NH_3}}{\tilde{\nu}_0 - \tilde{\nu}_Q} \right)^4 \frac{1 - \exp(-hc\tilde{\nu}_Q / k_B T)}{1 - \exp(-hc\tilde{\nu}_{NH_3} / k_B T)} \left(\frac{I_Q}{I_{NH_3}} \right) \Sigma_{NH_3} \right\}^{-1} \tag{6-4}$$

where $\tilde{\nu}$, h, c, k_B, T, $\mathbf{I}$, and Σ_{NH_3} represent the wave number, Planck's constant (= 6.626×10^{-34} Js), speed of light (= 2.998×10^{8} m/s), Boltzmann constant (= 1.381×10^{-23} J/K), thermodynamic temperature, scattering intensity, and the relative Raman cross-section of ammonia, respectively. Subscripts 0 and Q denote the incident light and the nitrogen Q branch at 2331 cm^{-1}, respectively. Among these quantities, scattering intensity and temperature are measured experimentally.

The lines in Figure 6-2 are generated by the reactor model developed in Chapter 2. The solid lines were obtained by including surface reaction on the susceptor surface, while the dashed lines were calculated without any reactions. It is noticed from the figure that ammonia mainly decomposes by surface reactions while gas phase reactions give negligible contribution to its decomposition. In this analysis, the surface reaction rate was estimated from kinetic theory using Eq. 6-5 [Mou91, Saf97] with ammonia concentration (C_{NH_3}) in the gas phase.

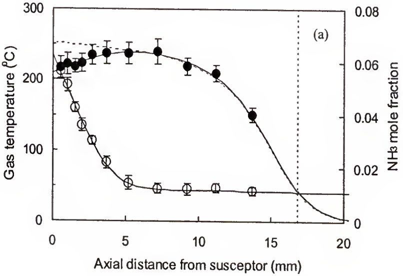

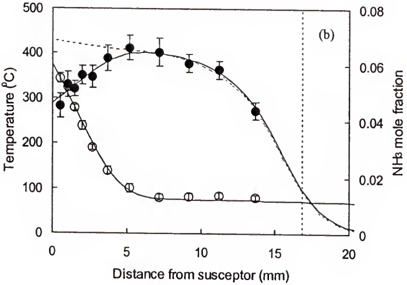

Figure 6-2. Ammonia concentration (●) and gas temperature (O) profiles along the centerline of the reactor at different heater temperatures: (a) 300, (b) 500, (c) 700, and (d) 900 °C. The surface reaction was included in the solid line, while no reactions were considered in the dotted line.

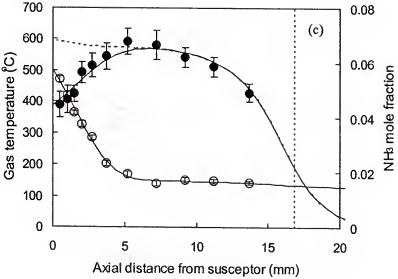

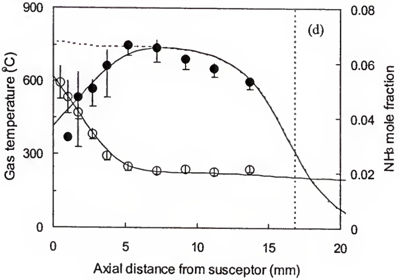

Figure 6-2. Continued.

$$\frac{dC_{NH_3}}{dt} = -\sqrt{\frac{RT}{2\pi M}}\, e^{-E_S/RT} C_{NH_3} \tag{6-5}$$

where R, T, M, E_S, and C_{NH_3} are gas constant, temperature, molecular weight of ammonia, activation energy for the surface reaction, and ammonia concentration just above the surface in the gas phase, respectively.

In Figure 6-2, the relative Raman cross-section and activation energy were adjusted to fit experimental observation in each temperature case and their values are summarized in Table 6-1.

Table 6-1. Values of apparent relative Raman cross-section of ammonia and activation energy for concentration and reaction rate calculations, respectively.

T (°C)	300	500	700	900
Σ_{NH_3}	4.05	3.77	3.39	2.95
E_S (kcal/mol)	10.9	12.6	14.5	15.8

The relative Raman cross-section should not change more than experimental error. The values of the relative Raman cross-section in Table 6-1, however, clearly show a decreasing trend with temperature. The temperatures used in these experiments are not high enough to cause any geometric changes in ammonia and electronic transitions considering its high vibration energy (3335 cm^{-1}). In Chapter 3, the apparent Raman cross-section of ammonia was observed to change with temperature from the flow cell experiments (Table 3-3). Therefore, it is considered that changes in optical properties of the reactor wall (i.e., quartz) are responsible for the observed trend in the relative Raman cross-section (Table 6-1) as explained Figure 3-6.

The activation energy values used in Figure 6-2 to reproduce experimental observations clearly show an increasing tendency as summarized in Table 6-1. The increase trend in activation energy with temperature is reasonable considering transition state theory ($E_a = \Delta H + mRT$, where m is the order of the reaction [Alb87]), even though actual mechanism is not simply described. It is, however, necessary to confirm that this observation was not an artifact due to the changes in optical properties of the reactor wall. The walls of the reactor were made of quartz and scattered signals pass one of the walls before reaching to the Raman spectrometer. Therefore, it is possible that apparent relative Raman cross-section was changed rapidly near the susceptor level due to variations of the transmittance of quartz cause by the corresponding rapid temperature change in the wall.

As light passes a quartz plate, the decrease in its intensity (**I**) is a function of reflection (α) and absorption (β) coefficients and thickness (l) of the plate as follows [Ing88]:

$$\mathbf{I} \propto \mathbf{I}^0 (1-\alpha)^2 \, e^{-\beta l} \qquad (6\text{-}6)$$

where superscript '0' denotes incident intensity of the light, i.e. before it encounters the plate. As discussed in Chapter 3, the optical properties depend on the wavelength of the light and temperature (see Figure 3-6). Therefore, it is needed to write Eq. 6-6 with respect to specific wavelengths or wave numbers, i.e. 2331 and 3335 cm^{-1} in this case.

$$\frac{\mathbf{I}_N^0}{\mathbf{I}_J^0} = \frac{\mathbf{I}_N}{\mathbf{I}_J} \left(\frac{1-\alpha_J}{1-\alpha_N} \right)^2 e^{(\beta_N - \beta_J) l} \qquad (6\text{-}7)$$

where 'J' and 'N' stand for ammonia (3335 cm^{-1}) and nitrogen (2331 cm^{-1}), respectively. Using Eq. 6-7, the original intensity ratio before scattered signals encounter the plate can now be calculated from the observed intensity ratio.

To evaluate the optical property term in Eq. 6-7 at the same set of points along the centerline of the reactor where temperature and concentration were measured, a well-known light source (W-lamp) was put at the same horizontal plane as the laser line was present outside the reactor. Therefore, radiation from the W-lamp was transmitted through two layers of quartz plates before detected by the spectrometer, while scattering signals were transmitted through one layer of quartz plate. In this configuration, an equation similar to Eq. 6-7 can be written for radiation from the W-lamp.

$$\frac{\mathbf{I}_{\mathrm{n}}^{0}}{\mathbf{I}_{\mathrm{j}}^{0}} = \frac{\mathbf{I}_{\mathrm{n}}}{\mathbf{I}_{\mathrm{j}}}\left(\frac{1-\alpha_{J}}{1-\alpha_{\mathrm{N}}}\right)^{4} \mathrm{e}^{2(\beta_{\mathrm{N}}-\beta_{J})l} \tag{6-8}$$

where lower case subscripts were used to denote the radiation originated from the W-lamp, while upper case subscripts were used in Eq. 6-7. If the intensities of the light of various wavelengths emitted from the W-lamp are measured before and after two layers of quartz plates of the measurement reactor, the optical property term in Eq. 6-8 or 6-7 can be determined.

$$\frac{\mathbf{I}_{\mathrm{N}}^{0}}{\mathbf{I}_{J}^{0}} = \frac{\mathbf{I}_{\mathrm{N}}}{\mathbf{I}_{J}}\sqrt{\frac{\mathbf{I}_{\mathrm{n}}^{0}/\mathbf{I}_{\mathrm{j}}^{0}}{\mathbf{I}_{\mathrm{n}}/\mathbf{I}_{\mathrm{j}}}} \tag{6-9}$$

As a test case, the term in square root in Eq. 6-9 was experimentally evaluated with the heater temperature set at 500 °C. The other conditions were the same as described in the experimental section except that pure nitrogen was used for all inlet flows. The transmission characteristic of the quartz plates of the reactor at a single observation point is shown in Figure 6-3. The transmission characteristic shown in Figure 6-3 is a function of temperature and wavelength of transmitted light. Transmission was observed to increase with temperature for the whole wavelength range and the degree of the increase was dependent on the wavelength. Therefore, depending on the wavelength, the square root term in Eq. 6-9 is expected to change differently. By measuring the transmission characteristic of the reactor walls along the centerline of the reactor, values of the square root term in Eq. 6-9 for observation points were evaluated and the results are presented in Figure 6-4.

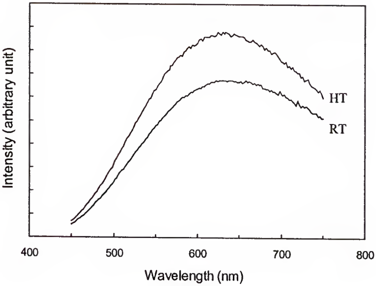

Figure 6-3. Transmission characteristic of the reactor walls for two temperatures: HT and RT stand for activated heater ($T_H = 500$ °C) and room temperature, respectively.

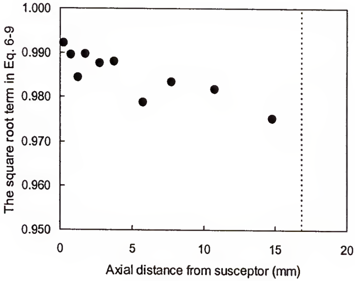

Figure 6-4. The square-root term in Eq. 6-9 evaluated by using a W-lamp. The heater temperature was set at 500 °C. The vertical dashed line denotes the position of the inlet tip.

The values in the figure range from 0.975 to 0.992 and the difference between these two is 0.017. For the NH_3/N_2 case, the uncertainty in the ammonia mole fraction due to this variation (δOP) can be estimated by analysis of the error propagation [Box78] as

$$(\delta x_{NH_3})^2 = (\delta OP)^2 x_{NH_3}^2 (1 - x_{NH_3})^2 / (OP)^2 . \qquad (6\text{-}10)$$

With $x_{NH_3} = 0.08$, $OP = (0.975+0.992)/2$, and $\delta OP = 0.0085$, the estimated uncertainty δx_{NH_3} is 6.36×10^{-4}. This uncertainty in the ammonia mole fraction is negligible compared with the observed variations near the susceptor in Figure 6-2. Therefore, changes in the optical properties of quartz due to the local temperature variation have little influence on the concentration behavior near the susceptor shown in Figure 6-2.

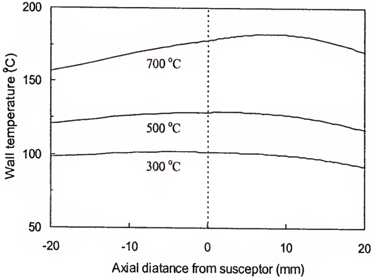

Figure 6-5. Simulated temperature distributions at the reactor wall for different heater temperature: 300, 500, and 700 °C.

The reactor model produced the temperature profiles along the centerline of the reactor given in Figure 6-2. Because the optical properties of quartz depend on the wall temperature, temperature profiles in the reactor wall were also extracted from the simulation results (Figure 6-5). The simulated wall temperature profiles are almost flat for 300 and 500 °C, and the temperature variation for 700 °C is less than 5 °C within 10 mm from the susceptor. This small temperature variation could not cause the large concentration variations within about 5 mm from the susceptor in Figure 6-2. This is consistent with the experimental observation shown in Figure 6-3. In Chapter 3, the apparent relative cross-section of NH_3 was evaluated at three temperatures using a quartz-wall flow cell. The value at 114 °C was 4.0, while the apparent relative Raman cross-section at the heater temperature of 300 °C in Table 6-1 is 4.05. The wall temperature curve for the same heater temperature in Figure 6-5 shows that the wall temperature ranges from 94 to 101 °C within 17 mm from the susceptor surface. Although two quartz materials for the flow cell and the current flow reactor are not the same, the reactor model describes the fundamental transport phenomena in the reactor well.

It should also be considered that unexpected phenomena such as a flow instability could cause the observed concentration variations in Figure 6-2. To check this possibility, one more experiment was conducted with the heat temperature at 500 °C. In this case, the sweep flow was stopped and other experimental conditions were the same as described in the experimental section. The gas temperature and ammonia concentration were measured and depicted in Figure 6-6. It is observed from the measured concentration profile in Figure 6-6 that the ammonia concentration along the centerline of the reactor is initially low near the inlet tip due to the fresh N_2 flow through the center channel and increases as the gas flows toward the susceptor. Finally, the concentration decreases near the susceptor surface. In this experiment, the sweep flow was turned off. This unmatched velocity condition should cause a poor prediction [Hwa04]: the concentration rise above the simulated concentration in the range from 5 to 10 mm. If no reactions had occurred on the susceptor surface, the ammonia concentration would not decrease near the susceptor, contrary to the observation in Figure 6-6, as ammonia diffusion should always occur toward the centerline of the reactor from its higher concentration surroundings. Furthermore, as shown by the horizontal dashed line in the figure, the mixing-cup concentration of ammonia in the reactor is higher than the highest concentration observed along the centerline of the reactor. Therefore, it is considered that ammonia disappeared upon adsorption at the susceptor surface.

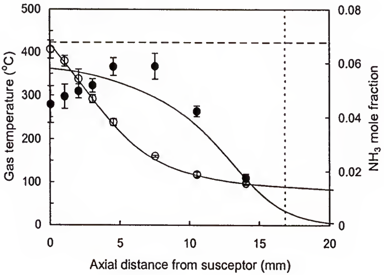

Figure 6-6. Ammonia concentration (●) and gas temperature (O) profiles along the centerline of the reactor with the heater temperature set at 500 °C. The horizontal dashed line denotes mixing-cup concentration in the reactor.

6.1.4 Conclusions

It was observed that ammonia reacts at the quartz susceptor surface when the heater temperature was set at 300, 500, 700, and 900 °C. The values of the activation energy for a simple reaction model were estimated at the heater temperatures. It should be noted that the transmission characteristic of quartz depends on wavelength of the light and quartz temperature. The wavelength dependency of transmittance is not linear and therefore careful attention should be paid in using Raman spectroscopy to probe processes in a quartz reactor. The wall temperature and apparent relative Raman cross-section relation observed for the heater temperature of 300 °C additionally supports the reactor model.

6.2 Behavior of Trimethylaluminum

6.2.1 Background

Group III-nitride semiconductor materials have promising properties for short wavelength optoelectronic applications, such as light emitters and detectors [Mor97, Nak97] as well as high temperature and high power applications. Especially, ultraviolet (UV) light sources can be used in optical storage devices and light sources for producing light of a desired wavelength [Nis01a, Nis01b]. UV light is obtainable using AlN or AlGaN semiconductor films and TMAl is the most common metalorganic precursor for aluminum.

It has been reported [Smi72] that TMAl is present in the dimer form at room temperature and the dimer dissociates at elevated temperature. The molecular geometry of TMAl and its dimer was determined using gas phase electron diffraction [Alm71] and later *ab inito* calculations were performed to estimate the dissociation energy [Hir94]. The vibration characteristics of TMAl and its dimer were investigated using Raman [Obr71, San92] and infrared (IR) spectroscopies [Ati91].

In the following, behavior of TMAl in a flow reactor is investigated using *in situ* Raman spectroscopy, including mass dispersion and dissociation of the dimer.

6.2.2 Experimental

The reactor configuration in Figure 6-1 was used with the modification that the height of the free space in the annulus channel after the packing was changed to 8.5 mm.

Nitrogen was introduced into the reactor through three inlets at 21 °C. The gas velocity was set at 2.5 cm/s for all inlets. The gas flow to the center inlet was allowed to pass through a TMAl bubbler kept at 17.1 °C before directed into the reactor. The vapor pressure of $(TMAl)_2$ was estimated using Eq. 6-11 [Smi72]:

$$P\,[\text{mmHg}] = \exp(19.0239 - 4929.8/T) \tag{6-11}$$

where T stands for temperature in Kelvin. This equation was obtained from experiments between 17.6 and 47.7 °C. At 17.1 °C, the $(TMAl)_2$ concentration at the center flow channel was calculated to be 1.0 % in the current experiment. A dispersion experiment was conducted without the heater activated and then dissociation behavior of the dimer was observed with the heater temperature set at 300 °C. Raman scattering signals were recorded along the centerline of the reactor with the 514 nm line of an argon ion laser.

6.2.3 Results

Characteristic peaks of $(TMAl)_2$ were observed as shown in Figure 6-7. The identification of these peaks was reported previously [San92]. There are two kinds of CH_3 in $(TMAl)_2$: pendant and bridge positions. Therefore, two Al-C vibrations (448 cm^{-1} and 592 cm^{-1}) and two C-H vibration (2835 and 2900 cm^{-1}) were observed.

Among these peaks, the intensity change of the peak at 592 cm^{-1} was followed along the centerline of the reactor and concentrations were extracted using Eqs. 3-24 and 3-25. The results are presented in Figure 6-8. Two different symbols in the figure designate different sets of experiments.

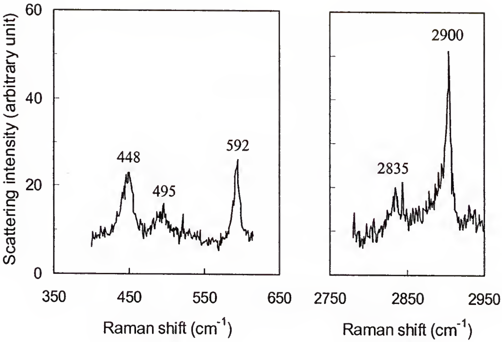

Figure 6-7. Observed Raman peaks for $(TMAl)_2$ at 21 °C.

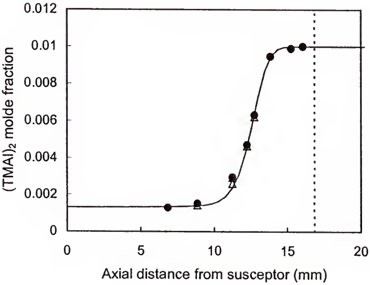

Figure 6-8. Measured and simulated $(TMAl)_2$ concentration profiles at 21 °C. The two different symbols designate repeated experiments. The vertical dashed line denotes the inlet tip position.

The relative Raman cross-section of 7.2 for the vibration of 592 cm^{-1} produced a good fit as shown in Figure 6-8. In the simulation, properties of the dimer were estimated using the Lennard-Jones potential parameters: $\sigma = 6.83$ and $\varepsilon/k_B = 465.9$ K [Hol92]. A reported Raman cross-section [San92] is 8.0×10^{-30} cm^2/sr with a 488 nm line, and this gave a relative Raman cross-section of 9.6. This difference between two values of the relative cross-section can be attributed to errors in temperature control of the thermal bath, saturation of $(TMAl)_2$ during bubbling, integration of peaks, etc. It is not easy to determine the Raman cross-section. For example, reported values of the relative Raman cross-section of CH_4 range from 6.8 to 9.5 [Sch79].

The molecular weight of the dimer is 144.18 and that of the carrier gas, i.e. N_2, is 28.02. Therefore, natural convection due to solutal density difference is expected. This type of natural convection was investigated in Chapter 4. The concentration profiles in Figure 6-8 show a rapid drop of concentration in the range from 10 to 15 mm due to the natural convection and the concentration was low after that drop. To keep concentration high, the natural convection should be suppressed.

The natural convection due to solutal density difference can be mitigated by heating the susceptor in the current inverted geometry of the measurement reactor, because the density variation with temperature is larger for higher molecular weight species. To test the effects of heat application, axial velocity profiles along the centerline of the reactor were simulated using the 2-D reactor model without reaction for three cases of heater temperatures: room temperature, 100, and 200 °C and the results are shown in Figure 6-9. The axial velocity component shows that there is strong recirculation characterized by the negative velocities inside the reactor at room temperature and the recirculation diminishes at higher temperature. This tendency is explained by considering thermal effects on density variation for different molecular weight cases. Therefore, by adjusting the heater temperature, the natural convection caused by molecular weight difference can be reduced to some degree.

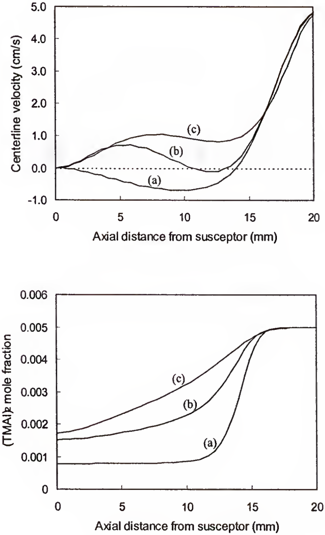

Figure 6-9. Axial velocity component and $(TMAl)_2$ mole fraction along the centerline of the reactor for three heater temperature cases: (a) room temperature, (b) 100, and (c) 200 °C.

With the heater activated ($T_H = 300$ °C), the dissociation of $(TMAl)_2$ into TMAl was studied in the current CVD reactor. The Al-C vibrations at 592 and 530 cm^{-1} [Obr71] for $(TMAl)_2$ and TMAl, respectively, were used to follow the dissociation. The results in Figure 6-10 show that the dimer dissociated as the gas flow approached the heated susceptor and finally the monomer became dominant at 135 °C in the up flow CVD reactor.

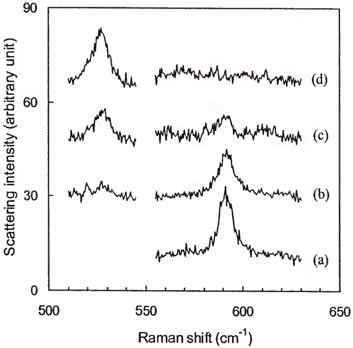

Figure 6-10. Dissociation behavior of $(TMAl)_2$ into TMAl at various temperature position along the centerline of the reactor: (a) 44, (b) 51, (c) 97, and (d) 135 °C.

By controlling thermal conditions, it is possible to have predominantly monomer and thus simplify the involved chemical processes. During the experiment, the optical path for Raman detection became blocked by deposition, considered to be Al_2O_3, and further investigation was aborted.

6.2.4 Summary

Characteristic peaks of $(TMAl)_2$ and TMAl were identified and the relative Raman cross-section of the dimer was estimated to be 7.2. The dispersion of the dimer in the stagnation flow reactor was measured by recording intensities of the peak at 592 cm^{-1} along the centerline of the reactor. It was considered that the natural convection caused by solutal density difference could be reduced by adjusting thermal conditions such as heater temperature in the inverted reactor geometry. In addition, it was shown that $(TMAl)_2$ could dissociate quickly in the flow reactor and therefore chemical processes can be simplified by dissociating the dimer into monomers with proper reactor geometry and thermal boundary conditions.

CHAPTER 7
DECOMPOSITION OF TRIMETHYLINDIUM

7.1 Introduction

MOCVD is a widely used technique to grow device quality epitaxial films of compound semiconductors [Kol98]. In particular, MOCVD is commonly used in the growth of In-containing group III-V materials for a variety of electronic and optoelectronic device applications. For example, alloys of indium with the direct wide bandgap semiconductor GaN are finding broad application as visible light emitters [Muk98, Nak99, Shr00]. The design of MOCVD reactors and identification of optimal operating conditions generally involve considerable experimentation and thus the development time for a new reactor or a process for a specific device application can be long. Furthermore, the operating conditions to optimize a specific film property such as background carrier concentration, thickness uniformity, or dislocation density are generally different for each property. Thus a realistic process model would be useful for optimizing a reactor design and establishing sensible operating conditions for a specific device application. Although advances in computational capacity and the estimation of transport properties have permitted the construction of reasonable flow models, the development of a realistic reactor model is limited by uncertainties in the reaction mechanisms and values of their corresponding reaction rate constants.

TMIn is the most commonly used precursor for depositing In-containing compound semiconductors and its pyrolysis has been previously investigated. The homogeneous decomposition of TMIn was first investigated by Jacko and Price [Jac64] using toluene as a carrier gas at low pressure. The results of this study suggested TMIn homogeneously decomposes by sequential homolytic fission of the In-C bond to yield methyl radicals, with elimination of the second methyl radical occurring rapidly. Subsequent studies used flow tube reactors and physical sampling of the reacting gas mixture to investigate the influence of the choice of carrier gas on the extent of decomposition [Buc88, But86, Lar86]. The value of the rate constant of the apparent 1st order decomposition reaction suggested by analysis of these measurements, however, varied by almost 2 orders of magnitude with the reported activation energy ranging from 35.9 to 54.0 kcal/mol. These variations possibly reflect chemical effects from the choice of carrier gas [But86, Jac64, Lar86] as well as experimental uncertainties. Consistent with the decomposition mechanism originally proposed by Jacko and Price, more recent experiments report the direct observation by *in situ* Raman spectroscopy of monomethylindium (MMIn) and atomic indium in the gas phase of a cold-wall CVD reactor [Par02b].

Kinetic data on the decomposition of metalorganic precursors are often obtained using a simple flow cell or flow tube experiment [Maz89, Syw91a, Tho96]. Establishing homogeneous reaction conditions, minimizing the influence of the sampling probe, and identifying reaction intermediates, however, can complicate the data analysis. Another approach to better understand the growth chemistry is to use a detailed reactor model to directly analyze data from MOCVD growth runs. Although several investigators have taken this approach [Mou91, Oh91, Pes98], modeling deposition reactors is complex (e.g., complicated view factors, time dependent surface reactivity and emissivity, moving susceptors, flow instabilities). Furthermore, spatial variation of the film composition and thickness as a function of deposition conditions are often the only experimental data available to validate the model or estimate parameters [Saf97]. These limitations and mass transfer effects often limit the ability of a model to distinguish reaction pathways and estimate reaction rate constants. For these reasons, several researchers have effectively used optical probes such as Raman scattering, IR absorption, laser induced fluorescence (LIF), and coherent anti-Stokes Raman scattering (CARS) [Ric91] to detect reaction species, and often quantify their concentration and establish the local temperature. As an example, the study of the decomposition of phospine (PH_3) by several analysis methods [Abr91, Lar87, Luc88] revealed that *in situ* probing is necessary to follow the process with sufficient accuracy to obtain quantitative results. Optical probes are thus well suited to probe the reactive boundary layer above a heated susceptor in a MOCVD reactor.

Physical properties of species in the reactor constitute an important part of a realistic MOCVD reactor model, while those of metalorganic precursors and their reaction derivatives are hardly available. In most cases, they are estimated from the Chapman-Enskog theory using simple interaction potentials as explained in Chapter 2. Thermodynamic properties are, however, not correctly estimated from that theory, because simple interaction potentials cannot account rotational and vibrational states of polyatomic molecules. It is known that those energy states are reasonably described using quantum chemistry concepts as explained in Chapter 3. Therefore, a few physical properties such as heat capacity and thermal conductivity could be estimated using those concepts and results of traditional kinetic theory [Bir60]. In addition, this fundamental approach to evaluate properties of chemical species is able to help understand reaction kinetics and mechanism by providing thermodynamic properties of reaction intermediates.

When Group III precursors and ammonia are mixed they can react to form a Lewis acid-base complex. Adduct structures have been reported for aluminum [Mül99], gallium [Alm92b], and indium [Pio99] cases. Since the vapor pressure of the adduct species is much less than its parent $M(CH_3)_3$ precursor, condensation can remove reactant from the process and lower precursor efficiency. Furthermore, thermal diffusion of the larger adducts can further reduce process efficiency. This problem has been mitigated with advances in reactor design and process optimization [Che96, Mih98], even for TMAl [Guo02]. It has been suggested for TMGa and NH_3 that adducts can further react to form ring-shape trimers, yielding methane. This reaction was first confirmed with low temperature experiments [Alm92b, Ama92] and it was suggested that the trimer is a major component [Tho96]. Several mass spectroscopic results [Guo02, Mih98], however, contradict this suggestion and recent quantum chemical calculations [Sne03] predict that the original adduct plays an important role in the growth process than oligomers of the adduct. It was observed [Syw91b] with IR spectroscopy that the adduct dissociated into TMGa and NH_3 at elevated temperatures. For TMIn and NH_3, formation of the adduct was reported by observing shifts in ν(N-H) and $\rho(CH_3)$ using infrared matrix isolation technique [Pio99]. It is considered that the adduct of TMIn and NH_3 dissociates more easily.

In this chapter, decomposition of TMIn is investigated using *in situ* Raman spectroscopy, computation chemistry, and the parameter estimation procedure developed in Chapter 5. In addition, interaction between TMIn and NH_3 is studied.

7.2 Kinetics of TMIn Decomposition

The reactor model developed in Chapter 2 was combined with a genetic algorithm described in Chapter 5 to study the pyrolysis of TMIn in a cold-wall CVD reactor using nitrogen as the carrier gas and extract physical parameters from measured temperature and TMIn concentration profiles.

7.2.1 Experimental

A custom CVD reactor (Figure 7-1) was designed and constructed for the purpose of interfacing it to a laser radiation source and the collection optics of a high-resolution spectrometer.

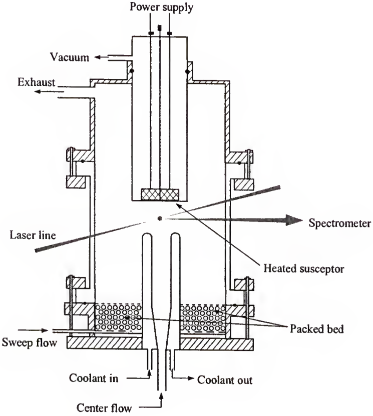

Figure 7-1. Schematic of the reactor.

To reduce recirculation flows, the reactor was oriented with the gas flow opposite that of gravity and towards a heated susceptor. In the decomposition experiments, the gases were introduced through two concentric inlets located at the bottom of the reactor. The reactant mixture entered through the center inlet, with an adjustable separation distance from the susceptor. A hot-water jacket surrounding the center inlet was incorporated in the reactor to control the inlet temperature. A second stream of only carrier gas (sweep), with gas velocity matched to that of the reactant gas stream at the center inlet, was fed to the outer inlet to prevent deposition on the quartz reactor wall. The whole reactor was surrounded by a rectangular enclosure constructed of optically pure quartz flats. The laser radiation and scattered light passed through these optical flats and through a small vertical slit in the cylindrical reactor wall. A quartz envelope containing a resistance heating-element served as the susceptor. The entire reactor system was mounted on an x-y-z translation stage to allow positioning the reactor relative to the laser focal point. A Raman spectrometer (Ramanor U-1000, Jobin-Yvon) was used to collect scattered light along the centerline of the reactor from the 488 nm line of an argon ion laser. The system has been described elsewhere in more detail [Hua93].

The base operating conditions for the TMIn pyrolysis studies consisted of a heating element control temperature of 850 °C and gas velocities for the reactant and sweep flows of 2.0 cm/s. TMIn was conveyed from a bubbler to the center inlet by nitrogen carrier gas at a sufficiently low flow rate to ensure saturation. The bubbler temperature was set at 42 °C, corresponding to a TMIn concentration of 1.17 mole % at the center inlet. The water jacket temperature was maintained at 95 °C. The temperature distribution within the reactor was determined by analysis of the rotation bands of the nitrogen carrier gas

[Mon88, Par02a] with an accuracy of less than 20 °C. The characteristic peaks of TMIn and its derivatives, MMIn and atomic indium (In), were traced to follow the pyrolysis process. These peaks are located at 476, 430, and 2215 cm^{-1} for TMIn, MMIn, and In, respectively [Par02b]. In a typical experiment, the susceptor was heated under carrier gas flow, followed by initiation of the reactant gas flow. After steady state had been reached, Raman spectra were collected along the reactor centerline as a function of distance from the susceptor.

7.2.2 Numerical Description

With the combination of a validated reactor model and an optimization procedure, measured temperature and Raman intensities for the decomposition of TMIn in N_2 were evaluated to estimate the Raman cross-section of TMIn and the rate constants for the removal of the first methyl group. The estimation was performed by minimizing the objective function that is the sum of squares of the differences between observed and model-predicted ($\hat{f}_i$) quantities for the total of 'm' observations:

$$S(\mathbf{k}) = \sum_{i=1}^{m}\left(\left\{1+\left(\frac{\tilde{\nu}_0-\tilde{\nu}_j}{\tilde{\nu}_0-\tilde{\nu}_Q}\right)^4 \frac{1-\exp(-hc\tilde{\nu}_Q/k_B T_i)}{1-\exp(-hc\tilde{\nu}_j/k_B T_i)}\left(\frac{\mathbf{I}_Q}{\mathbf{I}_j}\right)_i \Sigma_j\right\}^{-1} - \hat{f}_i(k_0, E_a)\right)^2 \qquad (7\text{-}1)$$

where $\tilde{\nu}$, h, c, k_B, T, $\mathbf{I}$, and Σ_j represent wavenumber, Planck constant ($= 6.626\times10^{-34}$ Js), speed of light ($= 2.998\times10^{8}$ m/s), Boltzmann constant ($= 1.381\times10^{-23}$ J/K), thermodynamic temperature, scattering intensity, and the relative Raman cross-section of species j, respectively. Subscripts 0, j, and Q denote the incident light, species j, and nitrogen Q branch, respectively. Among these quantities, scattering intensity and temperature are measured experimentally. $\mathbf{k}$ is the parameter vector to be estimated and consists of the Raman cross-section and reaction rate constants (k_0 and E_a).

Since local optima were anticipated, a genetic algorithm was selected for parameter estimation purposes, which was followed by a Simplex algorithm to expedite fine-tuning of the parameter estimates (a simple genetic algorithm was implemented and a parameter estimation procedure was established in Chapter 5). The simple genetic algorithm was modified to include the crowding concept [Gol89]. To give the model-prediction ($\hat{f}_i$) in Eq. 7-1, a two-dimensional, axisymmetric model describing the momentum, heat, and mass transport has been developed to quantitatively interpret the experimental data. The steady state model incorporated temperature dependent thermophysical properties and gray body radiation heat transfer from the susceptor, neglected the viscous heating term in the energy equation, and was formulated with the Penalty Finite Element approach. A more complete description of the model and its validation are given in Chapters 2 and 4.

7.2.3 Results and Discussion

A gas temperature profile was measured along the centerline of the reactor, flowing pure N_2. Heat transport characteristic of an inverted, cold-wall, stagnation flow reactor was previously investigated in detail [Par02a]. The experimental temperature profile is compared with the fitted result in Figure 7-2. It is evident that the heat transport model reproduced the experimental result very well. Using this heat transport characteristic, the decomposition of TMIn was studied. It was previously reported [Par02b] that TMIn and its decomposition products (MMIn and atomic indium) were detectable by examining the vibrational spectra for the organoindium species and the electronic states for atomic indium. Raman intensities of TMIn, MMIn, and atomic indium measured along the centerline of the reactor are presented in Table 7-1.

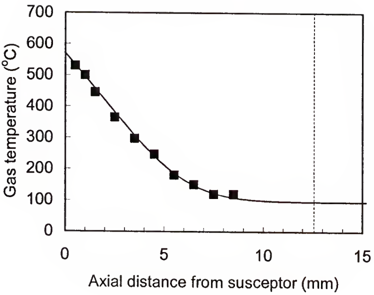

Figure 7-2. Experimental (■) and simulated (—) gas temperature profiles. The vertical dashed line denotes the tip position of the center inlet.

Table 7-1. Normalized relative Raman intensities of TMIn, MMIn, and atomic indium.

z (mm)	TMIn	MMIn	Indium
0.5	0	0.136	0.710
0.8	0.017	0.236	0.707
1.4	0.081	0.316	0.588
1.7	0.099	0.337	0.580
2.0	0.146	0.317	0.553
3.0	0.261	0.141	0.316
5.0	0.408	0	0
5.5	0.433	0	0
6.5	0.438	0	0
7.5	0.442	0	0

The intensities in Table 7-1 were normalized with that of nitrogen vibration ($2331\ cm^{-1}$) at each observation point (z) to provide the intensity ratio in Eq. 7-1. To quantitatively relate the scattering intensities in the table to concentrations, and thus estimate the rate constants for TMIn pyrolysis, a value of the cross-section must be established. Although its gas phase spectrum has been observed and interpreted [Hua93], the Raman cross-section of TMIn has not reported yet. In the approach proposed here, the Raman cross-section of TMIn and the rate constants for its pyrolysis are simultaneously estimated by minimizing Eq. 7-1.

It is well established [Jac64] that the decomposition of TMIn basically proceeds through sequential homolytic fission of the In-C bond to release methyl groups according to:

$$In(CH_3)_3 \rightarrow In(CH_3)_2 + CH_3 \tag{7-2a}$$

$$In(CH_3)_2 \rightarrow In(CH_3) + CH_3 \tag{7-2b}$$

$$In(CH_3) \rightarrow In + CH_3 \tag{7-2c}$$

It was reported [Buc88] that methyl radical attack on TMIn had little contribution to the disappearance of TMIn in He carrier. Since TMIn was dilute in inert N_2 carrier in the current study, it was assumed that the rate of disappearance of TMIn is dominated by Reaction (7-2a) and thus the decomposition was modeled as a pseudo first-order reaction. The frequency factor (k_0) and activation energy (E_a) of the rate constant and the Raman cross-section of TMIn were then estimated from experimental Raman intensities (Table 7-1). The rate equation was reparameterized to reduce the correlation between frequency factor and activation energy [Dra81, Mez67] according to:

$$k = k_0\, e^{-E_a/RT} \quad \rightarrow \quad k = \exp\left[p_1 - \frac{10p_2}{R}\left(\frac{1}{T} - \frac{1}{T_m}\right)\right] \qquad (7\text{-}3)$$

where $p_1 = \ln(k_0) - E_a/RT_m$ and $p_2 = E_a/10$. T_m is the mean temperature of measurement and was set at 337 °C in this analysis. Previously reported values of the activation energy are in the range 35.9 to 54.0 kcal/mol and those of the frequency factors are in the rage $10^{12.6}$ to $10^{17.9}$ [Buc88, But86, Jac64, Lar86]. Based on comparison with data for other molecules and published rate data, the activation energy was initially searched from 20 to 60 kcal/mol, the relative Raman cross-section from 20 to 25, and parameter p_1 from -18 to 14. A preliminary result (Figure 7-3) with this search space revealed that there exists a strong correlation between p_1 and p_2.

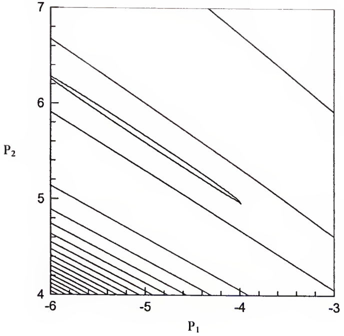

Figure 7-3. Exhaustive scan with the parameters defined in Eq. 7-3.

To reduce the correlation shown in Figure 7-3, the p_1 and p_2 axes were rotated by -32° to reduce the correlation. The new parameters were formulated using the following relations:

$$\begin{aligned}\phi_1 &= \quad p_1\cos\alpha + p_2\sin\alpha \\ \phi_2 &= -p_1\sin\alpha + p_2\cos\alpha\end{aligned} \tag{7-4}$$

where $\alpha = -32°$.

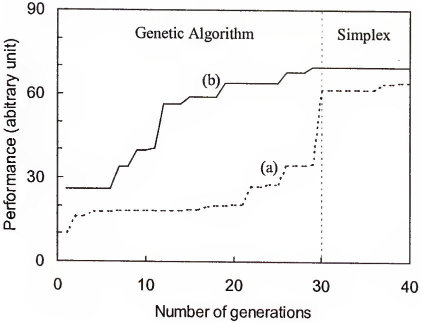

Figure 7-4. Performance of genetic/Simplex approach: (a) a simple genetic algorithm is used and (b) the crowding concept is added.

Performance of the sequential genetic/Simplex approach is depicted in Figure 7-4. The simple genetic algorithm developed in Chapter 5 gives Figure 7-4a, while a modified genetic algorithm with the crowding model concept [Gol89] gives Figure 7-4b. In the modified case (Figure 7-4b), the genetic algorithm alone showed good performance and no improvement was achieved by the sequential approach. The figure shows that the current minimization problem does not have a single optimum point as expected. After applying the Simplex algorithm repeatedly on the results in Figure 7-4a, three estimated parameters were: $\phi_1 = -7.1981$, $\phi_2 = 2.1205$, and $\Sigma_{TMIn} = 22.3$, which render $k_0 = 10^{17.9}\ s^{-1}$, $E_a = 56.1$ kcal/mol, and $\Sigma_{TMIn} = 22.3$. The relative cross-section of TMIn was estimated as 23.3 for the first time in this study.

With 95 % confidence, confidence intervals for the estimates were respectively evaluated as $10.6\times10^{17}\ s^{-1}$, 1.6 kcal/mol, and 0.2 by calculating the gradients numerically [Hwa04] and these uncertainty values for the rate constants are comparable with reported uncertainty values in TMIn decomposition [Oik88]. The magnitude of correlation [Mil86] between k_0 and E_a is 0.98, while those between the relative Raman cross-section and rate constant are in the range 0.39 to 0.45. To see the effects of the reparameterization given in Eq. 7-4, an exhausted scan was performed around the estimates with a fixed Raman cross-section ($\Sigma_{TMIn} = 22.3$).

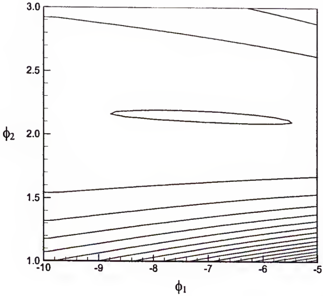

Figure 7-5. Exhausted scan with a fixed relative Raman cross-section ($\Sigma_{TMIn} = 22.3$).

Figure 7-5 shows that the correlation between the frequency factor and activation energy was nearly removed after the reparameterization.

With the estimated parameters, the reactor model reproduced a good fit to the measured TMIn concentration profile (Figure 7-6a). The dotted line represents temperature profile in the reactor. To better determine the onset of TMIn decomposition, a TMIn concentration profile was calculated assuming only gas phase dispersion of TMIn in N_2 (i.e. no gas phase reaction).

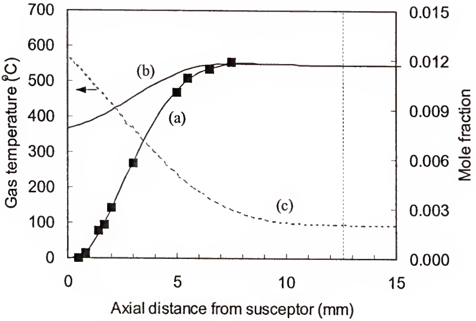

Figure 7-6. Experimental (■) and simulated concentration profiles of TMIn along the centerline of the reactor: simulated profiles with (a) and without (b) the decomposition reaction. Gas temperature profile (c) and the inlet position (---) are also presented.

Comparing the dispersion only profile (Figure 7-6b) with the reaction case (Figure 7-6a), it is noticed that the gas phase reaction started at about 120 °C. The temperature range over which TMIn was observed to decompose is in the approximate range 120 to 535 °C, which is wider than reported in the previous studies [Buc88, But86, Jac64, Lar86]. In particular, the onset temperature observed in this study is considerably lower than the one reported earlier (340 °C) using the same carrier gas in a flow tube arrangement [Lar86]. In addition, 430 °C was the highest temperature in the previous study [Lar86]. The difference in observed decomposition temperatures likely comes from differences in residence times and thermal profiles between the experimental methods, as well as differences in probing methods. The signs of these differences are reasonable when it is considered that the residence time of TMIn in the thermal boundary layer is shorter than that in the flow tube reactor, while the residence time in the lower temperature entrance is longer for the current apparatus than the flow tube. For the effect of probing methods, it was reported [Abr91, Lar87, Lüc88] that the decomposition of phospine was observed to start at a lower temperature with *in situ* probing than with *ex situ* probing, presumably due to continued chemical changes during the sample transfer step. In the current study, all of the information about the reaction was obtained with non-disturbing, *in situ* Raman spectroscopy and influences of the probing method on experimental data were consequently minimized.

The reactor design and operating condition, *in situ* diagnostics, and probe sensitivity allowed the reaction to be followed over a wider temperature range than ever, as illustrated in Figure 7-7. This figure compares the first order rates from different measurements over their temperature range of measurement, while values of the rate constants are summarized in Table 7-2. The present results render similar rates as in the N_2 carrier gas case in Lar86, while values of the rate constants are quite different. This observation reveals that the frequency factor and activation energy in the Arrhenius-type rate equation are correlated with each other and therefore it is not easy to determine rate constant from experimental data. As shown in Figure 7-5, the correlation between the two parameters was nearly removed in this study, using reparameterization.

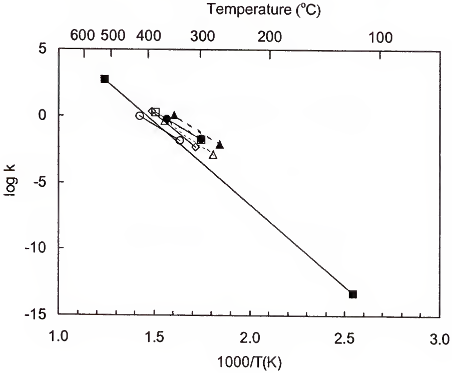

Figure 7-7. Reported reaction rates for TMIn decomposition with different carrier gases: (○) N_2 [Lar86], (◇) He [Buc88], (□) D_2 [Buc88], (●) H_2 [Lar86], (▲) H_2 [Buc88], (△) Toluene [Jac64] carrier cases, and (■) N_2 in the present study.

It is noticed from Table 7-2 that the previous experimental results are not consistent for the same carrier gas, as shown in hydrogen cases. In addition, chemical effects of carrier gases are not clearly observed as toluene and helium carrier cases are compared. These discrepancies imply that kinetic studies of metalorganic sources are easily influenced by experimental conditions. For example, as pointed out by McDaniel and Allendorf [Mcd00], the decomposition of TMIn can be under the influence of heterogeneous reactions on the reactor surface in flow tube investigations and apparent homogeneous rates could be higher than real reaction rates. For an inverted, cold-wall, stagnation flow reactor, a verified mass transport model showed that reactants could be isolated in the gas phase from the reactor surfaces (Figure 4-19). In addition, TMIn decomposition was completed in the gas phase (Figure 7-6). Therefore, the decomposition seemed to be homogeneous and influences of the reactor walls on the decomposition of TMIn were minimized in this study. This observation supports that the present results give a lower bound of the reported TMIn decomposition rates in Figure 7-7.

Table 7-2. Present and reported reaction rate constants for TMIn decomposition

	k_0 (s^{-1})	E_a (kcal/mol)	Carrier
Present	$10^{17.9}$	56.1	N_2
Jacko & Price [5]	$10^{15.7}$	47.2	Toluene
Larsen & Stringfellow [6]	$10^{12.6}$	40.5	N_2
	$10^{12.0}$	35.9	H_2
Buchan et at. [8]	$10^{17.9}$	54.0	He
	$10^{13.4}$	39.8	D_2
	$10^{15.0}$	42.6	H_2

The decomposition of MMIn (Reaction 7-2b) is considered in the following. Using the current reactor model, MMIn concentration profiles were calculated with the homogeneous decomposition of MMIn by Jacko and Price [Jac64] and heterogeneous decomposition of MMIn. The surface reaction rate (k_S) was estimated from kinetic theory as follows [Mou91, Saf97]:

$$k_S = \sqrt{\frac{RT}{2\pi M}}\, e^{-E_S/RT} \qquad (7\text{-}5)$$

where R, T, M, and E_S are respectively gas constant, temperature, molecular weight of MMIn, and activation energy for the surface reaction. Three values of the activation energy for the surface decomposition were used: 10, 15, and 20 kcal/mol.

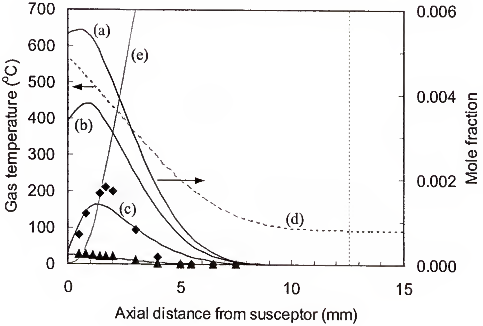

Figure 7-8. Experimental (◆) and calculated MMIn concentration profiles with three values of the activation energy for surface decomposition: (a) 20, (b) 15, and (c) 10 kcal/mol. Atomic indium concentration profile (▲) is shown and (d) gas temperature (e) TMIn concentration profiles are also presented.

The results (Figure 7-8) show that heterogeneous decomposition of MMIn is appreciable and the sequential decomposition mechanism by Jacko and Price [Jac64] does not give as good a fit as in the TMIn decomposition. Case (c) in the figure gives a good description of the slope of the experimental concentration profile near the surface, while it is not good on the other side of the acme of the experimental profile. The mechanism shown in Case (c) overestimates MMIn concentration in the low temperature region (> 3 mm) and underestimates in the high temperature region (1 ~ 3 mm). This observation can be explained by assuming a storage mechanism of MMIn and/or dimethylindium (DMIn): for example, these species hide from Raman detection in the low temperature region by forming some complexes, while the complexes release MMIn or DMIn to increase MMIn concentration in the high temperature region. This proposition, however, needs more experimental and/or theoretical studies, since no possible complex has been identified or reported yet.

The experimental concentrations of MMIn in Figure 7-8 were obtained from their Raman intensities using a value of relative Raman cross-section ($\Sigma_{MMIn} \approx 80$). Although this analysis could not be completed due to insufficient information, this value of relative Raman cross-section is several times larger than that of TMIn or other metalorganic sources. It was reported [Par02b] that MMIn was observed due to resonance Raman effects when wavelength of the laser line was shorter than 514 nm for an argon ion laser. If experimental conditions did not allow resonance Raman effects, MMIn would not be observed. Similarly, atomic indium seems to have a large relative Raman cross-section ($\Sigma_{In} \approx 3000$) due to the involved electronic transitions [Par02b]. Therefore, it is considered that experimental setup or conditions play important roles in detecting reaction intermediates.

7.2.4 Conclusions

The pyrolysis of TMIn was studied in an upflow, cold-wall, stagnation-point-flow reactor with *in situ* Raman spectroscopy. To analyze the experimental data and estimate reaction rate constants, a parameter estimation procedure based on a genetic/Simplex algorithm sequence was used. As a result of the estimation procedure, the reaction rate constants of the pyrolysis were estimated: the frequency factor and activation energy were $10^{17.9}$ s^{-1} and 56.1 kcal/mol, respectively. Pyrolysis of TMIn occurred and completed in the gas phase between 120 and 535 °C, while a previous study with the same carrier gas (nitrogen) reported a range between 340 and 430 °C. The decomposition of MMIn was, however, found to occur on the susceptor surface as well as in the gas phase. It was revealed for decomposition of metalorganic sources that experimental observations were easily influenced by the probing method and process conditions.

7.3 Reaction Intermediates

A number of studies have been conducted about TMIn decomposition, since a simple sequential hemolytic fission of the In-C bond was proposed by Jacko and Price [Jac64]. Reaction mechanisms suggested in most of those studies are based on the analysis of hydrocarbon byproducts (CH_4 and C_2H_6) and/or indium containing fragments (DMIn, MMIn, and In) using mass spectroscopy [Buc88, Jac64, Mcd00]. Recently, MMIn and atomic indium were observed in the gas phase using *in situ* Raman spectroscopy without any sampling mechanism involved [Par02b]. In this section, new reaction intermediates are suggested with experimental evidence and computational chemistry supports.

7.3.1 Experimental

An up flow cold-wall CVD reactor shown in Figure 7-9 was interfaced with a high resolution Raman spectrometer to establish *in situ* observation of TMIn decomposition. The reactor configuration was modified from the setup in Figure 5-5 based on mass transport study results discussed in Chapter 4: the annulus channel was filled with glass beads and the remaining free space was 6 mm in height. The entire reactor system was put on a 2-D stage to allow spatial scan with respect to a spatially fixed laser line for *in situ* probing.

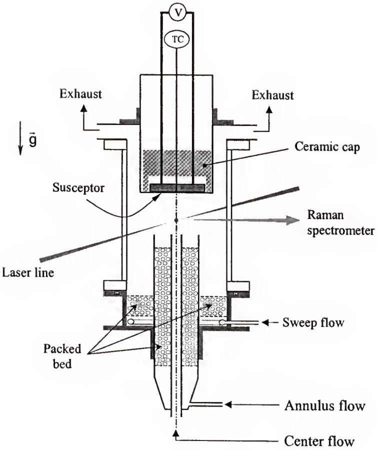

Figure 7-9. Schematic of the reactor for the reaction intermediate study.

Nitrogen was introduced to the reactor through three inlet channels at a nominal gas velocity of 2.5 cm/s. Part of the N_2 stream to the center inlet was allowed to pass through a TMIn bubbler at 36 °C and final TMIn concentration in the center channel was 0.48 %. The gas flows were directed to the heated susceptor. The heater temperature was set at 690 °C and thus TMIn in the gas stream would decompose as it flowed toward the susceptor. The 488 nm line of an argon ion laser (Inova-90, Coherent Lasers) was focused on a desired spatial point and the scattering signals from the point were collected with a Raman spectrometer (Ramanor U-1000, Jobin-Yvon). It has been reported that the vibrational Raman shifts of the In-C bond in TMIn and MMIn were observed respectively at 476 and 430 cm^{-1} [Par02b] and the electronic Raman shift of atomic indium ($5P_{3/2} \leftarrow 5P_{1/2}$) was at 2215 cm^{-1} [Tak81]. Decomposition behavior of TMIn was monitored along the centerline of the reactor with this information.

7.3.2 Computational Chemistry

The model chemistry used in this study was selected based on thermodynamic potential calculation results for the release of the first methyl group from TMIn:

$$In(CH_3)_3 \rightarrow In(CH_3)_2 + CH_3 \qquad (7\text{-}2a)$$

The used model chemistry and the calculation results for 25 °C are summarized in Table 7-3. In each model chemistry in the table, two different kinds of basis sets were used: the first was used for hydrogen and carbon atoms and the second was for indium atom.

Table 7-3. Calculated ΔH and ΔG depending on model chemistry (kcal/mol).

Model Chemistry*	BSSE	ΔH	ΔG
HF/(6-311G(2d,2p)① + LanL2DZ②)	-1.34	-138.9	-148.1
HF/(6-311++G(2d,2p) + LanL2DZ)	-0.98	-139.6	-150.0
B3LYP/(LanL2DZ③ + LanL2DZ)	-1.01	62.7	50.0
B3LYP/(6-311G(2d,2p) + LanL2DZ)	-0.80	62.0	46.8
B3LYP/(6-311++G(2d,2p) + LanL2DZ)	-0.43	61.5	45.1
B3LYP/(6-311G(2d,2p) + SDB-cc-pVTZ④)	-0.91	61.9	53.4
B3LYP/(6-311G(2d,2p) + SDB-aug-cc-pVTZ)	-0.77	64.6	50.8
B3LYP/(6-311++G(2d,2p) + SDB-cc-pVTZ)	-0.26	64.8	50.8
B3LYP/(6-311++G(2d,2p) + SDB-aug-cc-pVTZ)	-0.26	64.4	50.9

*Basis set: the first basis set was used for hydrogen and carbon atoms and the second was for indium. References for the basis sets: ① - Kri80, ② - Hay85, ③ - Dun77, ④ - Ber93 and Mar01.

Only a few basis sets are currently available for indium since it is a very heavy atom. In this work, used for indium atom were Martin/Sundermann Stuttgart relativistic, effective core potential basis sets, i.e. SDB-xxx-cc-pVXX [Ber93, Mar01], and LanL2DZ [Hay85]. Gaussian 03 [Fri03] was used for the calculations and SDB-xxx-cc-pVXX was generated from the Environmental Molecular Science Laboratory (EMSL) Basis Set Library [Ems04]. BSSEs were compensated using the CP correction [Boy70] as described in Chapter 3.

Considering that hemolytic bond fissions without any significant geometry change should accompany positive changes in ΔH and ΔG, the Hartree-Fock cases in Table 7-3 gave considerable errors in these changes, while the other cases with a density functional theory (B3LYP) show positive changes. In the first three of the density functional cases, LanL2DZ basis set was used for indium atom and the size of basis sets for carbon and hydrogen atoms was increased. As expected, the BSSE values became smaller as a bigger basis set was used. In the next four, the size of basis set for indium was also increased using SBD-xxx-cc-pVXX basis sets. It is noticed that the inclusion of diffusion terms in the basis sets is crucial to reduce BSSE, and ΔH and ΔG respectively seem to converge as the size of the basis set increases. ΔH for the same chemical change was previously calculated to be 65.07 kcal/mol with bigger basis sets and a more sophisticated method [All99]. In the last two cases in Table 7-3, the BSSE values are the smallest and the values of ΔH are within a usually accepted chemical accuracy (1~2 kcal/mol) [Sim97] compared with the previously reported value, 65.07 kcal/mol. The last model chemistry in the table was selected for further quantum chemistry calculations.

The selected model chemistry, B3LYP/(6-311++G(2d,2p) + SDB-aug-cc-pVTZ), was tested with frequency calculations for the stretching vibrations of In-C bond in TMIn and MMIn. Experimentally, the vibrations were observed at 476 and 430 cm^{-1} for TMIn and MMIn, respectively. The calculation of the symmetric In-C vibration of TMIn expected the Raman shift at 477 cm^{-1}, giving the scale factor of 0.998. Using the scale factor obtained from the In-C vibration in TMIn, the model chemistry gave 432 cm^{-1} for the In-C vibration of MMIn, which is very close to the experimental observation, 430 cm^{-1}. Therefore, the model chemistry seemed to reasonably describe characteristics of the In-C bond and was used to analyze experimental results in the following. In addition, this model chemistry expected the In-C vibration of DMIn at 441 cm^{-1}, though it has not been experimentally observed yet.

7.3.3 Experimental Results

Raman spectra taken in the ranges of In-C vibrations (390 ~ 510 cm^{-1}) and the atomic indium transition (2215 cm^{-1}) along the centerline of the reactor are presented in Figure 7-10. The gas temperatures in the figure were obtained from the rotation band of nitrogen at each corresponding axial position in the reactor. The lowest spectra (h) in the figure were taken at the position of 152 °C and only show a strong TMIn peak. As the gas temperature increases, i.e. the gases flow toward the heated susceptor, intensity of the TMIn peak goes down and that of the MMIn peak goes up at the same time. At the highest temperatures (Figures 7-10a and b), the two new peaks at 416 and 464 cm^{-1} were recorded in the figure, which have not been reported yet.

The decrease of indium peak at Figure 7-10b seems to be caused by coagulation of atomic indium. Figure 7-11 shows spectra taken in the nitrogen rotation band. There are two extra peaks recorded at 104 and 222 cm^{-1} in the nitrogen rotation band, which are attributed to plasma lines produced in the argon ion laser. These peaks are strongest (Figure 7-11b) at the position where atomic indium peak almost diminishes (Figure 7-10b). This observation indicates that small indium droplets were formed by coagulation of atomic indium in the gas phase and the plasma lines seemed to be directly reflected by the droplets.

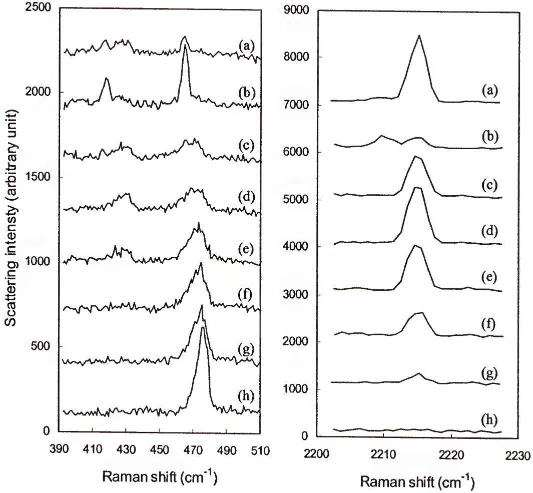

Figure 7-10. Observed spectra in the ranges of In-C vibrations and the atomic indium transition at the positions of (a) 514, (b) 470, (c) 436, (d) 388, (e) 340, (f) 306, (g) 271, and (h) 152 °C along the centerline of the reactor.

The new peaks at 416 and 464 cm^{-1} in Figure 7-10 were observed to have a strong relation with the intensity of atomic indium peak. They appeared as atomic indium peak diminished (Figure 7-10b) and disappeared as atomic indium peak regained a strong intensity (Figure 7-10a). The vapor pressure of coagulated metallic indium is very low within the experimental temperature range and therefore indium in the droplets did not significantly contribute to the reappearance of the strongest atomic indium intensity in Figure 7-10a. This observation suggests the presence of new indium-bearing reaction intermediates besides MMIn. The new intermediates seem to decompose and produce atomic indium as shown in Figure 7-10a. The distance between two points where spectra (a) and (b) in Figure 7-10 were taken was 0.5 mm and therefore the intermediates are considered to decompose very quickly in the high temperature region near the susceptor. Possible reaction intermediates will be discussed in the following section.

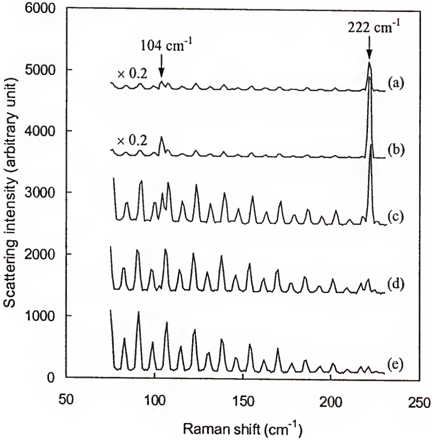

Figure 7-11. Spectra taken in the nitrogen rotation band at the positions of (a) 514, (b) 470, (c) 436, (d) 388, and (e) 271 °C along the centerline of the reactor. The peaks at 104 and 222 cm^{-1} are attributed to plasma lines of the Ar+ laser.

7.3.4 Reaction Intermediates

Stepwise hemolytic fission of the In-C bond in TMIn was first proposed as in Eq. 7-2 [Jac64] and recently MMIn and atomic indium were experimentally observed in the gas phase [Par02b]. It has been suggested from the experimental results in Figure 7-8 that MMIn and/or DMIn seem to hide from Raman detection by forming another intermediates. In addition, the presence of another reaction intermediates except MMIn is evident from the experimental results in Figures 7-10 and 7-11. In this section, quantum chemistry calculations were performed to suggest possible reaction intermediates. Based on the aforementioned consideration, the following reactions were conceived:

$$\mathrm{nMMIn} \Leftrightarrow (\mathrm{MMIn})_n \quad (7\text{-}6a)$$

$$\mathrm{2DMIn} \Leftrightarrow (\mathrm{DMIn})_2 \quad (7\text{-}6b)$$

$$\mathrm{DMIn + MMIn} \Leftrightarrow \mathrm{DMIn\text{-}MMIn} \quad (7\text{-}6c)$$

$$\mathrm{DMIn\text{-}MMIn} \Leftrightarrow \mathrm{CH_3InCH_2 + HInCH_3} \quad (7\text{-}6d)$$

$$\mathrm{TMIn + MMIn} \Leftrightarrow (\mathrm{DMIn})_2 \quad (7\text{-}6e)$$

Reactions 7-6a through 7-6c occur by combining two or more intermediates without significant geometry changes, while Reactions 7-6d and 7-6e seem to experience considerable changes and should overcome potential barriers to produce the reaction products. ΔH and ΔG were calculated for the first three reactions, while barrier heights were additionally estimated for the rest reactions.

To screen possible candidates out of Reactions 7-6a to 6c, simple model chemistry was used first and then more elaborate model chemistry was applied to confirm selected intermediate candidates. The considered intermediates in the reactions are depicted in Figure 7-12 using MOLDEN [Sch04], a visualization tool.

Table 7-4. Average ΔH and ΔG for Reactions 7-6a through 6c for the temperature range 200 to 600 °C (in kcal/mol). Each reaction product is depicted in Figure 7-12.

Reaction	BSSE	ΔH	ΔG	Product
7-6a	3.69	2.78	13.17	(d)
	1.89	1.35	13.86	(e)
	6.55	-4.50	22.80	(f)
	13.28	-28.60	24.80	(g)
7-6b	3.56	-40.49	-8.09	(h)
7-6c	3.34	-9.42	4.59	(i)

ΔH and ΔG for the reactions calculated using MP2/LanL2DZ model chemistry are summarized in Table 7-4. The thermodynamic potential changes in the table were already corrected for BSSE. In Figure 7-12, Structure (j) converged to Structure (f) for $(MMIn)_3$ case and the analogous structure for $(MMIn)_4$ converged to Structure (g) and therefore they were not considered separately. Structures (k) and (l) are related with Reaction 7-6d and they are considered later separately. For the reaction 7-6a, ΔG increases as the number ('n') of MMIn units increases, while ΔH shows a reverse tendency. For trimethylgallium decomposition, the polymer of monomethylgallium was suggested by Jacko and Price [Jac63] and its formation was reported to be energetically favored [Boc94]. It was, however, experimentally shown [Par03] that the material composed of carbon and gallium had separate domains of them, instead of consecutive carbon-gallium bonds. Therefore, as ΔG in Table 7-4 indicates, it is unlikely that polymers of MMIn formed during TMIn decomposition, though their formation is energetically favored. The most probable intermediate is found to be $(DMIn)_2$ based on ΔG. In addition, DMIn-MMIn shows a small ΔG and it looks favorable energetically.

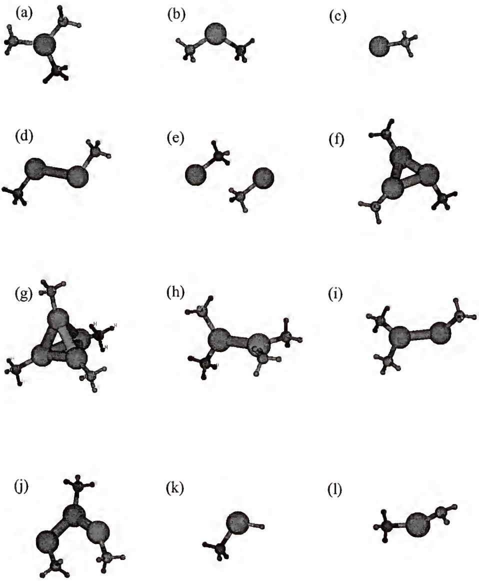

Figure 7-12. Reaction intermediates during TMIn decomposition.

In the following, ΔH and ΔG for $(DMIn)_2$ and DMIn-MMIn formation reactions were estimated using more sophisticated model chemistry: B3LYP/(6-311++G(2d,2p) + SDB-aug-cc-pVTZ) where the first basis set was used for hydrogen and carbon and the second was for indium. Justification of this chemistry model was established in Table 7-3 and its subsequent discussion. The estimation results are given in Table 7-5.

Table 7-5. ΔH and ΔG for the selected reactions using B3LYP/(6-311++G(2d,2p) + SDB-aug-cc-pVTZ). The values (in kcal/mol) are averaged from 200 to 600 °C.

Reaction	BSSE	ΔH	ΔG	Product
7-6b	0.27	-46.04	-19.79	(h)
7-6c	0.26	-17.07	2.13	(i)

In Table 7-5, it is noticed that $(DMIn)_2$ is likely to form by combination of DMIn during TMIn decomposition. In addition, the formation of DMIn-MMIn turned out to be more favorable with the more sophisticated model chemistry, compared with the results in Table 7-4. Smaller values of BSSEs support that the results in Table 7-5 are more reliable than those in Table 7-4.

Reactions 7-6d and 7-6e are considered to involve transition states, because geometry changes are expectedly significant during the reactions. Transition states for these reactions were found with B3LYP/(6-311++G(2d,2p) + SDB-aug-cc-pVTZ):

Reaction 7-6d:

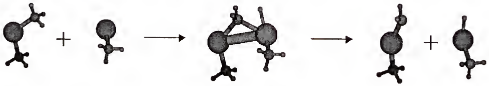

Reaction 7-6e:

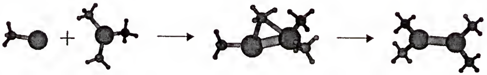

The transition states in the middle of the above reactions are characterized by a single imaginary frequency related to the vibration motion that connects reactants and products smoothly. For a transition state, it is required to confirm that the transition state structure leads to the reactants and products on the reaction coordinate. This confirmation process is called as the intrinsic reaction coordinate (IRC) calculation. For example, the IRC calculation for Reaction 7-6e is given in Figure 7-13. The energy of the reactants was set at zero in the figure.

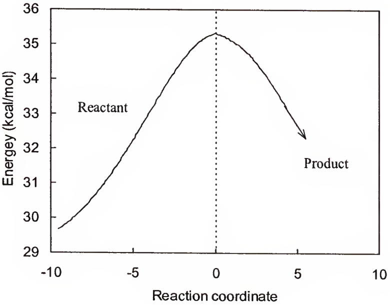

Figure 7-13. IRC calculation for a transition state of $(DMIn)_2$ in Reaction 7-6e.

ΔH and ΔG for the formation of the transition state structures and products were estimated with the same model chemistry used in the transition state identification. Potential barriers for Reactions 7-6d and 7-6e are presented in Table 7-6. The values in Table 7-6 are averaged over the temperature range of 200 to 600 °C and clearly shows the potential barriers.

Table 7-6. ΔH, ΔG, and reaction rate constants for Reactions 7-6d and 7-6e.

	Reaction 7-6d		Reaction 7-6e	
	Transition	Overall	Transition	Overall
ΔH (kcal/mol)	43.1	49.1	38.4	-8.0
ΔG (kcal/mol)	67.9	48.9	56.2	0.9

The presence of reaction intermediates besides MMIn has been suggested from the experimental results in Figure 7-10. Additionally, the figure reveals that a new intermediate is bearing indium atom within it and, therefore, In-C and In-H vibrations were mainly interested in the frequency analysis in the following. Intermediates $(DMIn)_2$, DMIn-MMIn, $HInCH_3$, and CH_3InCH_2 were selected for frequency analysis based on the results in Tables 7-5 and 7-6 (these intermediates are depicted in Figure 7-12). The model chemistry used was B3LYP/(6-311++G(2d,2p) + SDB-aug-cc-pVTZ), where the first basis was used for hydrogen and carbon, and the second was for indium.

Calculated vibration frequencies are summarized in Table 7-7. The scale factor for the In-C symmetric vibration in TMIn has been found to be 0.998, previously. It should be mentioned that one scale factor is specific to the particular type of bond and vibration and therefore it is not expected for the scale factor to work properly for other bond cases.

Table 7-7. Calculated vibrations for selected intermediates.

	$(DMIn)_2$	DMIn-MMIn	$HInCH_3$	CH_3InCH_2
Vibration (cm^{-1})	469 [ν_a(In-C)] 481 [ν_s(In-C)] 486 [ν_s(In-C)]	466 [ν_a(In-C)] 472 [ν_s(In-C)] 486 [ν_a(In-C)]	404 [ν(H-In-C)] 463 [ν(In-C)] 1614 [ν(In-H)]	486 [ν(In-C)] 586 [ν_a(In-C)]

The new Raman peaks at 416 and 464 cm^{-1} in Figure 7-10 are close to thecalculated peaks for $HInCH_3$ in Table 7-7. For this intermediate, the scale factor for ν(H-In-C) was calculated to be 1.03, which is a reasonable value [Sco96]. Therefore, experimental observation of the third vibration (1614 cm^{-1}) will support the presence of $HInCH_3$.

It was reported [Him00] that $HInCH_3$ was formed on a CsI plate cooled by liquid helium. Indium and methane were deposited first and then $HInCH_3$ was observed by infrared (IR) spectroscopy after irradiation of a wide range of ultraviolet light (200 ~ 400 nm). ν(H-In) = 1546 and $\rho(CH_3)$ = 697 cm^{-1} were experimentally observed. MMIn was observed at 422 cm^{-1} in that study, which is slightly different from 430 cm^{-1} of the current study. MMIn was adsorbed on a CsI plate and its electron density might be changed to render less interaction between indium and carbon atoms in MMIn. Considering lowering of vibration frequency of MMIn by adsorption, the gas Raman peak of ν(In-H) is expected to be between 1546 and 1614 cm^{-1}.

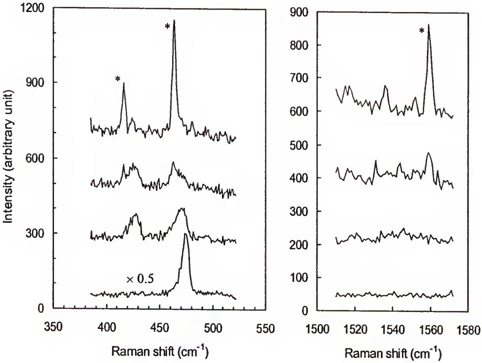

Figure 7-14. Raman spectra in the range of $HInCH_3$ vibrations. Three peaks (*) are distinctive at 416, 464, and 1560 cm^{-1}.

A set of experiments was performed to experimentally confirm the vibration of ν(In-H) by *in situ* Raman spectroscopy and thus obtained spectra are presented in Figure 7-14. The third peak, ν(In-H), was observed at 1560 cm^{-1}, the intensity of which behaves in a parallel fashion as those of the peaks at 416 and 464 cm^{-1}. The relative position in the figure represents relative distance from the inlet tip. The peak at 1560 cm^{-1} was not observed when TMIn and/or MMIn were dominant and started to appear as the peaks at 416 and 464 cm^{-1} did (see '*' in Figure 7-14). Therefore, it is considered that these three peaks are from the same intermediate, $HInCH_3$.

It has been proposed that the new intermediate was responsible for the reappearance of atomic indium peak in Figure 7-10. To provide a reasonable reaction path, the decomposition of $HInCH_3$ was investigated using computational chemistry. The model chemistry used was B3LYP/(6-311++G(2d,2p) + SDB-aug-cc-pVTZ) as the same as before. It was found that $HInCH_3$ decomposes as the hydrogen atom moves toward the methyl group, giving atomic indium and methane:

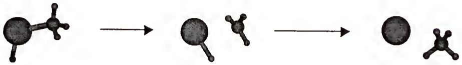

The structure in the middle represents the transition state. ΔH, ΔG, and reaction rate constants were estimated and averaged for the temperature range 200 to 600 °C. ΔH and ΔG for the overall process are -10.0 and -19.0 kcal/mol, respectively. For the transition state complex, ΔH and ΔG are 29.5 and 27.8 kcal/mol, respectively. In addition, reaction constants were obtained to be $E_a = 30.8$ kcal/mol and $k_0 = 1.4\times10^{14}\ s^{-1}$. The low activation energy explains observed quick decomposition of $HInCH_3$ in Figure 7-10.

7.3.5 Conclusions

It has been shown that quantum chemistry is useful in investigating reaction kinetics and mechanism. A new intermediate ($HInCH_3$) was found to exist during TMIn decomposition in a nitrogen carrier. It has some of its characteristic vibrations at 416 [ν(H-In-C)], 464 [ν(In-C)], and 1560 cm^{-1} [ν(H-In)]. The new intermediate was experimentally observed to decompose very quickly in a high temperature region of the reactor. Based on transition state theory, its decomposition rate constants were estimated with applications of quantum chemistry. In addition, it was considered highly probable that $(DMIn)_2$ and DMIn-MMIn would form during TMIn decomposition.

7.4 Interaction between TMIn and Ammonia

When TMIn and ammonia are flow into the reactor at the same time, it is expected for them to form a Lewis acid-base complex, i.e. adduct. In this section, the adduct formation was experimentally observed using *in situ* Raman spectroscopy and the effects of ammonia on TMIn decomposition were investigated.

7.4.1 Experimental

The reactor configuration in Figure 7-9 was used. TMIn, ammonia, and pure nitrogen were supplied to the reactor at a nominal gas velocity of 2.5 cm/s through the center, annulus, and sweep inlet channels, respectively. A TMIn bubbler was immerged in a thermal bath at 36 °C and TMIn concentration at the center flow was 0.48 % in nitrogen. Pure ammonia was used for the ammonia stream into the annulus. For investigation of the adduct formation, temperature of the heating unit inside the quartz envelop was set at 480 °C and a wide range scan from 50 to 3500 cm^{-1} was conducted with the 532 nm line of a solid-state laser (Verdi 8, Coherent Lasers). For TMIn decomposition study in the presence of ammonia, heater temperature was set at 660 °C.

An In-C vibration range (390 ~ 515 cm^{-1}), atomic indium (2215 cm^{-1}), and nitrogen (2331 cm^{-1}) peaks were scanned with the 488 nm line of argon ion laser (Innova 90, Coherent Lasers).

7.4.2 Results and Discussion

To investigate the adduct formation between TMIn and NH_3, characteristic peaks of TMIn were monitored with several experimental conditions. The results were presented in Figure 7-15.

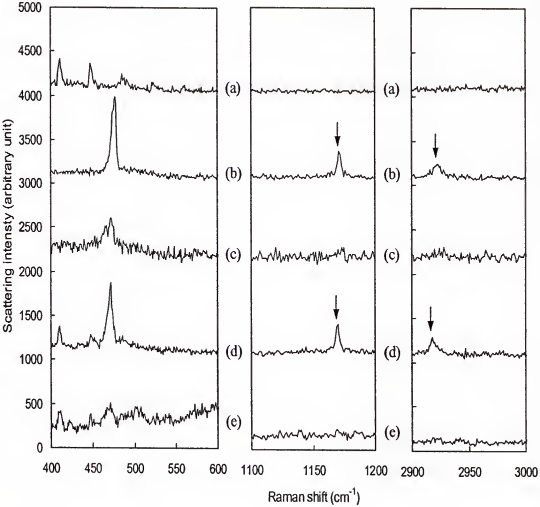

Figure 7-15. Changes in TMIn characteristic peaks for the following conditions: (a) NH_3 only, (b) TMIn only at 98 °C, (c) TMIn only at 384 °C, (d) TMIn and NH_3 at 126 °C, and (e) TMIn and NH_3 at 317 °C.

The gas temperatures in Figure 7-15 were obtained from the nitrogen rotation bands using Eq. 3-21 and they were determined by axial positions in the reactor with the fixed heater temperature (480 °C). The peaks at 476, 1172, and 2923 cm^{-1} were observed for TMIn (Figure 7-14b) and they correspond to ν_s(In-C), $\delta_s(CH_3)$, and ν_s(CH), respectively. NH_3 spectrum at room temperature (Figure 7-15a) shows NH_3 rotation band, which extended to the ν(In-C) vibration range of TMIn. Spectrum (c), i.e. Figure 7-15c, taken with TMIn at a higher temperature (384 °C) position in the reactor shows that the peaks at 1172 and 2923 cm^{-1} nearly disappeared and the ν_s(In-C) vibration was shifted to 472 cm^{-1}. When TMIn and NH_3 were simultaneously supplied into the reactor, three characteristic peaks of TMIn were observed at a lower temperature (126 °C) position, while their spectral positions were shifted to 471, 1170, and 2918 cm^{-1} (see Figure 7-15d). Spectrum (e) taken at a higher temperature (317 °C) position in the same experiment does not show $\delta_s(CH_3)$ and ν_s(CH). Therefore, it is considered that the observed shifts in ν_s(In-C), $\delta_s(CH_3)$, and ν_s(CH) with addition of NH_3, shown in Spectrum (d), were not caused by TMIn decomposition but the shifts reflects the adduct formation between TMIn and NH_3. It was, however, not possible to follow high temperature behaviors of the adduct, because the ν_s(In-C) of the adduct collapses onto that of TMIn at higher temperatures.

The frequency shifts upon the adduct formation were estimated with a quantum chemical method. The Hartree-Hock theory was used for the calculations because vibration frequencies were only interested. Several kinds of basis sets were used and the results are summarized in Table 7-8. The basis set cc-pVDZ-pp [Pet03] is a small core basis set, while LanL2DZ is a large core basis set. The scale factors determined by comparing the calculated vibration shifts with the experimental ν_s(In-C) = 476 cm^{-1} of TMIn were applied to the adduct case. The experimentally observed ν_s(In-C) at 471 $cm^{-1}$of the adduct were very closely estimated in all cases in Table 7-8, even though the Hartree-Fock theory was used in the calculations.

Table 7-8. Estimated ν_s(In-C) of the adduct.

ν_s(In-C) vibration	TMIn	Scale factor	Adduct
6-311G(2d,2p) + LanL2DZ*	476.1	0.9998	470.8
6-311G(2d,2p) + cc-pVDZ-pp	485.6	0.9802	470.7
6-311G(2d,2p) + aug-cc-pVDZ-pp	485.8	0.9798	470.5
6-311++G(2d,2p) + aug-cc-pVDZ-pp	486.0	0.9795	470.4

* The first basis set was used for H, C, and N, and the second was for In.

The decomposition behavior of TMIn in N_2 carrier was investigated previously (Figure 7-10) and it was observed that TMIn peak became smaller while MMIn peak appeared as the gases flowed toward the heated susceptor. At last, two new peaks at 416 and 464 cm^{-1} were observed near the heated susceptor. It is, however, known that Group III metal organic sources (TMAl, TMGa, and TMIn) could react with NH_3 to form a Lewis acid-base complex, i.e. adduct. In the following, effects of NH_3 on TMIn decomposition were qualitatively investigated.

TMIn decomposition behavior in the presence of NH_3 was observed using *in situ* Raman spectroscopy and the results are presented in Figure 7-16. The spectrum (f) in the figure taken about 5 mm above the inlet tip shows a strong ν_s(In-C) vibration, the position of which was shifted by about 5 cm^{-1} from the TMIn case due to the adduct formation. As the gases flowed into higher temperature region, MMIn peak was observed, e.g. Spectrum (d). There are some of NH_3 rotation peaks recorded at 412, 449, and 486 cm^{-1} in the figure. It seems that 416 cm^{-1} peak partially overlaps with the NH_3 rotation peak at 412 cm^{-1}. The peak at 464 cm^{-1} was also observed, though its intensity was not as strong as in Figure 7-10b.

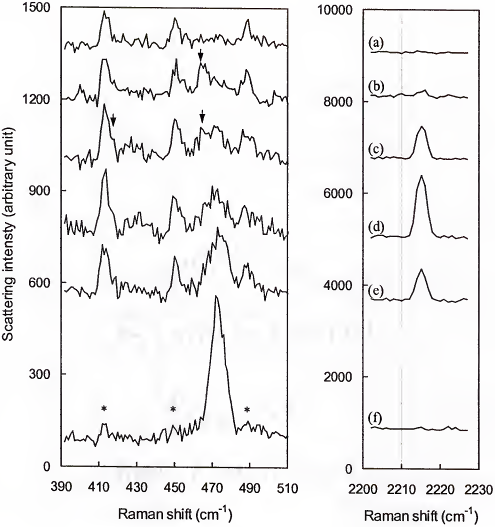

Figure 7-16. TMIn decomposition in the presence of NH_3 at the positions of (a) 512, (b) 463, (c) 434, (d) 334, (e) 303, and (f) 158 °C along the centerline of the reactor. NH_3 rotation peak positions are denoted by (*).

A major difference compared with Figure 7-10 is evident in the atomic indium transition region. Its intensity did not increase again after the sudden disappearance (see Figures 7-10a and 7-16a). Apparently, reaction intermediates did not produce atomic indium again in the high temperature region as previously observed in Figure 7-10a. It is possible that a less amount of $HInCH_3$ was formed during the decomposition in the presence of NH_3 and other intermediates were produced from reactions with NH_3. For the TMG and NH_3 case, it has been reported that the adduct starts to dissociate into TMG and NH_3 at 150 °C [Kim94]. In the current case, such dissociation is expected to occur and this explains the increasing trend of the atomic indium peak intensity as in Figure 7-10 until the peak disappeared and the observation of MMIn peak. It was, however, different that the intensity of the atomic indium peak did not regain its intensity near the heated susceptor (Figure 7-16a). Therefore, it is considered that NH_3 (or its derivatives) reacted with decomposition intermediates of TMIn in the high temperature region and more stable intermediates containing indium and nitrogen were possibly produced, and indium was not released from the stable intermediates even at the high temperature region. It is likely that In-N bond was formed in the gas phase at the high temperature region.

7.4.3 Conclusions

The adduct of TMIn and NH_3 was observed by 5 cm^{-1} shift of ν_s(In-C) vibration in the low temperature region of the reactor. For simultaneous supply of TMIn and ammonia, TMIn was considered to decompose in the same way as in the TMIn alone case until a high temperature region near the susceptor was reached. It is considered that decomposition intermediates of TMIn reacted with NH_3 (or its reaction derivatives) near the heated susceptor and the reaction product was stable.

CHAPTER 8
CONCLUSIONS AND RECOMMENDATIONS

A new methodology was established to quantitatively understand the physical/chemical behavior of precursors used in MOCVD with effective distinction of gas phase and surface reactions. The methodology consists of *in situ* Raman scattering signals collection, modeling the process, and extracting unknown parameters from the experimental data.

To obtain information on a physical/chemical process without disturbing it, a measurement reactor interfaced with a Raman spectrometer was built. Raman scattering can simultaneously provide temperature and species information with good spatial resolution and therefore it is a viable tool to study chemical reactions. With this apparatus it was possible to obtain more detailed information about the process, e.g., temperature and/or concentration profiles inside the reactor, while only lumped-information has been available with flow cell/tube reactors. No physical sampling mechanism is involved in probing physical/chemical processes in the reactor and therefore experimental observation with this apparatus is considered to reflect more realistic information.

To take full advantage of *in situ* observation with the experimental apparatus, a detailed reactor model describing momentum, heat, and mass transport in the reactor was developed and validated. *in situ* observation of a process gives a qualitative view of the process, while it can be further used to obtain quantitative insights into the process. It is, however, required to have a proper tool to analyze *in situ* observation and reveal implicit information from the observation. In this work, the detailed reactor model was validated for mass and heat transport with experimental data. The validated reactor model provided further information beyond direct observation, e.g., temperature, concentration, and velocity fields in the reactor. Therefore, the model can be used to reasonably separate gas phase and surface contributions to metalorganic precursor decomposition, which has been one of the unresolved issues in the decomposition study. In addition, the model can be used to tailor experimental or operation conditions for a specific goal.

A parameter estimation procedure was established in this work. In many cases, crucial parameters in an interested process are unknown and required to be determined, e.g., reaction kinetic constants, diffusivity, and Raman cross-section. Values of the cross-section of reaction intermediates are required to quantitatively analyze their concentration inside the reactor. A genetic algorithm was implemented along with the Simplex algorithm to efficiently estimate those parameters with reduced computational cost, because the reactor model consists of several partial differential equations and complex reactor geometry. The parameter estimation procedure was able to estimate diffusivities and relative Raman cross-sections of methane and ammonia in methane/nitrogen and ammonia/nitrogen gas mixtures, respectively.

The established methodology and its components were used to investigate characteristics of the reactor, decomposition of TMIn and NH_3, and dissociation behavior of $(TMAl)_2$. During this work, a computational chemistry tool, Gaussian 03, was utilized to predict vibration frequencies, thermodynamic properties, and reaction rate constants.

Gas dynamics of the reactor was studied using hydrogen and nitrogen carriers. It was found that the inverted upflow configuration of the current reactor provides forced convection dominant flow fields due to the stabilizing density gradient developed in the reactor. A larger thermal gradient normal to the susceptor surface was obtained with a higher gas flow velocity and the use of nitrogen carrier gas. Detailed treatment of heat transport was found to be critical in obtaining realistic temperature predictions. Mass transport characteristics in the reactor were also studied and flow instability caused by solutal density gradients was observed. Onset of instability was characterized by solutal density difference, gas velocity, and distance traveled by the gas. In MOCVD reactors, the density distribution due to molecular weight difference is very wide and the driving force for natural convection is always present. Therefore, the buoyancy caused by solutal density variations should be carefully considered when MOCVD processes are designed, scaled, and optimized.

Ammonia behavior in the flow reactor was investigated with four different heater temperatures: 300, 500, 700, and 900 °C. It was observed that ammonia disappeared on the susceptor surface, i.e., quartz. The values of activation energy with a simple reaction rate model were 10.9, 12.6, 14.5, and 15.8 kcal/mol for heater temperatures of 300, 500, 700, and 900 °C, respectively. Surface decomposition was dominant, while gas phase reaction was negligible. It should be noted that transmittance of quartz is a function of temperature and wavelength of the light. It was found that the temperature variations across the wall within physical detection range in the measurement reactor were small enough not to give any noticeable influences on transmittance across the reactor walls.

The dissociation of $(TMAl)_2$ into TMAl was observed in the reactor. With the heater temperature of 300 °C, it showed nearly complete dissociation at 135 °C position in the reactor. The reactor model was able to reproduce its dispersion behavior at room temperature and showed recirculation patterns caused by natural convection over a wide region in the reactor. It was found that the natural convection due to solutal density differences could be mitigated by applying heat in the current inverted geometry of the reactor.

The decomposition of TMIn was investigated using the new methodology. Applying the parameter estimation procedure, the frequency factor and activation energy for the 1st order homogeneous decomposition of TMIn were estimated: $10^{17.9}$ s^{-1} and 56.1 kcal/mol. At the same time, the relative Raman cross-section of TMIn was also estimated to be 22.3 for the symmetric In-C vibration (476 cm^{-1}). With these estimates found to be unique in a reasonable parameter space, the reactor model showed that TMIn started to decompose at 120 °C, while a previous study with the same carrier gas in a flow cell reactor showed 340 °C. This lower decomposition temperature is a consequence of *in situ* probing. At the conditions of this study, the decomposition of MMIn was found to occur on the susceptor surface as well as in the gas phase, while TMIn completely decomposed in the gas phase. In a further study, a new reaction intermediate ($HInCH_3$) was identified during TMIn decomposition. The intermediate is found to have Raman-active characteristic vibrations at 416 [ν(H-In-C)], 464 [ν(In-C)], and 1560 cm^{-1} [ν(In-H)]. Its decomposition kinetic constants were estimated using quantum chemistry calculations: $k_0 = 1.4\times10^{14}$ s^{-1} and $E_a = 30.8$ kcal/mol. It was also found highly probable that the dimer of DMIn would form during TMIn decomposition.

The adduct of TMIn and NH_3 was identified by observing 5 cm^{-1} shift of the symmetric In-C vibration at a low temperature point (126 °C) of the reactor. Quantum chemistry calculations gave a reasonable prediction of this shift. TMIn is considered to decompose in the same way as the TMIn alone case until the high temperature region near the susceptor is reached. It is considered that decomposition intermediates of TMIn reacted with NH_3 near the heated susceptor and the reaction product seemed stable.

LIST OF REFERENCES

Abr91 Abraham, P., A. Bekkaoui, V. Souliere, J. Bouix and Y. Monteil, *J. Crsyt. Growth*, 107, 21-31 (1991).

Alb87 Alberty, R.A., *Physical Chemistry*, Ch. 21, John Wiley and Sons, New York, 1987.

All99 Allendorf, M.D., C.F. Melius and C.W. Bauschlicher Jr., *J. Phys. IV France*, 9, Pr8-23 (1999).

Alm71 Almenningen, A., S. Halorsen and A. Haaland, *Act. Chem. Scand.*, 25, 1937-1945 (1971).

Alm92a Almond, M.J., C.E. Jenkins, and D.A. Rice, *J. Organometal. Chem.*, 439, 251-261 (1992).

Alm92b Almond, M.J., M.G.B. Drew, C.E. Jenkins, and D.A. Rice, *J. Chem. Soc. Dalton Trans.*, 5-9 (1992).

Ama92 Amato, C.C., J.B. Hudson and L.V. Interrante, *Appl. Surf. Sci.*, 54, 18-24 (1992).

Amb98 Ambacher, O., *J. Phys. D: Appl. Phys.*, 31, 2653-2710 (1998).

Asa80 Asawaroengchai, C. and G.M. Rosenblatt, *J. Chem. Phys.*, 72, 2664-2669 (1980).

Asp89 Aspnes, D.E., R. Bhat, E. Colas. V.G. Keramidas, M.A. Koza, and A.A. Studha, *J. Vac. Sci. Technol.*, A7, 711-716 (1989).

Ati91 Atiya, G.A., A.S. Grady, D.K. Russell and T.A. Claxton, *Spectrochim. Act.*, 47A, 467-476 (1991).

Ban89 Bank, H.T. and K. Kunisch, *Estimation Techniques for Distributed Parameter Systems*, Ch. 4, Birkhäuser, Boston, 1989.

Bar87 Baranska, H., A. Labudzinska, and J. Terpinski, *Laser Raman Spectroscopy*, Halsted Press, New York, 1987.

Bat88 Bates, D.M. and D.G. Watts, *Nonlinear Regression Analysis and Its Applications*, John Wiley & Sons, New York, 1988.

Baz93 Bazaraa, M.S., H.D. Sherali and C.M. Shetty, *Nonlinear Programming*, 2nd ed., John Wiley & Sons, New York, 1993.

Bec02 Bechsredt, F. and J. Furthmüller, *J. Cryst. Growth*, 246, 315-319 (2002).

Ben74 Bendtsen, J., *J. Raman Spec*., 2, 133 (1974).

Ber93 Bergner, A., M. Dolg, W. Kuechle, H. Stoll and H. Preuss, *Mol. Phys*., 80,1431 (1993).

Ber95 Bernath, P.F., *Spectra of Atoms and Molecules*, Oxford University Press, 1995.

Ber98 Berthomieu, D., Y. Bacquet, L. Pedocchi and A. Goursot, *J. Phy. Chem. A*, 102, 7821-7827 (1998).

Ber99 Bergmann, U., V. Reimer and B. Atakan, *Phys. Chem. Chem. Phys*., 1, 5593-5599 (1999).

Beu91 Beuermann, Th. and M. Stuke, *Chem. Phys. Lett*., 178, 197-203 (1991).

Bir60 Bird, R.B., W.E. Stewart, and E.N. Lightfoot, *Transport Phenomena*, John Wiley & Sons, New York, 1960.

Boc94 Bock, C.W. and M. Trachtman, *J. Phys. Chem*., 98, 95-99 (1994).

Boy70 Boys, S.F. and F. Bernardi, *Mol. Phys*., 19, 553-566 (1970).

Box78 Box, G.E.P., W.G. Hunter and J.S. Hunter, *Statistics for Experimenters*, Ch. 7, John Wiley & Sons, New York, 1978.

Bri97 Briot, O., J.P. Alexis, M. Tchounkeu, and R.L. Aulombard, *Mater. Sci. Eng*., B43, 147-153 (1997).

Buc88 Buchan, N.I., C.A. Larsen and G.B. Stringfellow, *J. Cryst. Growth*, 92, 591-604 (1988).

Bur87 Burnett, D.S., *Finite Element Analysis*, Addison-Wesley, Sydney, 1987.

But71 Butcher, R.J., D.V. Willetts and W.J. Jones, *Proc. Roy. Soc. Lond. A*, 324, 231-245 (1971).

But86 Butler, J.E., N. Bottka, R.S. Sillmon and D.K. Gaskill, *J. Cryst. Growth*, 77, 163-171 (1986).

Cha64 Chandler, C., *Atomic Spectra and the Vector Model*, 1964.

Cha73 Chavent, G., *The 3rd IFAC Sympo. on Ident. & Syst. Param. Est*., the Hague/Delft, 649-660 (1973).

Cha95 Charbonneau, P. and B. Knapp, *A User's Guide to PIKAIA 1.0*, NCAR Technical Note #TN-418+IA, 1995.

Che81 Cheung, L.M. and M. Bishop, *Chem. Phys. Lett.*, 80, 445-450 (1981).

Che91 Chen, Q. and P.D. Dapkus, *J. Electrochem. Soc.*, 138, 2821-2825 (1991).

Che96 Chen, C.H., H. Liu, D. Steigerwalt, W. Imiler, C.P. Kuo, and M.G. Craford, *Mat. Res. Soc. Symp. Proc.*, 395, 103-108 (1996).

Chi91 Chinoy, P.B., D.A. Kaminski, S.K. Ghandhi, *Solar Cells*, 30, 323 (1991).

Cot90 Cotton, F.A., *Chemical Applications of Group Theory*, Wiley Interscience, New York, 1990.

Cra02 Cramer, C.J., *Essentials of Computational Chemistry*, John Wiley & Sons, 2002.

Cre02 Creighton, J.R., W.G. Breiland and M.E. Coltrin, *Electrochemical Soceity Proceedings*, 2002-03, 28-35 (2002).

Cur49 Curtiss, C.F. and J.O. Hirschfelder, *J. Chem. Phys*., 17, 550-555 (1949).

Cur99 Curtiss, C.F. and R.B. Bird, *Ind. Eng. Chem. Res*., 38, 2515-2522 (1999).

Dav90 Davison, D.F., K. Kohse-Höinghaus, A.Y. Chang and R.K. Hanson, *Int. J. Chem. Kinet.*, 22, 513 (1990).

Den86 DenBaars, S.P., B.Y. Maa, P.D. Dapkus, A.D. Danner, and H.C. Lee, *J. Crystal Growth*, 77, 188-193 (1986).

Dil91 Dillon, A.C., P. Gupta, M.B. Robinson, A.S. Bracker and S.M. George, *J. Vac. Sci. Technol.*, A9, 2222-2228 (1991).

Dov79 Dove, J.E. and W.S. Nip, *Can. J. Chem*. 57, 689-701 (1979).

Dra66 Draper, N.R. and H. Smith, Applied Regression Analysis, ch. 10, John Wiley & Sons, New York, 1966.

Dra81 Draper, N.R. and H. Smith, *Applied Regression Analysis*, John Wiley & Sons, 1981.

Dra82 Drake, M.C., C. Asawaroengchai, D.L. Drapche, K.P. Veirs and G.M. Rosenblatt, *Temperature*, 5, 621-629 (1982).

Dun77 Dunning, T. H., Jr. and P. J. Hay, in *Methods of Electronic Structure, Theory*, Vol. 2, H. F. Schaefer III, ed., Plenum Press (1977).

Dur81 Durig, J.R. and K.K. Chatterjee, *J. Raman Spectroscopy*, 11, 168-173 (1981).

Dur82 Durig, J.R., C.B. Bradley, and J.D. Odom, *Inorg. Chem.*, 21, 1466-1472 (1982).

Dur95 Durst, F., L. Kadinski and M. Schäfer, *J. Cryst. Growth*, 146, 202-208 (1995).

Eck59 Eckert, E.R.G. and R.M. Drake, *Heat and Mass Transfer*, Part C, Ch. 13, McGraw-Hill, New York, 1959.

E1192 Ellis, A.M., E.S.J. Robles, and T.A. Miller, *Chem. Phys. Lett.*, 190, 599-604 (1992).

Ems04 EMSL requested citation: Basis sets were obtained from the Extensible Computational Chemistry Environment Basis Set Database, Version 02/25/04, as developed and distributed by the Molecular Science Computing Facility, Environmental and Molecular Sciences Laboratory which is part of the Pacific Northwest Laboratory, P.O. Box 999, Richland, Washington 99352, USA, and funded by the U.S. Department of Energy. The Pacific Northwest Laboratory is a multi-program laboratory operated by Battelle Memorial Institute for the U.S. Department of Energy under contract DE-AC06-76RLO 1830. Contact David Feller or Karen Schuchardt for further information.

Eva87 Eavns, G.H. and R. Grief, *Numer. Heat Transfer*, 12, 243-252 (1987).

Eva97 Evans, K.R., T. Lei, and C.R. Jones, *Solid-State Electron.*, 41, 339-343 (1997).

Fie84 Field, R.J., and S.K. Ghandhi, *J. Crystal Growth*, 69, 581-588 (1984).

Fot90a Fotiadis, D.I., M. Boekholt, K.F. Jensen and W. Richter, *J. Cryst. Growth*, 100, 577-599 (1990).

Fot90b Fotiadis, D.I., S. Kieda and K.F. Jensen, *J. Cryst. Growth*, 102, 441-470 (1990).

Fot90c Fotiadis, D.I. and S. Kieda, *J. Cryst. Growth*, 102, 441-470 (1990).

Fra91 Francis, J.T., S.W. Benson, and T.T. Tsotsis, *J. Phys. Chem.*, 95, 4583-4586 (1991).

Fri03 Frisch, M. J., G. W. Trucks, H. B. Schlegel, G. E. Scuseria, M. A. Robb, J. R. Cheeseman, J. A. Montgomery, Jr., T. Vreven, K. N. Kudin, J. C. Burant, J. M. Millam, S. S. Iyengar, J. Tomasi, V. Barone, B. Mennucci, M. Cossi, G. Scalmani, N. Rega, G. A. Petersson, H. Nakatsuji, M. Hada, M. Ehara, K. Toyota, R. Fukuda, J. Hasegawa, M. Ishida, T. Nakajima, Y. Honda, O. Kitao, H. Nakai, M. Klene, X. Li, J. E. Knox, H. P. Hratchian, J. B. Cross, C. Adamo, J. Jaramillo, R. Gomperts, R. E. Stratmann, O. Yazyev, A. J. Austin, R. Cammi, C. Pomelli, J. W. Ochterski, P. Y. Ayala, K. Morokuma, G. A. Voth, P. Salvador, J. J. Dannenberg, V. G. Zakrzewski, S. Dapprich, A. D. Daniels, M. C. Strain, O. Farkas, D. K. Malick, A. D. Rabuck, K. Raghavachari, J. B. Foresman, J. V. Ortiz, Q. Cui, A. G. Baboul, S. Clifford, J. Cioslowski, B. B. Stefanov, G. Liu, A. Liashenko, P. Piskorz, I. Komaromi, R. L. Martin, D. J. Fox, T. Keith, M. A. Al-Laham, C. Y. Peng, A. Nanayakkara, M. Challacombe, P. M. W. Gill, B. Johnson, W. Chen, M. W. Wong, C. Gonzalez, and J. A. Pople, *Gaussian 03, Revision B.04*, Gaussian, Inc., Pittsburgh PA, 2003.

Gen97 Gen, M. and R. Cheng, *Genetic Algorithms and Engineering Design*, John Wiley, New York, 1997.

Gil82 Giling, L.J., *J. Electrochem. Soc.*, 129, 634-644 (1982).

God78 Godson, E.P. and M.P. Polis, *Identification of Parameters in Distributed Systems* in Distributed Parameter Systems, ed. by W.H. Ray and D.G. Lainiotis, Marcel Dekker, New York, 1978.

Gol89 Goldberg, D.E., *Genetic Algorithms in Search, Optimization, and Machine Learning*, Addison-Wesley Publishing Co., 1989.

Gre86 Grefenstette, J.J., *IEEE Syst., Man, Cybern.*, SMC-16, 122-128 (1986).

Gru89 Grunzburger, M.D., *Finite element methods for viscous incompressible flows*, Academic Press, New York, 1989.

Guh96 Guha, S., N.A. Bojarczuk, and D.W. Kisker, *Appl. Phys. Lett.*, 69, 2879-2881 (1996).

Guo02 Guo, S., M. Pophristic, B. Peress and I. Ferguson, *Electrochem. Soc. Proc.*, 2002-3, 141 (2002).

Gup88 Gupta, P., V.L. Colvin and S.M. George, *Phys. Rev.*, 37, 8234 (1988).

Hai83 Haigh, J., *J. Mater. Sci.*, 18, 1072-1076 (1983).

Has79 Hastie, J.W., *Characterization of High Temperature Vapors and Gases, NBS SP-561*, 609, U.S. Government Printing Office, Washington, 1979.

Has84 Hashimoto, M., H. Amano, N. Sawaki, and I. Akasaki, *J. Crystal Growth*, 68, 163-168 (1984).

Hay85 Hay, P. J. and W. R. Wadt, *J. Chem. Phys.*, 82, 299 (1985).

Heb90 Hebner, G.A. and K.P. Killeen, *J. Appl. Phys.*, 67, 1598-1600 (1990).

Hei81 Heinrich, J.C. and R.S. Marshall, *Computers and Fluids*, 9, 73-83 (1981).

Hei84 Heinecke, H., E. Veuhoff, N. Putz, M. Heyen, and P. Balk, *J. Electron. Mater.*, 13, 815-830 (1984).

Her90a Herbner, G.A. and K.P. Killeen, *J. Appl. Phys.* 67, 1598-1600 (1990).

Her90b Hersee, S.D. and J.M. Ballingall, *J. Vac. Sci. Technol.*, A8, 800-804 (1990).

Him99 Himmel, H.-J., A.J. Downs, T. Greene and L. Andrews, *Chem. Comm.*, 2243-2244 (1999).

Him00 Himmel, H.-J., A.J. Downs, T.M. Greene and L. Andrews, *Organometallics*, 19, 1060-1070 (2000).

Hir54 Hirschfelder, J.O., C.F. Curtiss, and R.B. Bird, *Molecular Theory of Gases andLiquids*, p. 538, John Wiley & Sons, New York, 1954.

Hir82 Hirtz, J.P., M. Razeghi, M. Bonnet and J.P. Duchemin, in: T.P. Pearsall (Ed.), *GaInAsP Alloy Semiconductors*, Ch. 3, John Wiley and Sons, New York, 1982.

Hir94 Hiraoka, Y.S. and M. Mashita, *J. Cryst. Growth*, 145, 473-477 (1994).

Hol75 Holland, J.H., *Adaptation in Natural and Artificial Systems*, Cambridge, MIT press, 1975.

Hol92 Holster, W.L., *Prog. Cryst. Growth Charact.*, 24, 111-211 (1992).

Hos90 Hoshino, M., *J. Appl. Phys.*,68, 2538-2540 (1990).

Hua93 Huang, Z., C. Park and T.J. Anderson, *J. Organomet. Chem.*, 449, 77-84 (1993).

Hug79 Hughes, T.J.R., W.K. Liu, and A. Brooks, *J. Comput. Phys.*, 30, 1-60 (1979).

Hwa04 Hwang, J.Y., C. Park, M. Huang and T.J. Anderson, *J. Cryst. Growth*, Accepted with Minor Corrections (2004).

Ibu89 Ibuki, T., A. Hiraya, K. Shobatake, Y. Matsumi and M. Kawasaki, *Chem. Phys. Lett.*, 160, 152-156 (1989).

Ing88 Ingle, J.D., and S.R. Crouch, *Spectrochemical Analysis*, Prentice-Hall, 1988.

Int89 Interrante, L.V. and W. Lee, *J. Electrochem. Soc.*, 136, 472-478 (1989).

Ito88 Itoh, H., M. Watanabe, S. Mukai and Yajima, *J. Cryst.Growth*, 93, 165-169 (1988).

Jac63 Jacko, M.G. and S.J.W. Price, *Can. J. Chem.*, 41, 1560-1567 (1963).

Jac64 Jacko, M.G. and S.J.W. Price, *Can. J. Chem.*, 42, 1198-1205 (1964).

Jen84 Jenkinson, J.P. and R. Polland, *J. Electrochem. Soc.*, 131, 2911-2917 (1984).

Jen89 Jensen, K.F., *J. Cryst. Growth*, 98, 148-166 (1989).

Jen91 Jensen, K.F., D.I. Fotiadis and T.J. Mountziaris, *J. Cryst. Growth*, 107, 1-11 (1991).

Jer01 Jervase, J.A., H.Bourdoucen and A. Al-Lawati, *Meas. Sci. Technol.* 12, 1922-1925 (2001).

Joh32 Johnson, W.C., J.B. Parson, and M.C. Crew, *J. Phys. Chem.*, 36, 2651-2654 (1932).

Jun98 Jung, J.H., C.H. Lee and I. Lee, *Comput. Chem. Engng.*, 22, 1725 (1998).

Jur98 Jursic, B.S., *J. Mol. Struct. (Theochem)*, 428, 61-66 (1998).

Kad95 Kadinski, L., Yu.N. Makarov, M. Schäfer, M.G. Vasilev and V.S. Yuferev, *J. Cryst. Growth*, 146, 209-213 (1995).

Kel97 Kelman, J.B. and A.R. Masri, *Appl. Optics*, 36, 3506-3514 (1997).

Kill92 Killeen, K.P., *Appl. Phys. Lett.*, 61, 1864-1866 (1992).

Kim94 Kim, S.H., H.S. Kim, J.S. Hwang, J.G. Choi, and P.J. Chong, *Chem. Mater.*, 6, 278-281 (1994).

Kim01 Kim, K.-S., K.-B. Kim and S.-H. Kim, *J. Cryst. Growth*, 233, 167-176 (2001).

Kit70 Kittrell, J.R., *Adv. Chem. Eng.*, 8, 97-183 (1970).

Kol98 Koleske, D.D., A.E. Wickenden, R.L. Henry, W.J. DeSisto, and R.J. Gorman, *J. Appl. Phys.*, 84, 1998-2010 (1998).

Kop84 Koppitz, M., O. Vestavik, and W. Pletschen, *J. Crystal Growth*, 68, 136-141 (1984).

Kri80 Krishnan, R., J.S. Binkley, R. Seeger and J.A. Pople, *J. Chem. Phys.*, 72, 650 (1980).

Kub77 Kubrusly, C.S., *Int. J. Control*, 26 (4), 509-535 (1977).

Kus85 Kusumoto, Y., T. Hayashi and S. Komiya, *Japan. J. Appl. Phys*., 24 (5), 620-625 (1985).

Lar86 Larsen, C.A. and G.B. Stringfellow, *J. Crystal Growth*, 75, 247-254 (1986).

Lar87 Larsen, C.A., N.I. Buchan and G.B. Stringfellow, *J. Cryst. Growth*, 85, 148-153 (1987).

Lar90 Larsen, C.A., N.I. Buchan, S.H. Li, and G.B. Stringfellow, *J. Crystal Gowth*, 102, 103-116 (1990).

Lev91 Levine, I.N., *Quantum Chemistry*, 4th ed., Prentice-Hall, 1991.

Li98 Li, G., S.J. Chua, and W. Wang, *Chem. Vap. Deposit.*, 4, 186-189(1998).

Liu78 Liu, S.S. and D.A. Stevenson, *J. Elcetrochem. Soc*., 125, 1161-1169 (1978).

Liu94 Liu, H. and D.C. Bertolet, J.W. Rogers, *Surface Science*, 320, 145 (1994).

Lon58 Long, L.H. and J.F. Sackman, *Trans. Faraday Soc*., 54, 1797-1803 (1958).

Lon77 Long, D.A., *Raman Spectroscopy*, McGraw-Hill, New York, 1977.

Lüc88 Lückerath, R., P. Tommack, A. Hertliz, H.J. Koss, P. Balk and K.F. Jensen, *J. Cryst. Growth*, 93, 151-158 (1988).

Man96 Man, K.F., K.S. Tang and S. Kwong, *IEEE Trans. Ind. Electron*., 43, 519-533 (1996).

Mar01 Martin, J.M.L. and A. Sundermann, *J. Chem. Phys*., 114, 3408 (2001).

Maz89 Mazzarese, D., A. Tripathi, W.C. Conner, K.A. Jones, L. Calderon, and D.W. Eckart, *J. Electron. Mater*., 18, 369-377 (1989).

Mcd00 McDaniel, A.H. and M.D. Allendorf, *Chem. Mater*., 12, 450-460 (2000).

Mes98 Mesrine, M., N. Grandjean, and J. Massies, *Appl. Phys. Lett*., 72, 350-352 (1998).

Mez67 Mezaki, R. and J.R. Kittrell, *Ind. Eng. Chem*., 59 (5), 63-69 (1967).

Mic95 Michalewicz, Z., *Genetic Algorithms + Data Structures = Evolution Programs*, Ch. 5, Springer-Verlag, 1995.

Mih98 Mihopoulos, T.G., V. Gupta and K.F. Jensen, *J. Cryst.Growth*, 195, 733-739 (1998).

Mil86 Milton, J.S. and J.C. Arnold, *Probability and Statistics in the Engineering and Computing Science*, McGraw-Hill, New York, 364, 1986.

Mit85 Mitchell, S.A., P.A. Hackett, D.M. Rayner, and M.R. Humphries, *J. Chem. Phys.*, 83, 5028-5042 (1985).

Mof86 Moffat, H and K.F. Jensen, *J. Cryst.Growth*, 77, 108-119 (1986).

Mon86 Monteil, Y., M.P. Berthet, R. Favre, A. Harris, and J. Bouix , *J. Crystal Growth*, 77, 172-181 (1986).

Mon88 Monteil, Y., R. Favre, A. Bekkaoui, P. Raffin, J. Bouix, M. Marcillat and P. Dutto, *J. Cryst. Growth*, 93, 270-278 (1988).

Moo97 Moon, R.L., *J. Cryst. Growth*, 170, 1-10 (1997).

Mor94 Morkoc, H., S. Strite, G.B. Gao, M.E. Lin, B. Sverdlov, and M. Burns, *J. Appl. Phys.*, 76, 1363-1398 (1994).

Mor97 Morkoc, H., *Mater. Sci. Eng.*, B43, 137-146 (1997).

Mou91 Mountziaris, T.J. and K.F. Jesen, *J. Electrochem. Soc.*, 138, 2426-2439 (1991).

Mou93 Mountziaris, T.J., S. Kalyanasundaram, and N.K. Ingle, *J. Crystal Growth*, 131, 283-299 (1993).

Muk98 Mukai, T., D. Morita and S. Nakamura, *J. Cryst. Growth*,189/190, 778-781 (1998).

Mül96 Müller, J., *J. Am. Chem. Soc.*, 118, 6370-6376 (1996).

Mül99 Müller, J., U. Rsuschewitz, O. Indris, H. Hartwig and W. Stahl, J. Am. Chem. Soc., 121, 4647-4652 (1999).

Nak91 Nakamura, S., T. Mukai, and M. Senoh, *Jpn. J. Appl. Phys.*, 30, L1998-L2001 (1991).

Nak97 Nakamura, S., *Solid Sate Comm.*, 102, 237-248 (1997).

Nak99 Nakamura, S., *Phys. Stat. Sol. (A)*, 176, 15-22 (1999).

Nas01 Nassen, N.M., Y.Z. Zhen, L. Jiawei and X.Y. Bou, *J. Microwaves and Optoelectronic*, 2, 22-31 (2001).

Neu72 Neufeld, P.D., A.R. Janzen and R.A. Aziz, *J. Chem. Phys.*, 57, 1100-1102 (1972).

Nis97 Nishizawa, J. and T. Kurabayashi, *Thin Solid Films*, 306, 179-186 (1997).

Nis01a Nishida, T., H. Sato and N. Kobayashi, *Appl. Phys. Lett.*, 78, 3927-3928 (2001).

Nis01b Nishida, T., H. Sato and N. Kobayashi, *Appl. Phys. Lett.*, 711-712 (2001).

Nou02 Nougués, J.M., M.D. Grau and L. Puigjaner, *Chem. Eng. Sci.*, 41, 303-309 (2002).

Obr71 O'Brien, R.J. and G.A. Ozin, *J. Chem. Soc. A*, 1136-1138 (1971).

Odo81 Odom, J.D., K.K. Chatterjee and J.R. Durig, *J. Mol. Struct.*, 71, 73-84 (1981).

Oh91 Oh, I.-H. and C.G. Takoudis, and G.W. Neudeck, *J. Electrochem. Soc.*, 138, 554-567 (1991).

Oik88 Oikawa, S., M. Tsuda and M. Morishita, M. Mashita, Y. Kuniya, *J. Cryst. Growth*, 91, 471-480 (1988).

Oka98 Okamoto, M., T. Nonaka, S. Ochiai and D. Tomoinaga, *Appl. Math. Compt.*, 91, 63-72 (1998).

Par92 Park, C., *Studies on Chemical Vapor Deposition in the Gallium Indium Arsenide Phosphide System*, PhD dissertation, University of Florida, 1992.

Par98 Park, T.-Y. and G.F. Froment, *Computers Chem. Eng.*, 22, S103-S110 (1998).

Par00a Parchevsky, K.V., *Ecological Modelling*, 133, 107-115 (2000).

Par00b Park, T.-Y. and G.F. Froment, *Ind. Eng. Chem. Res.*, 40, 4187-4196 (2001).

Par02a Park, C., J.Y. Hwang, M. Huang and T.J. Anderson, *Thin Solid Films*, 409, 88-97 (2002).

Par02b Park, C., W.-S. Jung, Z. Huang and T.J. Anderson, *J. Mater. Chem.*, 12, 356-360 (2002).

Par03 Park, C., S. Han, C. Doh, S. Yeo, D. Yoon, S.-K. Hwang, K.-H. Lee and T.J. Anderson, *Electrochem. Soc. Proc.,* 2003-08, 92-97 (2003).

Pat89 Patniak, S., R.A. Brown and C.A. Wang, *J. Cryst. Growth*, 96, 153-174 (1989).

Pla84 Platten, J.K. and J.C. Legros, *Convection in Liquids*, Ch. 1, Springer-Verlag, New York, 1984.

Pel01 Pelekh, A.P. and R.W. Carr, *J. Phys. Chem. A*, 105, 4697-4701 (2001).

Pes98 Peskin, A.P. and G.R. Hardin, *J. Crystal Growth*, 186, 495-510 (1998).

Pet03 Peterson, K.A., *J. Chem. Phys.*, 119, 11099-11112 (2003).

Pol01 Poling, B.E., J.M. Prausnitz and J.P. O'Connell, *The Properties of Gases and Liquids*, 5th ed., McGraw-Hill, New York, 2001.

Pre92a Press, W.H., S.A. Teukolsy, W.T. Vetterung and B.P. Flannery, Numerical Recipes, Ch. 10, Cambridge University Press, Cambridge, 1992.

Pre92b Press, W.H., S.A. Teukolsy, W.T. Vetterung and B.P. Flannery, Numerical Recipes, Ch. 20, Cambridge University Press, Cambridge, 1992.

Red93 Reddy, J.N., *Computers and Structures*, 47, 857-869 (1993).

Red82 Reddy, J.N., *Int. J. Numer. Methods Fluids*, 2, 151-171 (1982).

Ric91 Richter, W., P. Kurpas, R. Luckerath, and M. Motzkus, *J. Crystal Growth*, 107, 13-25 (1991).

Rie97 Riechert, H., R. Averbeck, A. Graber, M. Schienle, U. Strauss, and H. Tews, *Mater. Res. Soc. Symp. Proc.*, 449, 149-159 (1997).

Rob91 Robles, E.S.J., A.M. Ellis, and T.A. Miller, *Chem. Phys. Lett.*, 178, 185-191 (1991).

Sac83 Sacilotti, M., A. Mircea and R. Azoulay, *J. Cryst. Growth*, 63, 111-115 (1983).

Saf97 Safvi, S.A., J.M. Redwing, M.A. Tischler, and T.F. Kuech, *J. Electrochem. Soc.*, 144, 1789-1796 (1997).

Sah00 Sahin, Õ., P. Sayan and A.N. Bulutcu, *J. Cryst. Growth*, 216, 475-482 (2000).

San92 Sano, H., G. Mizutani, and S. Ushioda, *Chem. Phys. Lett.*, 194, 398-402 (1992)

San00 Santen, H.V., C.R. Kleijn and H. Akker, *J. Cryst. Growth*, 212, 311-323 (2000).

Sch79 Schrötter, H.W. and H.W. Klöckner, In *Raman Spectroscopy of Gases and Liquids*, A. Weber, Editor, Ch. 4, Springer-Verlag, New York, 1979.

Sch00 Schäfer, J., A. Simons, J. Wolfrum and R.A. Fischer, *Chem. Phys. Lett.*, 318, 477-481 (2000).

Sch04 Schaftenaar, G. and J.H. Noordik, *J. Comput.-Aided Mol. Design*,14, 123-134 (2000).

Sco96 Scott, A.P. and L. Radom, *J. Phys.Chem.*, 100, 16502-16513 (1996).

Sed76 Sedgwick, T.O. and J.E. Smith, *J. Electrochem. Soc.: Solid-State Sci. Technol.*, 123, 254-258 (1976).

Sek78 Seki, Y., H. Watanabe, and J. Matsui, *J. Appl. Phys.*, 49, 822-828 (1978).

Sen03 Sengupta, D., *J. Phys. Chem. B*, 107, 291-297 (2003).

Shr00 Shreter, Y.G., Y.T. Rebane and W.N. Wang, *Phys. Stat. Sol. (A)*, 180, 307-313 (2000).

Sie72 Siegel, R. and J.R. Howell, *Thermal Radiation Heat Transfer*, McGraw-Hill, New York, 1972.

Sim97 Simka, H., B.G. Willis, I. Lengyel, and K.F. Jensen, *Prog. Crystal Growth and Charact.*, 35, 117-149 (1997).

Smi72 Smith, M.B., *J. Organometal. Chem.*, 46, 31-49 (1972).

Sto86 Stock, L. and W. Richter, *J. Cryst. Growth*, 77, 144-150 (1986).

Str89 Stringfellow, G.B., *Organometallic Vapor Phase Epitaxy: Theory and Practice*, Acedemic Press, San Diego, 1989.

Sug97 Sugiyama, M., K. Kusunoki, Y. Shimogaki, S. Sudo, Y. Nakano, H. Nagamoto, K, Sugawara, K. Tada, and H. Komiyama, *Applied Surface Science*, 117/118, 746-752 (1997).

Suz85 Suzuki, M. and M. Sato, *J. Electrochem. Soc.: Solid-State Sci. Technol.*, 132, 1684-1688 (1985).

Suz86 Suzuki, N., C. Anayama and K. Masu, *Jpn. A. Appl. Phys.*, 25, 1236 (1986).

Syw91a Sywe, B.S., J.R. Schlup, and J.H. Edgar, *Chem. Mater.*, 3, 737-742 (1991).

Syw91b Sywe, B.S., J.R. Schlup, and J.H. Edgar, *Chem. Mater.*, 3, 1093-1097 (1991).

Sza89 Szabo, A. and N.S. Ostlund, *Modern Quantum Chemistry*, Dover Publications, New York, 1989.

Tac99 Tachibana, A., O. Makino, S. Tanimura, H. Tokunaga, N. Akutsu and K. Matsumoto, *Phys. Stat. Sol. (a),* 176, 699-703 (1999).

Tak81 Takubo, Y., M. Tsuchiya and M. Shimazu, *Appl. Phys.*, 24, 139-142 (1981).

Tam88 Tamaru, K., *Acc. Chem. Res.*, 21, 88-94 (1988).

The00 Theodoropoulos, C., T. J. Mountziaris, H. K. Moffat and J. Han, *J. Cryst. Growth*, 217, 65-81 (2000).

Tho96 Thon, A. and T.F. Kueth, *Appl. Phys. Lett.*, 69, 55-57 (1996).

Tik77 Tikhonov, A.N. and V.Y. Arsenin, *Solutions of Ill-posed problems*, JohnWiley & Sons, New York, 1977.

Tjo92 Tjoa, I.-B. and L.T. Biegler, *Computers Chem. Engng.*, 16 (6), 523-533 (1992).

Tow75 Townes, C.H. and A.L. Schawlow, *Microwave Spectroscopy*, 7-9, Dover, New York, 1975.

Van78 Van den Bosch, B.A.J., *Identification of Parameters in Distributed Chemical Reactors* in Distributed Parameter Sytems, ed. by W.H. Ray and D.G. Lainiotis, Marcel Dekker, New York, 1978.

Van86 Van de Ven, J., G.M.J. Rutten, M.J. Raaijmakers and L.J. Giling, *J. Cryst. Growth*, 76, 352-372 (1986).

Vri75 Vriens, L. and M. Adriaansz, *J. Appl. Phys*., 46, 3146-3150 (1975).

Wan01 Wang, L. and C.N. Kim, *Korean J. Chem. Eng*., 18 (5), 652-661 (2001).

Yan99 Yang, C.-C., C.-K. Huang, G.-C. Chi and M.-C. Wu, *J. Cryst. Growth*, 200, 39-44 (1999).

Yas85 Yashida, M., H. Watanabe, and F. Uesugi, *J. Electrochem. Soc*., 132, 677-679 (1985).

Yaw99 Yaws, C.L., *Chemical Properties Handbook*, McGraw-Hill, New York, 1999.

Zao81 Zaouk, A., E. Salvetat, J. Sakaya, F. Maury, and G. Constant, *J. Crystal Growth*, 55, 135-144 (1981).

BIOGRAPHICAL SKETCH

Jang Yeon Hwang (황장연 in Korean) was born on December 24, 1967, in NamWon, Korea. Jang Yeon enjoyed nice times in the countryside until he enrolled in a primary school in Seoul. He received his Bachelor of Science and Master of Science degrees in chemical engineering from the Seoul National University in 1990 and 1992, respectively. In his mater's study, instability of a non-isothermal viscoelastic fluid layer flowing down an inclined plate was his academic interest. In 1992, he got a job with Hanwha Petrochemical Company and worked in polymer blends/composites and their processing areas. After working for six years, he decided to pursue his Ph.D. In 1998, he worked in the Korea Institute of Science and Technology until he attended the University of Florida. He joined Dr. Anderson's research group in 1999 and received his Doctor of Philosophy degree in chemical engineering during the summer of 2004.

I certify that I have read this study and that in my opinion it conforms to acceptable standards of scholarly presentation and is fully adequate, in scope and quality, as a dissertation for the degree of Doctor of Philosophy.

Timothy J. Anderson

Timothy J. Anderson, Chair
Professor of Chemical Engineering

I certify that I have read this study and that in my opinion it conforms to acceptable standards of scholarly presentation and is fully adequate, in scope and quality, as a dissertation for the degree of Doctor of Philosophy.

Chang Won Park

Chang-Won Park
Professor of Chemical Engineering

I certify that I have read this study and that in my opinion it conforms to acceptable standards of scholarly presentation and is fully adequate, in scope and quality, as a dissertation for the degree of Doctor of Philosophy.

James D Winefordner

James D. Winefordner
Graduate Research Professor of Chemistry

I certify that I have read this study and that in my opinion it conforms to acceptable standards of scholarly presentation and is fully adequate, in scope and quality, as a dissertation for the degree of Doctor of Philosophy.

Al

Adrian E. Roitberg
Associate Professor of Chemistry

This dissertation was submitted to the Graduate Faculty of the College of Engineering and to the Graduate School and was accepted as partial fulfillment of the requirements for the degree of Doctor of Philosophy.

August 2004

Pramod Khargonekar

Pramod P. Khargonekar
Dean, College of Engineering

Kenneth Gerhardt
Interim Dean, Graduate School